

Harmonic Resonance Assessment of Renewable Energy Power Plants on the Power System using Resonant Mode Analysis

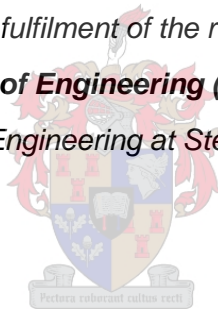
by

David Johannes Jacobus Scheepers

Thesis presented in partial fulfilment of the requirements for the degree of

Master of Engineering (Electrical)

in the Faculty of Engineering at Stellenbosch University



Supervisor: Dr. H.J. Beukes

Department of Electrical & Electronic Engineering

March 2021

Plagiarism declaration

Plagiarism is the use of ideas, material, and other intellectual property of another's work and to present it as my own.

I agree that plagiarism is a punishable offence because it constitutes theft.

I also understand that direct translations are plagiarism.

Accordingly, all quotations and contributions from any source whatsoever (including the internet) have been cited fully. I understand that the reproduction of text without quotation marks (even when the source is cited) is plagiarism.

I declare that the work contained in this assignment is my original work and that I have not previously (in its entirety or in part) submitted it for grading in another project / thesis / dissertation.

Name: David Scheepers
.....

Date: 27/11/2020
.....

Copyright © 2021 Stellenbosch University
All rights reserved

Abstract

Power quality problems and assessment methodologies associated with renewable energy power plants and resonant conditions are investigated. Resonant conditions are introduced by capacitive elements found in typical renewable energy power plant installations, namely the cabling capacitance and the inverter filter capacitors which resonates with inductive elements throughout the power system.

A 40 MW concentrated photovoltaic power plant serves as a case study. A simplified model of the power plant is developed and compared against a detailed DlgSILENT PowerFactory model to validate the results. The PowerFactory Python application programming interface is used to construct the PowerFactory model's admittance matrix for analysis.

Propagation analyses are performed on the developed simplified models as well as the PowerFactory model. Resonant mode analysis is applied to the PowerFactory model to calculate the participation factors of various elements connected to specific busbars. The participation factors indicate which system elements have dominant contributions to the creation of resonant conditions.

Opsomming

Krag kwaliteit probleme en assesserings metodeke wat geassosieer word met hernubare energie kragstasies en resonante kondisies word ondersoek. Resonante kondisies word veroorsaak deur kapasitiewe elemente in 'n tipiese hernubare energie kragstasie installasie, naamlik die kabel kapasitasie en die wisselrigter se filter kapasitore wat met induktiewe elemente in die krag netwerk resoneer.

'n 40 MW gekonsentreerde fotovoltaiiese kragstasie dien as gevallestudie. 'n Vereenvoudigde model van die kragstasie is ontwikkel en met 'n gedetailleerde DIGSILENT PowerFactory model vergelyk om die resultate te verifieer. Die PowerFactory Python toepassings programmering koppelvlak is gebruik om die PowerFactory model se admitansie matriks saam te stel om geanaliseer te word.

Propageeringsanalise word uitgevoer op die ontwikkelde vereenvoudigde modelle sowel as die PowerFactory model. Resonante modus analise is toegepas op die PowerFactory model om die bydraende faktore van verskeie elemente wat aan 'n spesifieke geleistam gekonnekteer is te bereken. Die bydraende faktore dui aan watter sisteem elemente dominante bydrae het tot die skepping van resonante kondisies.

Acknowledgements

I would like to acknowledge the following people for their contributions:

My supervisor, Dr. Johan Beukes, for his guidance throughout the past two years as well as providing insight into the various challenges we faced.

My fiancé, Ariane Korf, for her loving support and dedication towards keeping me on track to complete my thesis.

My parents, Dawie and Nina Scheepers, for supporting me throughout my studies and motivating me to give everything my best.

The Electric & Electronical Engineering Department and Eskom Power Plant Engineering Institute for their monetary contribution towards my studies.

Table of contents

	Page
Plagiarism declaration.....	i
Abstract	ii
Opsomming.....	iii
Acknowledgements	iv
Table of contents	v
List of figures	ix
List of tables.....	xiv
List of abbreviations.....	xvi
List of symbols	xvii
1 Introduction.....	1
1.1 Background.....	1
1.2 Project Motivation.....	2
1.3 Project Description	2
1.3.1 Research Objectives and Scope	2
1.3.2 Research Methodology.....	3
1.4 Thesis Overview.....	3
2 Literature Review.....	5
2.1 Introduction	5
2.2 Renewable resource penetration	6
2.3 Harmonic generating mechanisms in RPPs.....	7

2.3.1	VSDs	7
2.3.2	Inverters	9
2.4	Harmonic propagation.....	11
2.5	Effects of harmonic resonance.....	13
2.6	Harmonic assessment standards and methodologies.....	14
2.6.1	The IEEE 519-2014 standards	14
2.6.2	The IEC 61000-3-6 standard	17
2.6.3	The Cigré C4.103 working group.....	22
2.6.4	The Cigré C4.109 working group.....	22
2.7	Power system modal analysis.....	27
2.8	Conclusion	28
3	Simplified RPP Installation Single-Phase Equivalent Circuit Development	29
3.1	Introduction	29
3.2	RPP Modelling	29
3.2.1	Overview	29
3.2.2	Modelling assumptions and simplifications.....	31
3.2.3	Model parameter calculations.....	34
3.2.4	Summary	38
3.3	Developed model validation	39
3.3.1	MATLAB Simulink model.....	39
3.3.2	PowerFactory model.....	40
3.3.3	Simulink and PowerFactory model comparison.....	42
3.4	Conclusion	42
4	Resonance Analysis of a Simplified RPP Installation Circuit.....	44
4.1	Introduction	44
4.2	Development of frequency domain impedance function.....	45
4.3	Resonant frequency assessment.....	46
4.3.1	Low order resonance produced by inverter filter capacitor	46
4.3.2	High order resonance produced by cable capacitance.....	48
4.4	Simulation results comparison	49

4.5	The effect of resonance on harmonic propagation	50
4.5.1	Propagation of installation harmonic current emission	51
4.5.2	Propagation of background harmonic voltage distortion	54
4.6	RPP installation resonance sensitivity analysis.....	57
4.6.1	Inverter filter capacitor sensitivity analysis.....	57
4.6.2	Medium voltage cabling sensitivity analysis	58
4.7	Conclusion	59
5	Resonant Mode Analysis of an RPP Installation Circuit	61
5.1	Introduction	61
5.2	RMA of the simplified system.....	62
5.2.1	Establishing the admittance matrix	62
5.2.2	Eigenvalue calculation.....	64
5.2.3	Eigenvalue decomposition.....	65
5.2.4	Participation factor.....	66
5.2.5	Results	67
5.3	Harmonic propagation as affected by modes.....	70
5.3.1	Propagation of installation's current emission	72
5.3.2	Propagation of background harmonic voltage	73
5.4	Conclusion	76
6	Application of RMA on Complex PowerFactory Model using Python	78
6.1	Introduction	78
6.2	System model development.....	79
6.2.1	Network reduction methodology	79
6.2.2	Network model.....	80
6.2.3	Validation.....	85
6.2.4	Admittance matrix construction methodology	87
6.3	PowerFactory Python API	88
6.3.1	Setup	90
6.3.2	Processing.....	91
6.3.3	Results	94
6.4	Python model validation	95

6.4.1	Long line effect	95
6.4.2	Skin effect.....	96
6.5	RMA results	98
6.6	PowerFactory RMA propagation results.....	102
6.6.1	Harmonic voltage propagation.....	102
6.6.2	Harmonic current propagation	107
6.7	Conclusion	110
7	Conclusions	112
7.1	Summary.....	112
7.2	Conclusions	113
7.3	Contributions.....	114
7.4	Future research.....	114
8	References	116
	Appendix A Network Models	120
	Appendix B Python Code Discussion	125
	Appendix C MATLAB Code Discussion.....	138
	Appendix D Additional Resonant Mode Results.....	140

List of figures

	Page
Fig. 2-1. Various energy resources with installed generation capacity, 2019	6
Fig. 2-2. Simplified three-phase 6-pulse rectifier circuit	8
Fig. 2-3. Ideal six-pulse rectifier input voltage and AC-side phase-A current waveforms	8
Fig. 2-4. Six-pulse rectifier current source's harmonic content	9
Fig. 2-5. Simplified equivalent resonance circuit for a) series resonance (jX_s) b) parallel resonance (jX_p)	13
Fig. 2-6. Summation of pre- and post-connection harmonic voltage vectors with installation contribution vector V_{hi}	18
Fig. 2-7. Equivalent harmonic contribution circuit for grid and installation	22
Fig. 2-8. Apparent power consumption vs voltage emission level correlation	24
Fig. 2-9. a) Network b) Installation dominant contributor source simplified circuits	25
Fig. 2-10. Harmonic impedance slopes of dominant harmonic contributing sources	26
Fig. 3-1. Overview of a typical 40MVA RPP	30
Fig. 3-2. Detailed overview of a single branch	31
Fig. 3-3. a) Complete and b) neglecting excitation current representations of a single-phase two-winding transformer	32
Fig. 3-4. Cable shunt admittance circuit	33
Fig. 3-5. Detailed three-winding transformer a) and simplified three-winding transformer b)	33
Fig. 3-6. VSI circuit representation	34
Fig. 3-7. Simplified aggregated element single-phase equivalent model of an RPP installation	34

Fig. 3-8. Simulink model of simplified installation and network	39
Fig. 3-9. Frequency sweep impedance as seen at the POC of the Simulink model	40
Fig. 3-10. Frequency sweep impedance as seen at the POC of the detailed PowerFactory model	41
Fig. 4-1. System diagram for calculating POC driving point impedance	45
Fig. 4-2. Assessment loops of dominant elements causing low order a) parallel and b) series resonance	47
Fig. 4-3. Assessment loops of dominant elements causing high order parallel a) and series b) resonance	48
Fig. 4-4. Installation harmonic current source propagation	51
Fig. 4-5. Harmonic current distortion contribution from installation harmonic current emission	53
Fig. 4-6. Harmonic voltage distortion contribution from installation harmonic current emission	54
Fig. 4-7. Background harmonic voltage distortion propagation	54
Fig. 4-8. Harmonic current emission contribution from background harmonic voltage distortion	56
Fig. 4-9. Harmonic voltage distortion contribution from background harmonic voltage distortion	57
Fig. 4-10. System 3D resonance sensitivity mesh graph of the function $f(f, C_i)$	58
Fig. 4-11. System 3D resonance sensitivity mesh graph of the function $f(f, C_c)$	59
Fig. 5-1. Labelled simplified network and RPP installation model	62
Fig. 5-2. Modal impedance of simplified system	67
Fig. 5-3. Critical mode impedance of simplified system	68
Fig. 5-4. Driving point impedance (bottom) decomposition from modal impedances (top) of simplified network model	70
Fig. 5-5. Harmonic voltage distortion contribution from installation harmonic current emission using modal analysis	72

Fig. 5-6. Simplified system harmonic current emission contribution from installation harmonic current emission using modal analysis	73
Fig. 5-7. Simplified system harmonic voltage distortion contribution from background harmonic current emission using modal analysis	74
Fig. 5-8. Simplified system harmonic current distortion contribution from network harmonic current emission using modal analysis	Error! Bookmark not defined.
Fig. 5-9. Simplified system harmonic voltage distortion contribution from background harmonic voltage distortion using modal analysis	75
Fig. 5-10. Simplified system harmonic current emission contribution from background harmonic voltage distortion using modal analysis	76
Fig. 6-1. Various network conditions' frequency sweep impedances	80
Fig. 6-2. Bacchus self-impedance (top) and phase angle (bottom)	81
Fig. 6-3. Network AC voltage source representation with source impedance	84
Fig. 6-4. Bacchus network impedance and interpolated model impedance	85
Fig. 6-5. Impedance (top) and phase angle (bottom) comparison of reduced and detailed network models	87
Fig. 6-6. Flow diagram of Python code process overview	89
Fig. 6-7. Python IDE interaction with PowerFactory API	90
Fig. 6-8. Construction of the admittance matrix flow diagram	92
Fig. 6-9. Admittance matrix construction process flow diagram	93
Fig. 6-10. Modal analysis and eigenvalue/vector sorting method	94
Fig. 6-11. Long line effect influence on Touwsrivier busbar impedance	96
Fig. 6-12. Comparison of Python model without and with skin effect	97
Fig. 6-13. Comparison between NGC and PowerFactory skin effects	98
Fig. 6-14. Identified system resonant modes	99
Fig. 6-15. Installation- and network-side aggregated participation towards the resonant modes	101

Fig. 6-16. POC bus impedance (bottom) decomposition from modal impedances (top) of reduced network PowerFactory model	102
Fig. 6-17. Harmonic voltage distortion (blue) and transfer impedance approximated harmonic voltage distortion (black) for a 10 A @ 132 kV harmonic current injection at the inverter containers	104
Fig. 6-18. Harmonic voltage distortion (blue) and transfer impedance approximated harmonic voltage distortion (black) for harmonic current injection from the Laingsburg busbar	106
Fig. 6-19. Harmonic current propagation for harmonic current injection at the inverter containers	108
Fig. 6-20. Harmonic current propagation for harmonic current injection at the Laingsburg busbar	109
Fig. A-1. Large Western Cape generating network overview	120
Fig. A-2. Complete Karoo network overview	121
Fig. A-3. Complete RPP PowerFactory Model	122
Fig. A-4. Partial network representation with connected RPP installation	123
Fig. A-5. Partial network model developed in PowerFactory	124
Fig. D-1. Modal impedances of all the extended power system's modes	140
Fig. D-2. Power system bus participation visualisation (top) and bar graph (bottom) for mode 16 at 313.7 Hz	141
Fig. D-3. Power system bus participation visualisation (top) and bar graph (bottom) for mode 15 at 485.0 Hz	142
Fig. D-4. Power system bus participation visualisation (top) and bar graph (bottom) for mode 13 at 600.3 Hz	143
Fig. D-5. Power system bus participation visualisation (top) and bar graph (bottom) for mode 14 at 996.1 Hz	144
Fig. D-6. Power system bus participation visualisation (top) and bar graph (bottom) for mode 12 at 1505.4 Hz	145

Fig. D-7. Power system bus participation visualisation (top) and bar graph (bottom) for mode
6 at 1981.4 Hz 146

Fig. D-8. Power system bus participation visualisation (top) and bar graph (bottom) for mode
11 at 2256.3 Hz 147

List of tables

	Page
Table I: Different sampling method $\kappa(\omega)$, $\beta(\omega)$ and $\gamma(\omega)$ values [18].....	11
Table II: Voltage distortion limits for 69 kV to 161 kV _{L-N} power systems	15
Table III: Current distortion limits (odd harmonics) for 69 kV to 161 kV _{L-N} power systems ..	16
Table IV: Summation formula probabilistic α values in the absence of specific system information	18
Table V: Harmonic voltage planning levels (percentage of fundamental voltage) in HV and EHV power systems.....	20
Table VI: Parameters for simplified installation model	38
Table VII: Frequency summary of simplified Simulink model.....	40
Table VIII: Frequency summary of detailed PowerFactory model.....	41
Table IX: Simulink and PowerFactory frequency and impedance comparison	42
Table X: Resonant frequencies from simulation versus estimations from equations (4.5) - (4.8)	50
Table XI: Simplified system parameter values	64
Table XII: Modal resonant frequencies of simplified system model	68
Table XIII: Simplified system resistive damping values.....	69
Table XIV: PFs of simplified system resonant modes at each node for peak resonant frequencies	69
Table XV: Reduced network OHL properties	84
Table XVI: PowerFactory frequency sweep results object structure	91
Table XVII: Modal resonant frequencies of PowerFactory reduced network model	99
Table XVIII: Transfer impedance and harmonic voltage distortion for selected system buses with a 10 A @ 132 kV harmonic current injection at the inverter containers	105

Table XIX: Transfer impedance and harmonic voltage distortion for selected system buses
with 10 A @ 132 kV harmonic current injection at the Laingsburg busbar 107

List of abbreviations

API	Application Programming Interface
FFT	Fast Fourier Transform
IDE	Integrated Development Environment
IEC	International Electrotechnical Commission
IEEE	Institute of Electrical and Electronics Engineers
IPP	Independent Power Producer
IRP	Integrated Resource Plan
LRM	Linear Regression Model
NDP	National Development Plan
PF	Participation Factor
POC	Point of Connection
POE	Point of Evaluation
PWM	Pulse Width Modulation
QoS	Quality of Supply
REIPPP	Renewable Energy Independent Power Procurement Programme
RMA	Resonant Mode Analysis
RMSE	Root Mean Squared Error
RPP	Renewable Energy Power Plant
TDD	Total Demand Distortion
VFD	Variable-Frequency Drive
VSD	Variable-Speed Drive
VSI	Voltage Source Inverter

List of symbols

Units:

C	Capacitance [F]
f	Frequency [Hz]
F	Current or Voltage measurement [A or V]
I	Current magnitude [A]
\bar{I}	Complex current phasor [A]
L	Inductance [H]
ω	Angular frequency [Rad].
R	Resistance [Ohm]
t	Time [s]
V	Voltage magnitude [V]
V_{RMS}	RMS voltage [V]
\bar{V}	Complex voltage phasor [V]
X	Reactance [Ohm]
Y	Admittance [S]
Z	Complex impedance value [Ohm]

Variables:

α	Summation law exponent
β_0, β_1	Linear regression coefficients
$\hat{\beta}_0, \hat{\beta}_1$	Linear regression least squares estimators

ε	Random error component
h	Harmonic order (integer multiple of fundamental frequency)
H	Half-period
λ	Eigenvalue
Λ	Diagonal eigenvalue matrix
m_a	Modulation index
Φ	Right eigenvector
Ψ	Left eigenvector
R^2	Coefficient of determination
S	Sample space
y	Response variable
\hat{y}	Linear regression estimated response variable
Y-Y	Wye-Wye connection
Y- Δ	Wye-Delta connection

1 Introduction

This chapter introduces the topics that are investigated in this thesis. Background information is provided, followed by the research motivation, project objectives, scope and the research methodology that will be implemented. Finally, a breakdown of the structure and content of the thesis will be provided.

1.1 Background

The increasing demand for renewable energy has led to an increase in renewable energy power plants (RPPs) as well as in the injection of a wide band of harmonics into the utility network. These RPPs are allowed to generate a wide range of harmonics in accordance with their operational characteristics, level of production, internal network configuration and the connected network's characteristics. It is, however, an international concern regarding the uncertainty of the contribution of a connected RPP when various sources of harmonics are connected to the same network interacting with each other.

A RPP can be modelled as a dynamic load/source combination as these parameters fluctuate significantly over time causing the RPP to either generate or absorb harmonics during different operating conditions. It is common practise to assume that any harmonics measured at the point of connection (POC) are injected into the network leading to RPPs facing increased operational cost to mitigate the claimed harmonic injections. Mitigation methods such as installing active or passive filters could have adverse effects on the impedance profile of the network. It is therefore important to identify whether harmonics are being injected or absorbed by an RPP as an RPP absorbing harmonics would be beneficial for the network quality of supply (QoS).

In academic literature various methods for determining harmonic emissions and contributions are suggested in [1], [2], [3] and [4]. Information regarding individual harmonics are, however, not provided through commonly used methods such as the power direction method which produce incorrect results in various conditions.

1.2 Project Motivation

The primary motivation behind this study is to provide independent power producers (IPPs) with a basis from which harmonic contributions can be accurately quantified.

The power utility is required to regulate the harmonic voltage levels on the network to comply with NRS 048-2 compatibility levels. A dependable method for establishing the main contributors towards certain harmonic orders is therefore essential. A method for analysing the contribution that RPPs have towards the total harmonic distortion would enable the power utility to grant or deny compliance to IPPs on a fair and informed basis.

The nature of the interaction between the network and RPP installation will be investigated to determine whether detrimental effects become prevalent due to the connection of an RPP. Various contributing components of a typical RPP will be considered and its interaction with network elements investigated.

Power system impedance-based analysis and resonant mode analysis (RMA) will be the main tools for analysing the interaction between the power system and an RPP.

1.3 Project Description

1.3.1 Research Objectives and Scope

- *Identifying harmonic generating mechanisms.* This study focuses on the effects of harmonic injection from RPPs. Various mechanisms that lead to increased harmonic distortion will be reviewed in literature and discussed in corresponding chapters.
- *Modelling of simplified RPP.* Developing a simplified RPP model through analytical methods and MATLAB Simulink modelling will be a primary objective. The contribution of specific detrimental components will be easily identifiable if an accurate, simplified representation of a complex system can be developed.
- *Harmonic impedance analysis.* Illustrate the relationship that various elements in the power system and RPP installation have on the harmonic impedance at the POC.
- *Modal domain analysis.* Analyse the modal domain to determine causes of resonant conditions and the participation factors associated with them. Describe combined effect of various components to identify the main cause of resonance in a large power system.
- *DigSILENT PowerFactory modelling.* Develop an expansive network model in conjunction with an analytically simplified RPP model.

- *Python programming*. Implementing Python on the Spyder integrated development environment (IDE) to construct system matrices, using a PowerFactory application programming interface (API), and apply RMA on the constructed data.

1.3.2 Research Methodology

Existing harmonic assessment methodologies will be researched to establish an understanding of how the harmonic assessment process is conducted for RPPs connected to an HV power system.

Simplified RPP models will be developed to provide greater insight into harmonic resonance and its influence on the larger power system. Propagation of harmonics under resonant conditions will be numerically modelled. The simplified model will be developed in MATLAB Simulink and the complete layout RPP model in PowerFactory.

Simulations of the RPP will be conducted to compare the MATLAB and PowerFactory models. The simplified MATLAB model will be compared to a complete layout model in PowerFactory to ensure that sufficient similarities exist between the two models. These simulations will be used to identify resonant conditions in the modelled power system and the effect of various elements on the impedance seen at the POC.

Python will be implemented in conjunction with the PowerFactory API to construct the PowerFactory model's positive sequence admittance matrix. RMA will be conducted and analysed in the Python environment.

The results from the RMA will be investigated to identify the dominant elements that contribute towards resonant conditions as well as the propagation of harmonics.

1.4 Thesis Overview

In Chapter 2 a literature review introducing the causes of harmonics and the detrimental effect thereof is conducted. The concept of resonant conditions is discussed along with established assessment techniques to analyse harmonics before the concept of modal domain RMA is introduced.

In Chapter 3 a simplified single-phase equivalent circuit of a large RPP will be developed. The modelling methodology is discussed along with the assumptions and simplifications. The developed model is compared against a detailed PowerFactory model to validate the simplified model.

In Chapter 4 the simplified circuit developed in Chapter 3 will be analysed using an impedance-based analytical approach to determine which elements influence the resonant conditions. The impedance-

based analytical approach will identify resonant loops in the simplified circuit and intuitively determine the contribution of certain elements toward the resonant conditions. The propagation effect of resonant conditions is analytically described through circuit analysis.

In Chapter 5 the impedance-based analytical approach is taken further with the inclusion of RMA to identify specific buses in a larger system which contribute towards various resonant conditions. The admittance matrix is constructed, and eigenvalue decomposition is applied to obtain the orthogonal resonant conditions located within the system. The propagation effect is once again described but through the analysis of transfer impedances.

In Chapter 6 the simplified model is expanded to include a real network operating condition which is developed in PowerFactory. The modelling process is described, and a new system model implemented for further analysis. The system model's admittance matrix is determined through an analytical process developed in Python to automatically obtain the larger power system's admittance matrix since such a feature is not available in PowerFactory. RMA is applied to the developed PowerFactory model and network. Installation related resonant conditions are then discussed. The propagation of harmonics injected into the developed model is once again analysed to illustrate the effect of additional elements introduced by a larger power system.

In Chapter 7 the final conclusions, based on the results obtained from the previous chapter, are made regarding the findings from this thesis. The contributions and achieved objectives are summarised. Future work that would be required to extend this research is listed and elaborated upon.

2 Literature Review

This chapter covers the problems associated with QoS and reviews documentation on various aspects thereof. Fundamental principles behind harmonic injection are discussed to provide additional insight. A review of various international assessment techniques and standards is conducted along with other assessment methods suggested in literature.

2.1 Introduction

To understand the quality of supply (QoS) problems related to harmonics the following concepts will be reviewed to provide greater insight into the topic that is investigated in this study:

Renewable resource penetration in South Africa provides motivation to investigate the effect that distributed generation has on QoS. Background on the current state of the power system and the renewable energy sector's planned trajectory of renewable energy distributed generation for the future will be investigated.

The harmonic generating mechanisms that cause harmonic currents and consequently harmonic voltage distortion on the AC network are investigated to identify the cause of QoS related problems. Equipment that can be typically associated with RPPs and industrial applications will be investigated along with the harmonic content associated with inverter sampling operations.

The propagation of harmonic current emissions in the network needs to be investigated to determine how far injected harmonic current can propagate through the utility network and the effect that it would have on the harmonic voltage distortion at various busbars. This propagation needs to be quantified to understand the global effect of harmonic current emission.

The effect of harmonic resonance on harmonic voltage distortion levels with regards to the attenuation or amplification thereof will be investigated. Being able to determine resonant conditions would provide insight into which order of injected harmonic currents would lead to greater harmonic voltage distortion in the power system. The effects of resonance will also provide insight into harmonics propagation.

Methodologies to determine the cause of measured harmonic distortion and the standard assessment of harmonics at the point of evaluation (POE) will be reviewed. This would enable an understanding

of how harmonics are perceived and provide insight into the factors that influence the results of these assessments.

The concept of evaluating the cause of resonant conditions will be investigated to determine its applicability in the assessment of harmonics on the power system. The proposed analysis in the modal domain provides insight into the excitability and observability of harmonics throughout the entire power system and would provide a transformed system that simplifies the assessment of resonant conditions.

2.2 Renewable resource penetration

Renewable energy resources integration into South Africa's energy mix has been an imperative factor since the promulgation of the integrated resource plan (IRP) in March 2011. Renewable resources include various sources, namely, hydro, wind, solar and pumped storage. The South African power system has an installed generation capacity as illustrated in Fig. 2-1 [5].

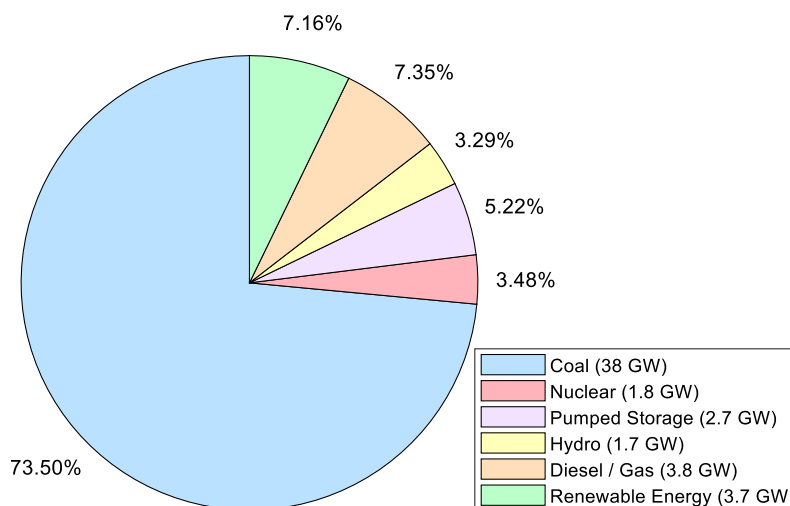


Fig. 2-1. Various energy resources with installed generation capacity, 2019

The renewable energy independent power procurement programme (REIPPP) has allowed the total generation capacity provided by independent power producers (IPPs) to grow to 5 206 MW, as of 31 March 2020 [6]. The objective is to reach 17 800 MW of renewable energy resources by 2030 [7] through the REIPPP. This uptake in renewable energy resources warrants the need for grid impact assessments and understanding how RPPs interact with the network.

2.3 Harmonic generating mechanisms in RPPs

Non-linear rectifier loads have increasingly been introduced into the power system since the 1970's [8]. According to the IEC 61000 2-1, static power converter and electric arc furnaces are the primary industrial non-linear loads contributing to harmonic distortion in the industrial category, whilst switch-mode power supplies in personal computers and televisions are the most prominent distortion devices in the residential category [9].

Electrical equipment introduced by RPPs such as variable-speed drives (VSDs) and inverters have non-linear characteristics that introduce harmonic emissions into the power system. The problems associated with renewable energy systems were discussed in [10] which focused on QoS issues introduced by distributed generation. It was found that harmonics were the most dominant QoS related problem not attributed to faulty connections [10].

VSDs consist of 3-phase 6-pulse rectifiers which generate harmonics throughout the frequency spectrum while inverters generate baseband and switching frequency harmonics. These devices are AC/DC rectifiers (VSDs) and DC/AC power electronic converters (inverters) which are typically associated with large-scale RPP installations. The fundamental concepts of harmonic generating mechanisms are discussed in [11].

2.3.1 VSDs

Rectifier circuits are known for generating harmonics which can be harmful to equipment sensitive to the peak supply voltage [12]. Harmonic current on the AC side of the network is induced due to these rectifiers' non-linear current draw operation.

In this research, the case study RPP installation implements VSDs within its dual-axis solar tracking systems. These VSDs introduce additional harmonic emissions in conjunction with the RPP's inverters.

Three-phase six-pulse rectifier

The three-phase six-pulse rectifier consists of 6 diodes or thyristors to produce 6 voltage pulses on the DC-side per source voltage period, fundamentally doubling the source frequency three times. A typical six-pulse rectifier circuit is illustrated in Fig. 2-2.

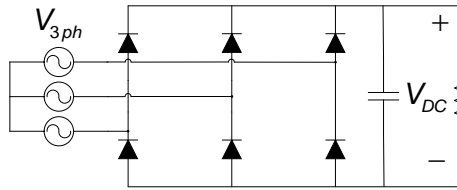


Fig. 2-2. Simplified three-phase 6-pulse rectifier circuit

Three-phase rectifiers are generally implemented for industrial applications as it is suitable for higher power rating equipment and has lowered ripple content when compared to single-phase rectifiers [13]. The simplest three-phase rectifier is the 6-pulse rectifier which is used in VSDs [14].

An ideal six-pulse rectifier, that neglects commutation and assumes a smooth current on the DC-side, produces a symmetrical square wave [14], [11]. In Fig. 2-3 the results of a single phase AC current generated by an ideal six-pulse configuration is illustrated.

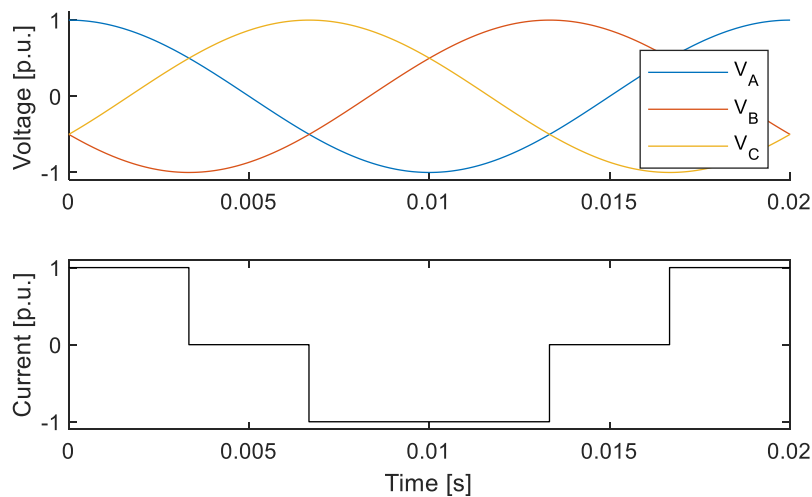


Fig. 2-3. Ideal six-pulse rectifier input voltage and AC-side phase-A current waveforms

Applying the FFT to the phase current induced by the 6-pulse rectifier, as illustrated in Fig. 2-3, results in the harmonic content illustrated in Fig. 2-4.

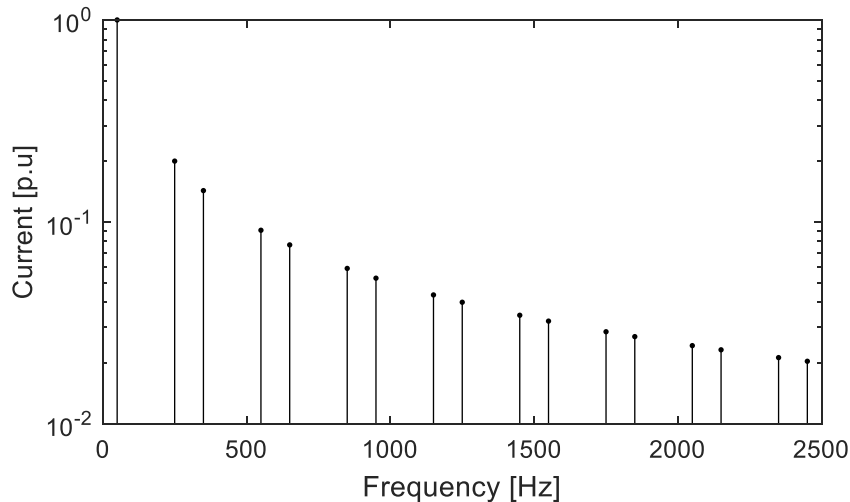


Fig. 2-4. Six-pulse rectifier current source's harmonic content

From Fig. 2-4 harmonics are observable at the odd-harmonic frequencies in regular intervals. The dominant odd-harmonics occur around multiples of 300 Hz and can be described as occurring at harmonic orders $h = k \cdot 6 \pm 1$ for $k = 1, 2, 3, \dots, n$. Even harmonics cancel out due to the symmetrical nature of the distorted AC current waveform.

2.3.2 Inverters

Different inverter topologies have various modulation schemes with the most implemented modulation scheme being pulse width modulation (PWM), which is the modulation system that will be investigated. Even though there exist various types of PWM schemes in literature all schemes are merely adaptations of three basic modulation systems. These modulation systems include naturally sampled PWM, regular sampled PWM and direct PWM [15].

Harmonic current injection due to PWM voltage source inverters (VSIs) implementing various control and sampling schemes leads to increased harmonic voltage on the utility power network. An RPP consists of many inverters connected in parallel thus leading to an increase in harmonic voltage distortion. In extreme cases excessive injected harmonic emissions from inverter harmonic generating mechanisms could lead to system equipment, such as capacitor banks and control devices, to malfunction and even overloading of power plants connected to the same network [16], [11].

The implemented modulation scheme is not the only aspect that determines the performance of an inverter. Most higher power level inverters implement closed-loop feedback for their modulation scheme, leading to the performance mostly relying on the closed-loop controller. The effect of various closed-loop control schemes will, however, not be investigated in this thesis.

Inverter PWM mathematical analysis

Traditionally the harmonics produced by the modulation process can be mathematically described using a two-dimensional Fourier series represented in the time-domain (t) and half-period (H) as follows [17]:

$$\begin{aligned}
 f(t, H) = & \frac{A_{00}}{2} + \sum_{n=1}^{\infty} (A_{0n} \cos(n\omega_1 t) + B_{0n} \sin(n\omega_1 t)) \\
 & + \sum_{m=1}^{\infty} \left(A_{m0} \cos\left(\frac{m\pi H}{2}\right) + B_{m0} \sin\left(\frac{m\pi H}{2}\right) \right) \\
 & + \sum_{m=1}^{\infty} \sum_{\substack{n=-\infty \\ (n \neq 0)}}^{\infty} \left(A_{mn} \cos\left(\frac{m\pi H}{2} + n\omega_1 t\right) \right. \\
 & \left. + B_{mn} \sin\left(\frac{m\pi H}{2} + n\omega_1 t\right) \right)
 \end{aligned} \tag{2.1}$$

where m is the carrier index and n is the baseband/sideband index.

Two fundamental harmonic components exist, namely, the baseband and carrier harmonic components. The baseband harmonics refers to the sideband harmonics located around the fundamental frequency while carrier harmonics refers to harmonics generated at integer multiples of the carrier frequency as well as its associated sidebands.

To calculate the Fourier transform of the PWM pulse train for different sampling methods a one-dimensional equation with specific parameters for each sampling method is developed in [18]. The one-dimensional integral for each corresponding sampling method results in the following:

$$S_m(\omega) = \int_{-\infty}^{\infty} \kappa(\omega) \sin(\beta(\omega) + \gamma(\omega)f(t)) e^{-j(\omega - m\omega_c)t} dt \tag{2.2}$$

With the values of $\kappa(\omega)$, $\beta(\omega)$ and $\gamma(\omega)$ changing in accordance with the sampling method that is implemented, according to Table I.

Table I: Different sampling method $\kappa(\omega)$, $\beta(\omega)$ and $\gamma(\omega)$ values [18]

Sampling method	$\kappa(\omega)$	$\beta(\omega)$	$\gamma(\omega)$
Naturally sampled	$\frac{2}{m\pi}$	$\frac{m\pi}{2}$	$\frac{m\pi}{2}$
Symmetric regular sampled	$\frac{2 \omega_c}{\pi \omega}$	$\frac{\pi \omega}{2 \omega_c}$	$\frac{\pi \omega}{2 \omega_c}$
Asymmetric regular sampled	$\frac{2 \omega_c}{\pi \omega}$	$\frac{\pi}{2} m$	$\frac{\pi \omega}{2 \omega_c}$

where ω_c is the switching frequency and ω is the harmonic frequency.

The fundamental difference between the naturally and regular sampled methods is the inclusion of baseband harmonics with the regular sampling method. The difference between symmetric regular and asymmetric regular sampling is that asymmetric regular sampling eliminates even-harmonic sideband and odd-harmonic sideband components around even and odd multiples of the carrier frequency, respectively [15].

Other non-ideal characteristics of inverters, such as deadtime, cause additional baseband harmonics.

2.4 Harmonic propagation

Harmonic current emissions generated through the mechanisms discussed in Section 2.3 are injected into the power system at baseband and switching frequencies. These emissions are subject to QoS requirements such as indicated in the South African grid code for RPPs and NRS 048 standards [19], [20]. The emissions that will be investigated for this study are the emissions introduced by an RPP connected to a HV busbar. The QoS requirements for RPPs connected to MV, HV or EHV busbars are presented in [19].

Harmonic propagation causes harmonic voltage distortion throughout the entire power system affecting connected customers' equipment [16]. The harmonic voltage distortion is calculated using the system impedance matrix, constructed using the system's nodal voltages and currents, as follows [21]:

$$\begin{bmatrix} V_1 \\ V_2 \\ \vdots \\ V_l \\ \vdots \\ V_n \end{bmatrix} = \begin{bmatrix} Z_{11} & Z_{12} & \cdots & Z_{1k} & \cdots & Z_{1n} \\ Z_{21} & Z_{22} & \cdots & Z_{2k} & \cdots & Z_{2n} \\ \vdots & \vdots & & \vdots & & \vdots \\ Z_{l1} & Z_{l2} & \cdots & Z_{lk} & \cdots & Z_{ln} \\ \vdots & \vdots & & \vdots & & \vdots \\ Z_{n1} & Z_{n2} & \cdots & Z_{nk} & \cdots & Z_{nn} \end{bmatrix} \begin{bmatrix} I_1 \\ I_2 \\ \vdots \\ I_k \\ \vdots \\ I_n \end{bmatrix} \quad (2.3)$$

These voltage distortions are subject to the susceptibility of the various busbars to the injected harmonic current's frequency. In [21] it is suggested that harmonic current emissions be evaluated individually, therefore implementing the concept of superposition, and summated to calculate the total harmonic voltage distortion at each bus.

Implementing superposition for a particular injected harmonic current emission, the harmonic voltage distortion at a bus can be determined using (2.3) as follows:

$$V_l = I_k Z_{lk} \quad (2.4)$$

where V_l is the bus voltage, I_k is the injected current and Z_{lk} is the frequency dependent transfer impedance between the two buses. All other currents are considered as zero.

The harmonic voltage distortion calculated using (2.3) can also be implemented to determine the propagated harmonic current (I_{lk}) at each defined frequency as follows [21]:

$$I_{lk} = \frac{V_l - V_k}{Z_{lk}} \quad (2.5)$$

where V_l and V_k are the bus voltages of the injection and observation buses, respectively, and I_{lk} is the propagated harmonic current between the injection and observation bus.

For non-resonant conditions, the harmonic voltage distortion is expected to diminish as the ratio of the harmonic current to fundamental current decreases [8]. This is attributed to the linear nature of non-resonant conditions.

The impedance matrix from (2.3) only considered steady-state space variables. This is acceptable for studying harmonic propagations under specific operating conditions but does not illustrate the variability of resonant conditions on a large power system. In [22] the concept of a dynamically changing impedance envelope is presented with the investigation of harmonic propagation in traction networks.

Changing loads and network configurations impact network conditions and introduce volatility to the network's impedance envelope. This will only be investigated briefly for specific RPP installation elements as stochastic power system modelling is not within the scope of this thesis.

2.5 Effects of harmonic resonance

Section 2.4 introduced harmonic propagation and the impedance matrix which governs the amount of harmonic propagation throughout the entire power system. The transfer- and self-impedances contribute to the amount of harmonic voltage distortion that is observed due to harmonic current injection.

Two types of resonant conditions occur when capacitive and inductive reactances create oscillating energy exchange loops. These are low and high impedance resonant conditions, called series and parallel resonance, which approach zero and infinite impedance, respectively. Resonant conditions can therefore be simplified to a unique equivalent capacitive-inductive circuit as illustrated in Fig. 2-5.

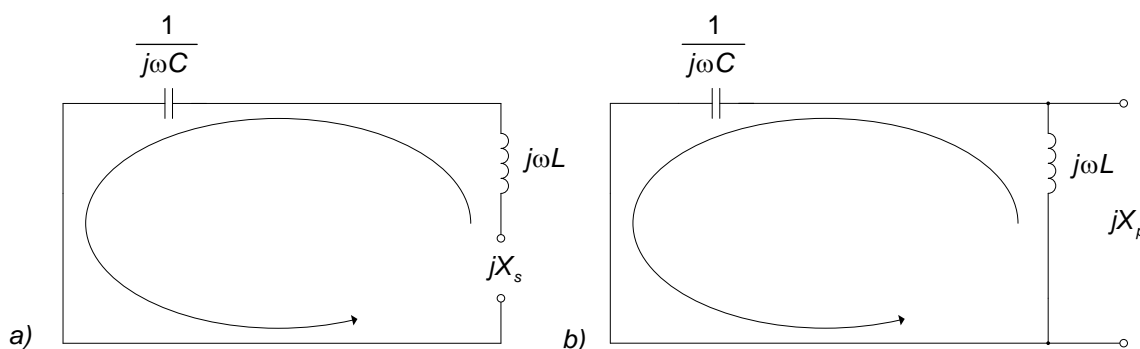


Fig. 2-5. Simplified equivalent resonance circuit for a) series resonance (jX_s) b) parallel resonance (jX_p)

In an ideal power system, there would exist no harmonic content in the power system, therefore no excitation would be experienced from resonant conditions above the fundamental frequency [8]. As Section 2.3 discussed, VSDs and inverters inject harmonic current into the power system therefore exciting these resonant conditions. The investigation of resonant conditions introduced by VSDs and inverters connected to the network is therefore paramount.

In [23], [8] and [24] the effects of harmonics on utility network equipment is presented. Through these studies it is shown that the installation of any capacitive equipment on the network could lead to increased resonant conditions. In [8] the resonant frequency of a basic LC circuit, similar to Fig. 2-5, is calculated using the following:

$$\frac{f_R}{f_1} = \frac{1}{\omega_1} \sqrt{\frac{1}{LC}} \quad (2.6)$$

where f_R is the resonant frequency, f_1 is the fundamental frequency ($\omega_1 = 2\pi f_1$), L is the equivalent inductance and C is the equivalent capacitance. Harmonic distortion is therefore amplified as the system excitation frequency approaches the resonant frequency.

Typical RPPs introduce two reactive elements that significantly influence resonant conditions namely, the cable shunt capacitances and inverter filter capacitors. These capacitances introduce additional resonant conditions which varies depending on the connected network's impedance envelope. These two capacitive elements will be investigated to identify resonant conditions associated with the inclusion of an RPP on the power system.

2.6 Harmonic assessment standards and methodologies

The previous sections discussed sources of harmonic distortion and the amplification factors associated with reactive elements on the power system. The primary reason harmonic distortion assessment was introduced was due to the large harmonics introduced by VFDs [8]. The accumulation of more power electronic devices connected to the power system each year also further necessitated harmonic limit assessments to ensure proper QoS.

The harmonic assessment methodologies that will be investigated are described by various organisations and institutions including the International Electrotechnical Commission (IEC) and the Institute of Electrical and Electronics Engineers (IEEE) [25][26]. These methodologies are further supplemented and simplified by organisational working groups such as the Cigré working groups [27], [28]. The application of these methodologies will be investigated for an HV system (132 kV).

IEC and IEEE produced the main aspects from which the national regulatory standards in South Africa is derived from in the NRS 048-1:2003 [20] which contains the QoS assessment methods prescribed by the power system utility company Eskom.

2.6.1 The IEEE 519-2014 standards

It is stated that although the IEEE does not provide a broad spectrum of QoS standards, it provides practically implementable standards [16]. It also requires that measurement instruments comply with the IEC 61000 specifications showing coherence between the various standards.

The IEEE 519-2014 [26] focuses on two types of measurements namely, short time (10-minute intervals, $F_{n,sh}$) and very short time (3-second intervals, $F_{n,vs}$). Very short time measurements are aggregated rms values of 15 consecutive 10 cycle windows at 50 Hz. This is calculated as follows:

$$F_{n,vs} = \sqrt{\frac{1}{15} \sum_{i=1}^{15} F_{n,i}^2} \quad (2.7)$$

Short time measurements are aggregated rms values of 200 consecutive very short samples. This is calculated as follows:

$$F_{n,sh} = \sqrt{\frac{1}{200} \sum_{i=1}^{200} F_{(n,vs),i}^2} \quad (2.8)$$

where F represents the rms value of voltage or current and n is the harmonic order.

These values are statistically evaluated over periods of 24-hours and 7-days for very short and short time interval aggregated values, respectively. For very short interval aggregated values the 99th percentile is used to evaluate harmonic limit. For short interval aggregated values both the 95th and 99th percentile values are evaluated against the harmonic limits, except for the 99th percentile for the harmonic voltage limit evaluation.

Harmonic voltage distortion limits

Recommended harmonic limits are further specified for the POC which is also specified as the POE for harmonic assessments. The aggregated harmonic voltage at the POC over the indicated evaluation period is specified as follows:

- Less than 1.5 times the recommend limits for very short time (3-second) 99th percentile values.
- Less than the recommend limits for short time (10-minute) 95th percentile values.

The recommended voltage distortion limits applicable to a 132 kV_{L-L} (76.2 kV_{L-N}) system are indicated in Table II.

Table II: Voltage distortion limits for 69 kV to 161 kV_{L-N} power systems

Bus voltage V at POC (kV_{L-N})	Individual harmonic (%)	Total harmonic distortion THD (%)
69 kV < V ≤ 161 kV	1.5 %	2.5 %

The voltage distortion limits are defined for individual harmonics as well as the total harmonic distortion (THD) defined as follows:

$$THD = \sqrt{\frac{\sum_{h=2}^n F_h^2}{F_1^2}} \times 100\% \quad (2.9)$$

where F_h is the harmonic component value at harmonic order h and F_1 is the fundamental component value of either voltage or current. THD is expressed as a ratio of the harmonic content to the fundamental component.

Harmonic current distortion limits

Harmonic current limits at the POC, for a 132 kV_{L-L} system, are specified as follows:

- Less than 2 times the recommend limits for very short time (3-second) 99th percentile values.
- Less than 1.5 times the recommend limits for short time (10-minute) 99th percentile values.
- Less than the recommend limits for short time (10-minute) 95th percentile values.

The current distortion limits applicable to a 132 kV_{L-L} (76.2 kV_{L-N}) system are indicated in Table III.

Table III: Current distortion limits (odd harmonics) for 69 kV to 161 kV_{L-N} power systems

Maximum harmonic current distortion in percent of I_L (%) for odd harmonic orders (h)						
I_{SC}/I_L	$3 \leq h < 11$	$11 \leq h < 17$	$17 \leq h < 23$	$23 \leq h < 35$	$35 \leq h < 50$	TDD
< 20	2.0	1.0	0.75	0.3	0.15	2.5
20 < 50	3.5	1.75	1.25	0.5	0.25	4.0
50 < 100	5.0	2.25	2.0	0.75	0.35	6.0
100 < 1000	6.0	2.75	2.5	1.0	0.5	7.5
> 1000	7.5	3.5	3.0	1.25	0.7	10.0

The even harmonics are not included in these distortion limits as they are limited to 25% of the individual harmonic group's limit. The total demand distortion (TDD) is also specified and is calculated as follows:

$$TDD = \sqrt{\frac{\sum_{h=2}^n I_h^2}{I_L^2}} \times 100\% \quad (2.10)$$

where I_h is the harmonic current and I_L is the maximum demand load current over a demand interval [29]. TDD is expressed as a ratio of the harmonic current content to the fundamental current and exclusively applies to harmonic current emissions in contrast to THD.

Conclusion

The QoS assessment methodology proposed by the IEEE takes a basic statistical approach to assessing harmonics at the POC. The limits, as stated above, must not exceeded more than 5% to 1% of the measurement period for short and very short time measurements, respectively.

No method for establishing the source of the harmonic distortion is defined as it is assumed that the background harmonics are well within its planned operating conditions. It is therefore suggestive that any harmonic measurements observed at the POE are due to harmonic injections from the customer. This methodology therefore lacks a comprehensive assessment method to determine the cause of the measured harmonic distortions.

2.6.2 The IEC 61000-3-6 standard

The IEC 61000 [25] series provides the most commonly implemented QoS standards in the industry [16]. It is also considered more comprehensive as QoS limits are assessed according to various classes of equipment.

Harmonic emission levels are defined as the vector change in system harmonic voltage or current emission levels for each assessed frequency. This is graphically illustrated in Fig. 2-6 where the pre- and post-connection harmonic voltage distortions are measured and the change in the distortion level is considered the installation's contributions (V_{hi}).

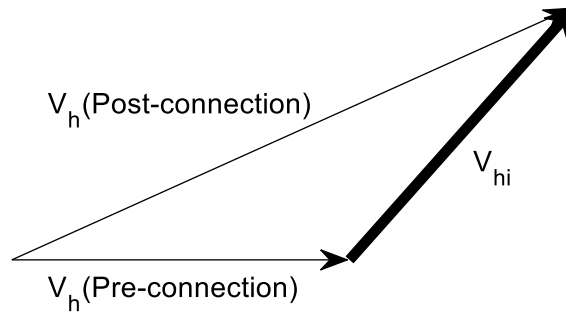


Fig. 2-6. Summation of pre- and post-connection harmonic voltage vectors with installation contribution vector V_{hi}

This leads to the summation approach of the IEC to harmonic emissions. When the contribution of various sources is considered to determine a specific installation's contribution, the general summation law can be adopted, defined as:

$$V_h = \sqrt[\alpha]{\sum_i V_{hi}^\alpha} \quad (2.11)$$

where the resulting harmonic voltage V_h is the aggregation of all the harmonic voltage sources' contributions, V_{hi} is the individual harmonic sources' emission level and α is the exponent of the summation law, with values as listed in Table IV, which varies depending on whether the generated harmonics are likely to be in phase or not.

Table IV: Summation formula probabilistic α values in the absence of specific system information

Harmonic Order	α
$h < 5$	1
$5 \leq h \leq 10$	1.4
$h > 10$	2

The use of 95 percentile values for "short" 10-minute assessment data and 99 percentile values for "very short" 3-second or 150 cycles (for 50 Hz) over a monitoring period of 1 week of normal operation is specified in [25]. The electrical measurement equipment is also required to comply with the standards presented in [30], with harmonics being evaluated up to the 40th or 50th harmonic order.

The IEC further lays more focus on the system's harmonic impedance envelope to convert harmonic voltage distortion limits to harmonic current limits. The harmonic impedance can be established through simulated generic system characteristics, worst case operating conditions or through

determining the actual harmonic impedance from a combination of simulations and actual measurements through the use of perturbation signals, as presented in [31].

The IEC emission assessment is more extensive than the IEEE assessment. The emission levels are assessed in 3 stages. The 1st stage evaluates a power criterion to determine whether the installation's emission requires examination. The power criterion is defined as:

$$\frac{S_i}{S_{sc}} \leq 0.2 \% \quad (2.12)$$

where S_i is the customer/installation power and S_{sc} is the short circuit power at the POE. The value of 0.2% is based on various assumptions regarding the system operation.

The installation can also be evaluated using the weighted power criterion, defined as:

$$S_{Dwi} = \sum_j S_{Dj} \cdot W_j \quad (2.13)$$

where S_{Dj} is the distorting equipment's (j) power rating in the installation (i). This weighted power criterion is evaluated as following:

$$\frac{S_{Dwi}}{S_{sc}} \leq 0.2\% \quad (2.14)$$

The weighting factors W_j are listed in [25] Table 4 and ranges from 0.5 for a 12-pulse converter to 2.5 for a single-phase power supply.

The 2nd stage assesses emission limits relative to system characteristics. This requires that the total apparent power of all the contributing installations be calculated as follows:

$$S_t = \sum S_{Din} + \sum S_{out} + \sum Q_{Dshunt} \quad (2.15)$$

where S_t is the total apparent power of all installations allocated to the system, S_{Din} is the apparent power of non-linear generating plant equipment, S_{out} is the apparent power flowing out of the HV busbar and Q_{Dshunt} is the dynamic reactive power rating of any conditioning equipment connected to the investigated busbar. The apparent power of the busbar under investigation (S_{tm}) can be used to allocate the installations' appropriate global contribution (G_{hBm}), apportioning the system planning level (L_{hHV}) as follows:

$$G_{hBm} \leq \alpha \sqrt{\frac{S_{tm}}{S_{t1} + S_{t2} + \dots + S_{tn}}} \cdot L_{hHV} \quad (2.16)$$

where S_{tm} is the individual apparent power of all the buses connected to the global system. The system planning levels for harmonic voltages applicable to MV, HV and EHV power systems are illustrated in Table V.

Table V: Harmonic voltage planning levels (percentage of fundamental voltage) in HV and EHV power systems

Odd harmonics (non-triplen)		Odd harmonics (triplen)		Even Harmonics	
Harmonic Order h	Harmonic Voltage %	Harmonic Order h	Harmonic Voltage %	Harmonic Order h	Harmonic Voltage %
5	2	3	2	2	1.4
7	2	9	1	4	0.8
11	1.5	15	0.3	6	0.4
13	1.5	21	0.2	8	0.4
$17 \leq h \leq 49$	$1.2 \cdot \frac{17}{h}$	$21 \leq h \leq 45$	0.2	$10 \leq h \leq 50$	$0.19 \cdot \frac{10}{h} + 0.16$
Planning level for THD is: $\text{THD}_{\text{HV-EHV}} = 3\%$ in HV and EHV systems.					

Harmonic voltage distortion limits

The apportioned global contribution is used in conjunction with the investigated busbar's and installations' apparent power to calculate the individual harmonic voltage emission limit, calculated as follows:

$$V_{Uhi} = G_{hBm} \alpha \sqrt{\frac{S_i}{S_{tm}}} \quad (2.17)$$

where V_{Uhi} is the harmonic voltage emission limit for bus m , S_i is the installations' rated apparent power, S_{tm} is the bus m 's total capacity rating and α is the exponent of the summation law's value.

The values calculated from (2.17) are limited to a minimum of 0.1% after which anything smaller than 0.1% is set equal to 0.1% unless severe restrictions are justified.

Harmonic current distortion limits

The harmonic current emission limit is calculated through dividing the harmonic voltage emissions with the system's frequency-dependent impedance. This is calculated as follows:

$$V_{Ihi} = \frac{V_{Uhi}}{Z_{hi}} \quad (2.18)$$

where V_{Ihi} is the corresponding harmonic current emission limit associated with the harmonic voltage emission limit V_{Uhi} and system frequency-dependant impedance Z_{hi} .

The 3rd stage assesses emissions that exceed limits as established in (2.17) and (2.18) above. This stage is implemented to address the conservative nature of generic system characteristics. Scenarios under which higher emission limits could be allowed are stated in [25] and specifically identified the use of generic harmonic impedance or amplification factors as a reason for overly restrictive harmonic current emission limits. The system operator is left to re-evaluate the system to establish higher emission limits that the conservative limits established in the 2nd stage.

Conclusion

The emission limits, as presented in the IEC 61000-3-6 standard, requires significantly more knowledge of the system under consideration to establish appropriate harmonic voltage and current emission limits. This could lead to more appropriate emission limits than those presented in the IEEE-519 as overall system emissions are subdivided according to individual installation's capacities. The concept of using a global contribution factor to establish proper emission limits therefore differentiates the IEC's from the IEEE's approach to establishing emission limits.

There are, however, no clear guidelines in the 3rd stage of the assessment on how emission limits that exceed the calculated emission limits should be assessed. It is suggested that the system operator employs knowledge of the operating condition of the system to re-evaluate the harmonic limits.

The implementation of a generic harmonic impedance and amplification factors (to account for resonance) is stated as generally being derived from using conservative system characteristics. The harmonic impedance mostly focuses on the worst normal operating condition and it is stated that future changes to power system should also be considered making it difficult to develop a suitable model. The harmonic impedance is identified as the system characteristic that introduces the most inconsistency depending on how the system data is constructed.

2.6.3 The Cigré C4.103 working group

The C4.103 [27] Cigré joint working group was established to evaluate, simplify, and supplement the recommendations set forth by the IEC. This assessment methodology builds on the basic concepts presented in the IEC 61000 standards.

The C4.103 working group reported on both the statistical harmonic assessment method described by the IEEE-519 and the comprehensive emission allocation method presented in the IEC 61000-3-6. This will, therefore, not be discussed further as both methods are implemented with the same fundamental principles.

2.6.4 The Cigré C4.109 working group

Contrary to the simplified, summative report delivered by the C4.103 working group, the C4.109 [28] working group presents a compliance assessment methodology that attempts to discriminate between harmonic sources, therefore identifying “network” and “customer” harmonic emissions. Three assessment methods will be reviewed that do not primarily rely on statistical analysis of harmonic measurements.

The use of weekly 10-minute data is recommended in the report as the index for comparing harmonic emission limits. This is allowed as [25] requires that either 10-minute, 3-second or both be evaluated against the appropriate harmonic limits.

One-shot harmonic emission evaluation

The equivalent circuit for establishing the individual harmonic emission contributions is illustrated in Fig. 2-7.

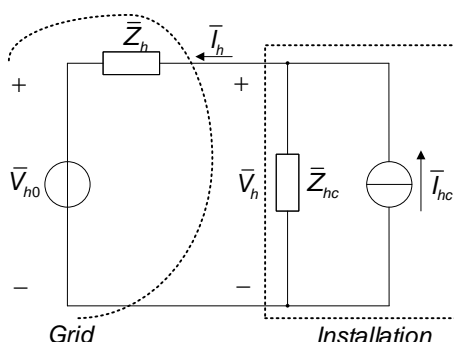


Fig. 2-7. Equivalent harmonic contribution circuit for grid and installation

From Fig. 2-7 the value of the current harmonic emission can be calculated as follows:

$$\bar{I}_h = \bar{I}_{hc} \cdot \frac{\bar{Z}_{hc}}{\bar{Z}_h + \bar{Z}_{hc}} - \frac{\bar{V}_{h0}}{\bar{Z}_h + \bar{Z}_{hc}} \quad (2.19)$$

where I_h is the current harmonic emission at the POE, I_{hc} is the harmonic current contribution of the installation, Z_{hc} is the installation harmonic impedance, Z_h is the network Thevenin equivalent impedance and V_{h0} is the background harmonic voltage distortion.

The installation's harmonic voltage emission contribution can further be calculated using the following:

$$\bar{V}_{hc} = \bar{Z}_h \bar{I}_h = \bar{V}_h - \bar{V}_{h0} \quad (2.20)$$

which intuitively reveals that the installation harmonic voltage distortion, as measured at the POE, can be ignored at harmonic frequencies where the installation has a smaller magnitude than the background harmonic voltage (V_{h0}). A negative voltage contribution would indicate that the installation is absorbing harmonic current and can therefore be exempted from assessment.

Conclusion

The one-shot emission evaluation method is conducted to provide instantaneous results regarding whether the installation is contributing towards the harmonic voltage. This assessment is conducted with the installation disconnected and then reconnecting it. This instantaneous connection of the installation allows for the assumption that the network impedance is constant between the two consecutive measurements.

There is, however, no statistical significance to this assessment as the operating condition of the network and the installation are not constant throughout its operation.

Dominant disturber assessment

When the installation under investigation is the dominant contributor towards harmonic voltage emissions at the POE the harmonic voltage is expected to correlate linearly with the apparent power. This correlation concept is illustrated in Fig. 2-8.

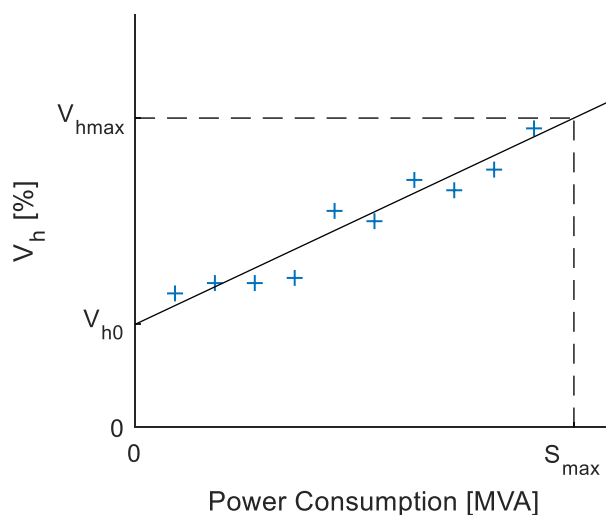


Fig. 2-8. Apparent power consumption vs voltage emission level correlation

From Fig. 2-8 the correlation between the apparent power consumption and the voltage emission level, observed at the POE, can be utilised to extrapolate the background harmonic voltage distortion (V_{h0}) at zero power consumption. This assessment can therefore be made with the installation connected to the network and does not require disconnecting the installation. The harmonic contribution of the installation can be calculated using the statistical summation law as follows:

$$V_{hc} = \sqrt[\alpha]{V_h^\alpha - V_{h0}^\alpha} \quad (2.21)$$

where α considers the probability that either the measured harmonic emission value or background harmonic voltage distortion value will vary from the calculated value or differ in magnitude and phase angle.

Conclusion

The dominant disturber method provides a statistical method for assessing the harmonic voltage contribution of the installation without requiring system impedance data, as it intrinsically accounts for changes in the harmonic impedance. If the background harmonic voltage distortion varies significantly, it can also be approximated using a 95th percentile statistical value.

The major problem with this evaluation method is that it only produces coherent results if the installation being considered is a dominant contributor to the global distortion at the POE. Datapoints would be too scattered to extrapolate a significant best-fit line in which case the background harmonic voltage could not be approximated.

Impedance correlation assessment

Harmonic voltage and current measurements are taken simultaneously at the POC to establish a correlating harmonic impedance slope over several measurements. The determinant impedance slopes are obtained from calculated network and installation harmonic impedances. The installation harmonic impedance is, however, typically assessed using the installation's main transformer impedance.

Considering the same simplified circuit presented in Fig. 2-7 the correlating slope can be determined from dominant contributing sources by applying superposition, as illustrated in Fig. 2-9.

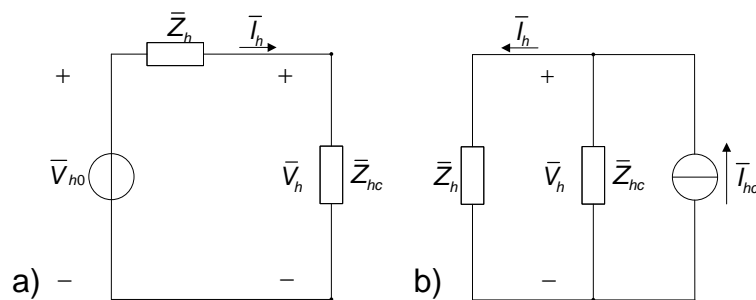


Fig. 2-9. a) Network b) Installation dominant contributor source simplified circuits

As the concept is built on a dominant source the impedance slope evaluated at the POE for each circuit is defined as:

$$\begin{aligned}
 \bar{V}_h &= \bar{V}_{h0} \cdot \frac{\bar{Z}_{hc}}{\bar{Z}_h + \bar{Z}_{hc}} \\
 \bar{I}_h &= \frac{\bar{V}_{h0}}{\bar{Z}_h + \bar{Z}_{hc}} \\
 \bar{Z}_{POE} &= \frac{\bar{V}_h}{\bar{I}_h} = \frac{\bar{V}_{h0} \cdot \frac{\bar{Z}_{hc}}{\bar{Z}_h + \bar{Z}_{hc}}}{\frac{\bar{V}_{h0}}{\bar{Z}_h + \bar{Z}_{hc}}} = \bar{Z}_{hc}
 \end{aligned} \tag{2.22}$$

for the dominant network contribution circuit Fig. 2-9 a). And defined as:

$$\begin{aligned}\bar{V}_h &= \bar{I}_{hc} \cdot \frac{\bar{Z}_h \cdot \bar{Z}_{hc}}{\bar{Z}_h + \bar{Z}_{hc}} \\ \bar{I}_h &= \bar{I}_{hc} \cdot \frac{\bar{Z}_{hc}}{\bar{Z}_h + \bar{Z}_{hc}} \\ \bar{Z}_{POE} &= \frac{\bar{V}_h}{\bar{I}_h} = \frac{\bar{I}_{hc} \cdot \frac{\bar{Z}_h \cdot \bar{Z}_{hc}}{\bar{Z}_h + \bar{Z}_{hc}}}{\bar{I}_{hc} \cdot \frac{\bar{Z}_{hc}}{\bar{Z}_h + \bar{Z}_{hc}}} = \bar{Z}_h\end{aligned}\quad (2.23)$$

for the dominant installation contribution circuit Fig. 2-9 b). From (2.22) and (2.23) it can be seen that the dominant impedance observed at the POE provides an indication of which harmonic source is dominant. The implementation of impedance slopes can be visualised as seen in Fig. 2-10.

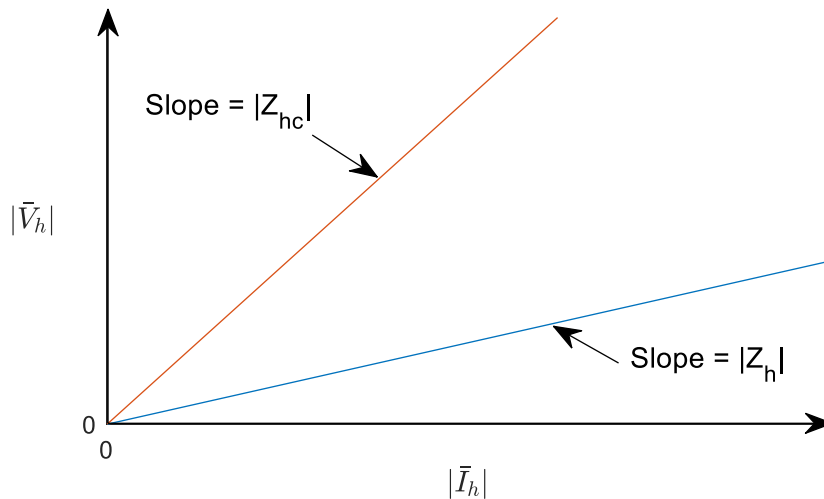


Fig. 2-10. Harmonic impedance slopes of dominant harmonic contributing sources

Evaluating short 10-minute rms current and voltage values and plotting them against the dominant impedance slopes illustrated in Fig. 2-10 reveals the dominant source of the observed harmonic resonance. This method can result in one of the following:

- The values correlate with the installation impedance slope indicating that the network is the primary contributor of harmonics and the installation is “absorbing” harmonics from the network.
- The values correlate with the network impedance slope indicating that the installation is the primary contributor of harmonics and the installation is “injecting” harmonics into the network.
- The values do not correlate with either of the impedance slopes with a spread between the two slopes indicating a combined influence of both the installation and the network.

This assessment was applied to an RPP system with results reported in [32] which reveals the limitation of using this assessment technique over a long time period.

Conclusion

The impedance correlation method is supported by the derivations provided in (2.22) and (2.23). It presents a statistical analysis methodology which assesses the correlation of the measured data to the harmonic impedance slopes illustrated in Fig. 2-10. It has the advantage of only requiring the harmonic voltage and current magnitudes to evaluate the correlation.

The method is, however, flawed as it requires that the installation and network impedances remain constant for the duration of the assessment which is typically done over a 7-day period. This assessment methodology is therefore more applicable to networks that do not experience significant variations in harmonic impedance. The implementation of the installation's main transformer impedance to represent the installation impedance slope is also problematic as it ignores any possible resonance that is introduced by capacitive elements connected within the installation.

2.7 Power system modal analysis

The study of the modal domain has been documented in developing methods to decouple linear time-invariant systems using selective modal analysis in electric power systems [33]. The implementation of modal analysis was, however, more significant in the field of small-signal stability producing uncoupled, linear state equations, easing the assessment of stability problems in large power systems [34].

These studies introduced eigenvalue matrices and eigenvectors, obtained through eigenvalue decomposition, used to transform the system state equations. The combination of the system's left and right eigenvectors produces the participation matrix allowing for the relationship between modes and state variables to be identified.

The concept of harmonic RMA was first introduced in [35] which presented the uncoupling of the system's admittance matrix using the same matrix modal transformation described in [33] and [34]. This is fundamentally different from the state variable decoupling of the differential equations presented in [34] as it is applied to a dynamic frequency-dependant linear system matrix instead. The eigenvalues describe the natural resonant modes of the admittance matrix and can be described through eigenvalue decomposition as follows:

$$Y = \Psi \Lambda \Phi \quad (2.24)$$

where Y is the admittance matrix, Ψ is the left eigenvector, Λ is the eigenvalue matrix and Φ is the right eigenvector. The implementation of RMA was further investigated to analyse the sensitivity of

eigenvalues to system shunt and series components in [36] through the use of bus participation factors (PFs).

The implementation of RMA in the renewable energy sector is presented in [37] to address resonant conditions introduced by the inclusion of multiple parallel inverters connected to the power system. The dynamics of a large RPP can be identified through the modal analysis as it reveals how the resonant modes change with the connection and disconnection of parallel inverters. In [37] the influence of various inverter components to resonant modes were investigated and revealed that certain resonant modes were more sensitive to the inverter equivalent input admittance value.

The study conducted in [37] revealed the importance of including the filter components within an inverter model's input admittance as these parameters were found to influence system resonant conditions. The topic of RMA is further investigated in detail in this thesis.

2.8 Conclusion

The uptake of renewable energy resources warrants the need for QoS impact assessments. Harmonic generating mechanisms of VSDs and inverters, introduced by RPPs installations, illustrated how harmonic content gets emitted into the power system at baseband and switching frequencies.

The system impedance determines how harmonic current emissions propagate and how resonant conditions amplify or attenuate harmonic voltage distortion throughout the power system.

Harmonic assessment methodologies provided by the IEEE and IEC could not determine the dominant contributors of specific harmonic measurements under resonant conditions. The Cigré group, however, provided further methods for evaluating the source of specific harmonics. The Cigré working group C4.109 suggested practical assessment techniques implementing statistically significant results to analyse and determine dominant contributors of harmonic measurements at a POE.

The biggest problem with the suggested harmonic assessment techniques is that resonant conditions significantly influence the results and would therefore need to be accurately determined. RMA as a method for identifying and quantifying the contributions of various nodes in a system to a resonant condition was identified as a possible approach to analysing resonant conditions.

The cause of resonant conditions will be investigated in detail in this thesis along with the evaluation of resonant conditions using RMA.

3 Simplified RPP Installation Single-Phase Equivalent Circuit Development

This chapter covers the process of developing a single-phase equivalent model used to represent an RPP. The simplifications and assumptions that are made are discussed and applied towards a case study RPP. The simplified model is developed in Simulink and compared to a detailed installation model developed in PowerFactory.

3.1 Introduction

A RPP was simplified to reduce the complexity of modelling transfer functions to represent harmonic propagation throughout the system. When modelling a large-scale RPP, the number of parallel branches operating independently leads to computational challenges, requiring numerous transfer functions to be solved.

The parallel branches were reduced to a single aggregated branch to represent the entire RPP. The single branch equivalent representation was used to develop generalized transfer functions that represent the approximation of the harmonic propagation between the network and the RPP during full operation.

This chapter was covered in the peer-reviewed ICREPQ publication [38], with alterations to the three-winding transformer modelling methodology.

3.2 RPP Modelling

3.2.1 Overview

The installation considered for this section is a concentrated photovoltaic RPP. The installation is rated at 40 MVA and connected to the grid at a high voltage of 132 kV. The layout of the RPP is illustrated in Fig. 3-1 which also illustrates the various parallel branches typically associated with an RPP.

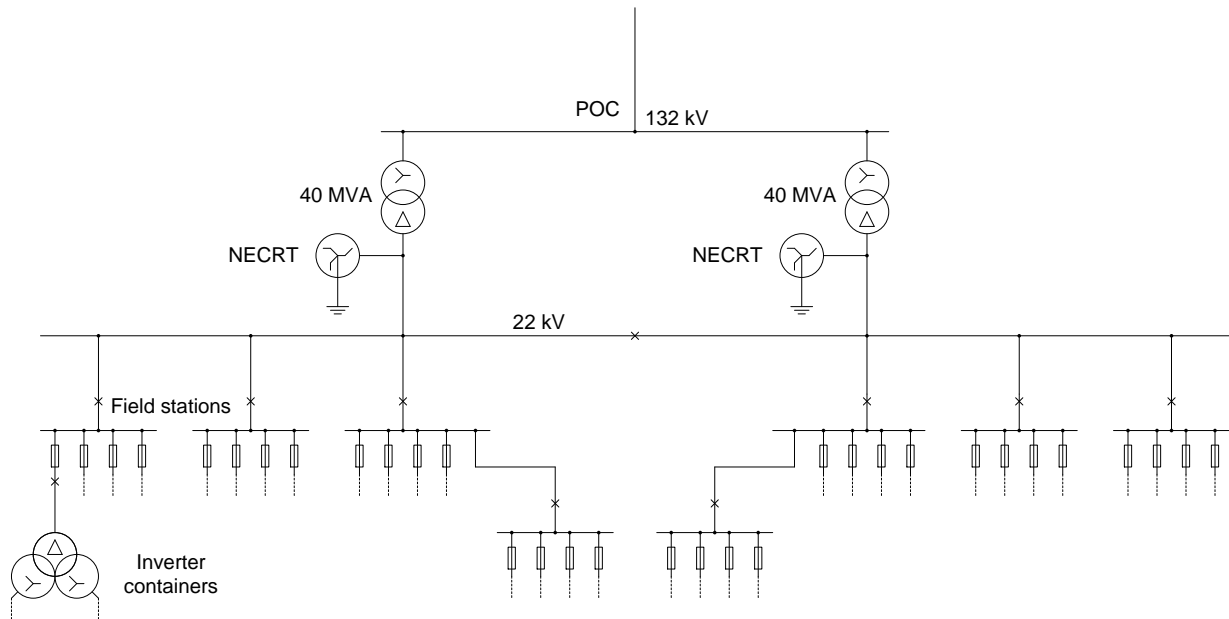


Fig. 3-1. Overview of a typical 40MVA RPP

The investigated installation had 30 inverter containers installed (a maximum capacity of 32) each containing two 750 kVA inverters connected to a mutual 1450 kVA, 0.3/22 kV three-winding transformer. Short low voltage (LV) cables connect the inverters to the transformer and are located inside the inverter containers. These cables are of insignificant length and are therefore ignored.

The medium voltage (MV) field stations, operating at 22 kV, contain 630 A isolators and 100 A fuses for each connected inverter container. A 630 A circuit breaker was included for the main outgoing connection.

The outgoing connections of the MV field stations is connected to the main 40 MVA, 22/132 kV transformer through MV cabling. A neutral earthing compensator (NEC) with neutral earthing resistor (R) and auxiliary transformer (T) is connected to the 22kV MV line to provide a neutral point to the delta configuration of the system limiting the earthing resistance to prevent high earth fault currents. This NECRT affects zero-sequence currents and can therefore be ignored for positive- and negative sequence harmonic currents.

This overview layout was subdivided into the various components that were connected to each branch of the installation, illustrated in Fig. 3-1. An equivalent aggregated element model for a single-phase equivalent representation of the installation was developed as per the components from Fig. 3-1.

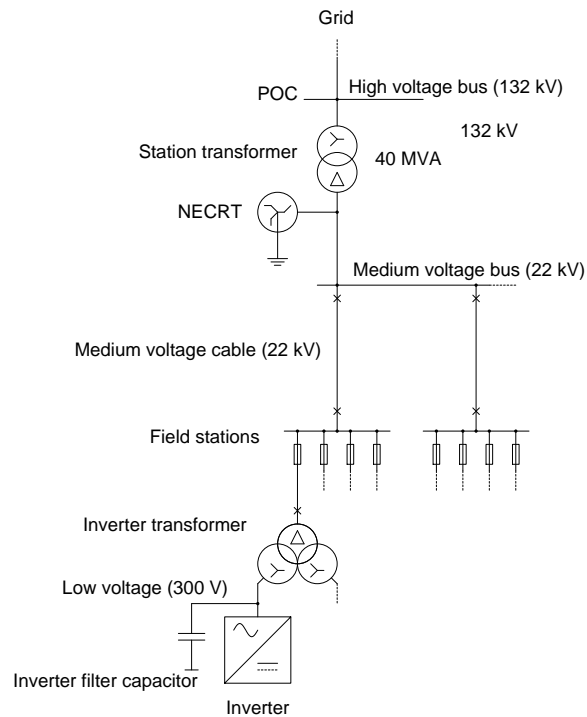


Fig. 3-2. Detailed overview of a single branch

3.2.2 Modelling assumptions and simplifications

When modelling a large system, the order of the system equation is a function of the number of shunt reactive components. A typical RPP consist of various parallel branches leading to a higher order system equation that becomes difficult to evaluate.

Reducing the order of a large system requires that certain assumptions and simplifications be made. Considering a typical RPP model as seen in Fig. 3-2, the various variable parallel branches can be identified. These components are calculated according to their respective rated values. The system component values were calculated starting from the connected grid network and working towards the inverter filter capacitor.

Grid

The connected grid network system has many interconnected power sources, transmission lines and reactive ancillary equipment contributing towards a complex system impedance. Various configurations can therefore be assumed for the system with a radial system impedance configuration being the simplest. For a linear impedance configuration, the grid impedance is defined as:

$$Z_s = R_s + jX_s = R_s + j\omega L_s \quad (3.1)$$

Another configuration that will be a complex loop-network system configuration that introduces additional network components, allowing for the introduction of existing network resonances due to ancillary equipment found on a typical network. This complex configuration is of a higher order and will be subjected to additional parameters that will be discussed in Chapter 7.

Main station transformer

The main 40 MVA, 22/132 kV transformer is a three-phase, two-winding transformer which is schematically represented using three single-phase transformers that are phase-shifted by 120 degrees. The complete representation, per phase, is illustrated in Fig. 3-3 a).

Since the transformer efficiency and excitation current phenomena are not of concern, due to the low percentage of rated current (less than 5%) used for excitation, the shunt resistance and inductance representing the core and magnetization losses can be neglected [1]. Stray capacitances are also neglected as assessment is only done up to the 50th harmonic (2500 Hz) and transformers can generally be modelled as an inductive component with resistive damping [39]. The model that will be considered for the main transformer is seen in Fig. 3-3 b).

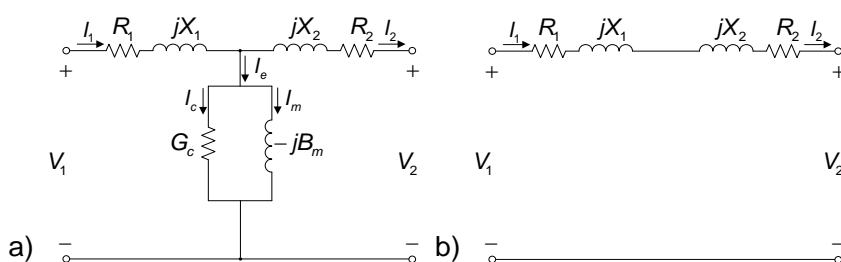


Fig. 3-3. a) Complete and b) neglecting excitation current representations of a single-phase two-winding transformer

The station transformer impedance is defined as:

$$Z_{st} = R_{st} + jX_{st} = R_{st} + j\omega L_{st} \quad (3.2)$$

Grounded medium voltage cable

Grounded MV cables of various lengths are used in a typical RPP. An appropriate length for calculating the aggregated model representation needed to be established. Since these cables are mostly short, grounded cables an aggregated circuit model will be adequate for modelling the cables. An aggregated shunt admittance, T circuit or π circuit model can be implemented.

Due to the insignificance of the inductance of these cables relative to the inductance of the transformers only the capacitive element will be considered represented by a single shunt capacitance using the shunt admittance model, as seen in Fig. 3-4.

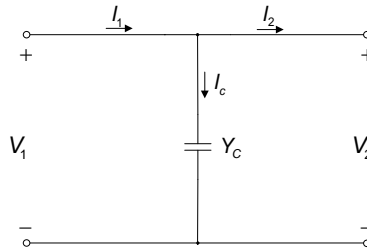


Fig. 3-4. Cable shunt admittance circuit

The MV cabling impedance is defined as:

$$Z_c = jX_c = -j \frac{1}{\omega C_c} \tag{3.3}$$

Inverter transformer

The inverter transformer is a three-winding transformer connected to two synchronized inverters. This three-winding transformer will be reduced to the same model as the main station transformer. As seen in Fig. 3-5, some additional calculations are required to reduce the two parallel windings connected to the inverters, as seen in Fig. 3-5 b).

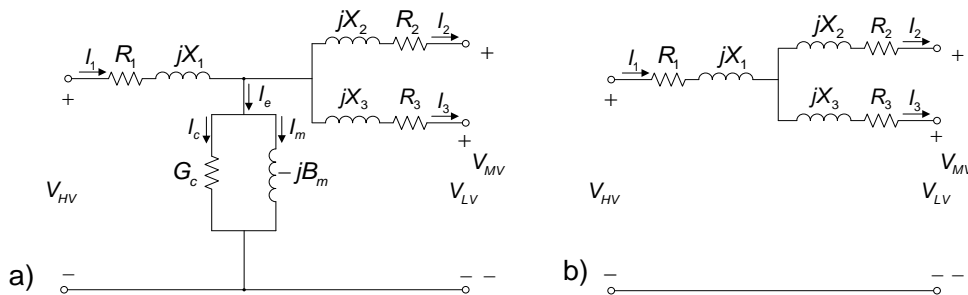


Fig. 3-5. Detailed three-winding transformer a) and simplified three-winding transformer b)

The inverter transformer impedance is defined as:

$$Z_s = R_{it} + jX_{it} = R_{it} + j\omega L_{it} \tag{3.4}$$

Inverter

As a VSI controls the output current through its low-pass filter it operates as a current source [40]. The low-pass filter inductor of an LC inverter can generally be excluded from the model, but the filter capacitor needs to be included as it contributes towards the dynamic effect of the installation's impedance and represents the inverters parallel admittance [41]. The Norton equivalent circuit for a single VSI can be modelled as illustrated in Fig. 3-6.

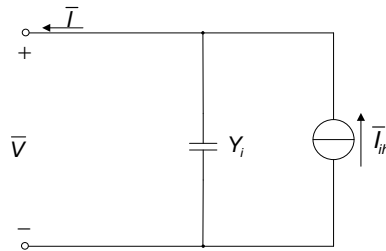


Fig. 3-6. VSI circuit representation

The inverter impedance is defined as:

$$Z_i = jX_i = -j \frac{1}{\omega C_i} \quad (3.5)$$

3.2.3 Model parameter calculations

Now that the conditions under which the simplified model will be developed have been established the parameters for the simplified single-phase equivalent model, as illustrated in Fig. 3-7, can be calculated.

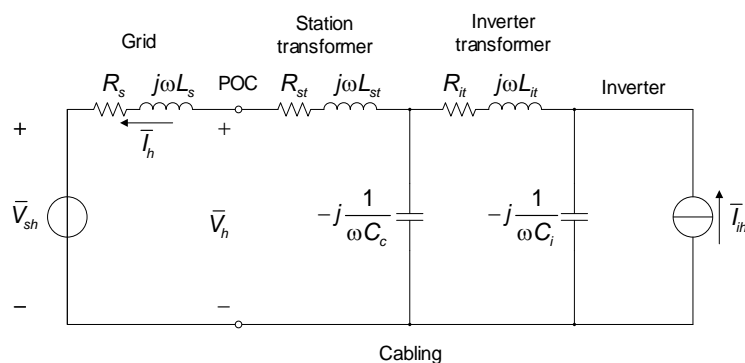


Fig. 3-7. Simplified aggregated element single-phase equivalent model of an RPP installation

Grid

The installation is connected to the grid at 132 kV and is modelled using the Thevenin equivalent representation with a single voltage source and series impedance. Specific parameters for the network impedance are obtained from the national service provider or extrapolated from available network data. The network impedance was provided as follows for the 50 Hz component:

$$\begin{aligned} R_s &= 8.39 \, \Omega \\ X_s &= 21.7 \, \Omega \\ \Rightarrow L_s &= \frac{21.7}{100\pi} = 69 \, \text{mH} \end{aligned} \quad (3.6)$$

Main station 2-winding transformer

The station transformer is rated for 40 MVA at 132 kV which is the base voltage (V_{base}). The rated current for the station transformer is defined as:

$$I_{st} = \frac{40 \cdot 10^6}{\sqrt{3} \times 132 \cdot 10^3} = 175 \, \text{A} \quad (3.7)$$

The transformer is defined as having a 11.5% impedance rating leading to the calculation for the voltage drop defined as:

$$V_{11.5\%} = 0.115 \times \frac{132 \cdot 10^3}{\sqrt{3}} = 8760 \, \text{V} \quad (3.8)$$

The station transformer impedance can now be calculated as follows:

$$Z_{st} = \frac{V_{11.5\%}}{I_{st}} = \frac{8670}{175} = 50 \, \Omega \quad (3.9)$$

Using the copper losses of the three-phase transformer, rated at 200 kW (66.7 kW per phase) the transformer's equivalent single-phase series resistance is calculated as:

$$R_{Cu, st} = \frac{P_t}{I_{st}^2} = \frac{1}{3} \times \frac{200 \cdot 10^3}{175^2} = 2.177 \, \Omega \quad (3.10)$$

The inductance per phase can now be calculated using the values from (3.9) and (3.10) as follows:

$$\begin{aligned} X_t &= \sqrt{Z_{st}^2 - R_{Cu, st}^2} = \sqrt{50^2 - 2.177^2} = 49.95 \, \Omega \\ \Rightarrow L_{\sigma, st} &= \frac{X_t}{\omega} = \frac{49.95}{100\pi} = 159 \, \text{mH} \end{aligned} \quad (3.11)$$

Medium voltage cables

There are 8 MV field stations that spur MV cables towards the main transformer. Additionally, 30 inverter containers are connected to these field stations. The average length between an inverter container and the main station transformer was determined to be approximately 0.7 km with a capacitance of 0.192 $\mu\text{F}/\text{km}$. The cable capacitance, as transformed to the 132 kV side is calculated as follows:

$$C_c = 30 \times 0.7 \times 0.192 \cdot 10^{-6} \times \frac{22^2}{132^2} = 112.5 \text{ nF} \quad (3.12)$$

Inverter three-winding transformer

The inverter transformer located inside the inverter containers transforms two inverter's output voltage from 300 V to 22 kV for transmission through the MV cables. Each of the two secondary windings are rated for 725 kVA and have a rated current at the HV side as follows:

$$I_{it} = \frac{725 \cdot 10^3}{\sqrt{3} \times 22 \cdot 10^3} = 19 \text{ A} \quad (3.13)$$

The inverter transformer is rated for a 5.59% impedance. At rated current this impedance rating would produce a voltage drop as follows:

$$V_{5.59\%} = 0.059 \times \frac{22 \cdot 10^3}{\sqrt{3}} = 710 \text{ V} \quad (3.14)$$

Using the values from (3.13) and (3.14) the impedance between the HV and MV/LV terminals can be calculated as follows:

$$Z_{HV-MV} = \frac{V_{5.59\%}}{I_{it}} = \frac{710}{19} = 37.37 \Omega \quad (3.15)$$

Using the copper losses between the primary HV and secondary MV/LV terminals of the three-phase transformer, rated at 6.5 kW (2.16 kW per phase), the transformer's equivalent single-phase series resistance between these terminals is calculated as:

$$R_{Cu, HV-MV} = \frac{P_{Cu, HV-MV}}{I_{it}^2} = \frac{1}{3} \times \frac{6500}{19^2} = 6 \Omega \quad (3.16)$$

Using the values from (3.15) and (3.16) the transformer inductance can be calculated as follows:

$$\begin{aligned} X_{\sigma, HV-MV} &= \sqrt{Z_{HV-MV}^2 - R_{Cu, HV-MV}^2} = \sqrt{37.37^2 - 6^2} = 36.89 \Omega \\ \Rightarrow L_{\sigma, HV-MV} &= \frac{X_{\sigma, HV-MV}}{\omega} = \frac{36.89}{100\pi} = 117.4 \text{ mH} \end{aligned} \quad (3.17)$$

At rated current a voltage drop of 9.7% is experienced between the two secondary LV/MV terminals leading to a voltage drop as follows:

$$V_{9.7\%} = 0.097 \times \frac{22 \cdot 10^3}{\sqrt{3}} = 1232 \text{ V} \quad (3.18)$$

The impedance between the two secondary winding terminals is calculated as follows:

$$Z_{MV-LV} = \frac{V_{9.7\%}}{I_{it}} = \frac{1232}{19} = 64.85 \Omega \quad (3.19)$$

Using the copper losses between the two secondary terminals of the three-phase transformer, rated at 7.9 kW (2.633 kW per phase) the transformer's equivalent single-phase series resistance between these terminals are calculated as:

$$R_{Cu, MV-LV} = \frac{P_{Cu, MV-LV}}{I_{it}^2} = \frac{1}{3} \times \frac{7900}{19^2} = 7.3 \Omega \quad (3.20)$$

Using the values from (3.19) and (3.20) the transformer inductance can be calculated as follows:

$$\begin{aligned} X_{\sigma, MV-LV} &= \sqrt{Z_{MV-LV}^2 - R_{Cu, MV-LV}^2} = \sqrt{64.85^2 - 7.3^2} = 64.43 \Omega \\ \Rightarrow L_{\sigma, MV-LV} &= \frac{X_{\sigma, MV-LV}}{\omega} = \frac{64.43}{100\pi} = 205.1 \text{ mH} \end{aligned} \quad (3.21)$$

Using (3.16), (3.17), (3.20) and (3.21) the individual winding impedances can be calculated as follows:

$$\begin{aligned} R_2 = R_3 &= 0.5 \times R_{Cu, MV-LV} = 0.5 \times 7.3 = 3.65 \Omega \\ L_2 = L_3 &= 0.5 \times L_{\sigma, MV-LV} = 0.5 \times 205.1 = 102.5 \text{ mH} \end{aligned} \quad (3.22)$$

and

$$\begin{aligned} R_1 &= R_{Cu, HV-MV} - R_2 = 6 - 3.65 = 2.35 \Omega \\ L_1 &= L_{\sigma, HV-MV} - L_2 = 0.1174 - 0.1025 = 14.9 \text{ mH} \end{aligned} \quad (3.23)$$

The transformer winding impedances are aggregated and transformed to the 132 kV to obtain the equivalent transformer series impedance. The equivalent aggregated impedance has 30 parallel three-winding transformers with 30 primary windings and 60 secondary windings that when combined result in the following:

$$L_{it} = \frac{132^2}{22^2} \cdot \left(\frac{L_1}{30} + \frac{L_2}{60} \right) = \frac{132^2}{22^2} \cdot \left(\frac{14.9 \cdot 10^{-3}}{30} + \frac{102.5 \cdot 10^{-3}}{60} \right) = 79.38 \text{ mH}$$

$$R_{it} = \frac{132^2}{22^2} \cdot \left(\frac{R_1}{30} + \frac{R_2}{60} \right) = \frac{132^2}{22^2} \cdot \left(\frac{2.35}{30} + \frac{3.65}{60} \right) = 5.01 \Omega$$
(3.24)

Inverter

The installation has 60 operating inverters each with 400 μF capacitors connected in a delta configuration in its low pass LC filter. The aggregated equivalent value for the capacitance as transformed to the 132 kV side is calculated as follows:

$$C_i = 3 \times 60 \times \frac{0.3^2}{132^2} \times 400 \cdot 10^{-6} = 0.3719 \mu\text{F}$$
(3.25)

3.2.4 Summary

To summarize, the values that will be implemented for the simplified aggregated model's components, as illustrated in Fig. 3-7, are indicated in Table VI below.

Table VI: Parameters for simplified installation model

Installation parameter	Value
<i>Network inductance (L_s)</i>	69 mH
<i>Network resistance (R_s)</i>	8.39 Ω
<i>Station transformer inductance (L_{st})</i>	159 mH
<i>Station transformer resistance (R_{st})</i>	2.177 Ω
<i>Cable capacitance (C_c)</i>	112.5 nF
<i>Inverter transformer inductance (L_{it})</i>	79.38 mH
<i>Inverter transformer resistance (R_{it})</i>	5.01 Ω
<i>Inverter filter capacitance (C_i)</i>	371.9 nF

3.3 Developed model validation

The simplified model of the RPP installation and network developed in the previous sections is implemented in a MATLAB Simulink model, as illustrated in Fig. 3-8. Implementing the calculated values, as indicated in Table VI, this model will be verified against a detailed PowerFactory model.

The criteria for validating the developed model includes obtaining a similar frequency domain impedance relative to the complete installation as modelled in PowerFactory. The frequency sweep is performed at the POC as the aggregated installation representation would have to correlate with the detailed model to provide similar results.

Some discrepancies are expected due to the nature of the assumptions made for the simplification of the installation. Damping of resonant frequencies is subjected to many dynamic characteristics found in the installation.

3.3.1 MATLAB Simulink model

The frequency sweep impedance of the developed Simulink model is determined at the POC, as indicated in Fig. 3-8.

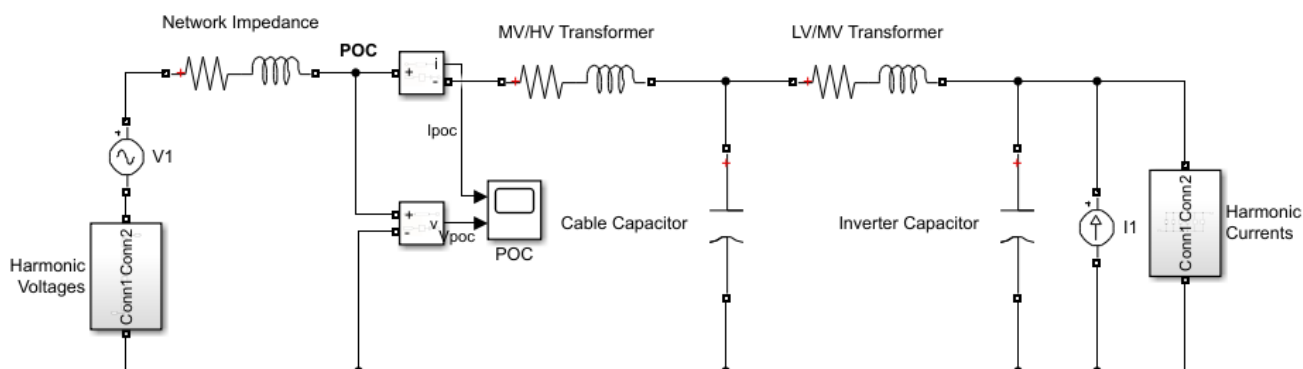


Fig. 3-8. Simulink model of simplified installation and network

The result of the frequency sweep impedance is illustrated in Fig. 3-9.

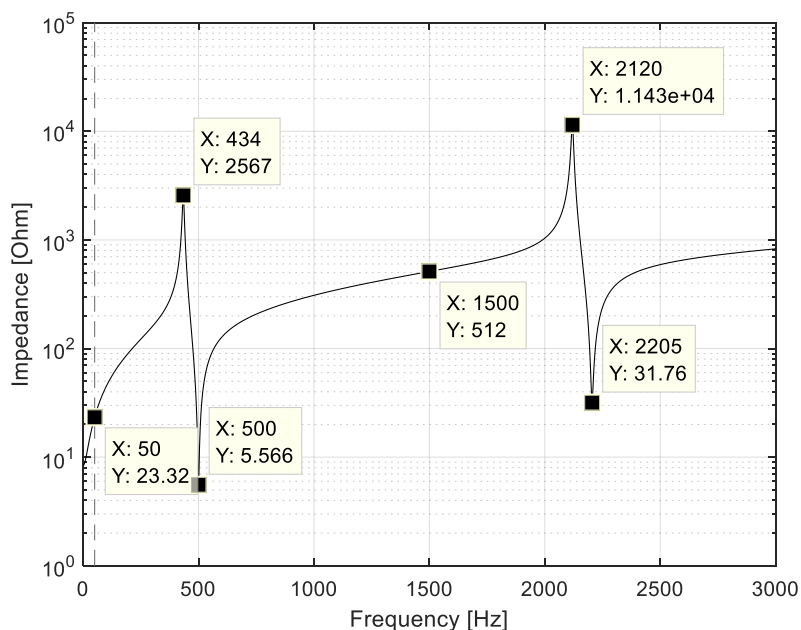


Fig. 3-9. Frequency sweep impedance as seen at the POC of the Simulink model

This result can be summarised considering only the relevant resonant frequencies as the impedance is subjected to the plot's resolution, as illustrated in Table VII below.

Table VII: Frequency summary of simplified Simulink model

Frequency	Magnitude
50 Hz	23.32 Ω
434 Hz	2567 Ω
500 Hz	5.566 Ω
1500 Hz	512 Ω
2120 Hz	11.43 k Ω
2205 Hz	31.76 Ω

3.3.2 PowerFactory model

The complete PowerFactory model has the configuration as seen in Fig. A-8-3. This detailed model has individual values for each branch's MV cables whilst maintaining the same parameters for matching equipment.

Performing power flow analysis in PowerFactory the frequency sweep impedance is determined at the POC as illustrated in Fig. 3-10.

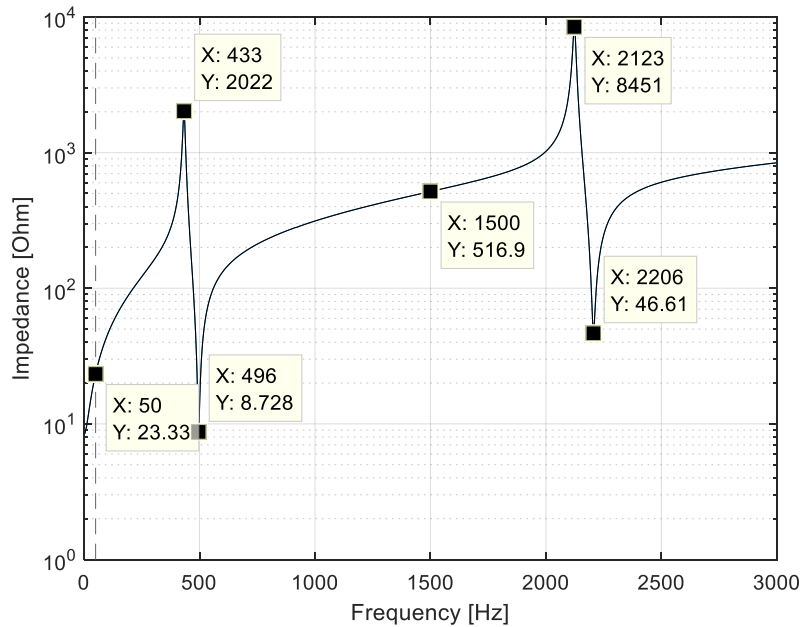


Fig. 3-10. Frequency sweep impedance as seen at the POC of the detailed PowerFactory model

These results are summarised using the resonant frequency values, as illustrated in Table VIII.

Table VIII: Frequency summary of detailed PowerFactory model

Frequency	Magnitude
50 Hz	23.33 Ω
433 Hz	2022 Ω
496 Hz	8.728 Ω
1500 Hz	516.9 Ω
2123 Hz	8451 Ω
2206 Hz	46.61 Ω

3.3.3 Simulink and PowerFactory model comparison

Comparing the results from Table VII and Table VIII in Table IX it can be seen that the resonant frequencies are very close to one another as well as the magnitudes of the additional frequency points. This indicates that the reactive elements of the simplified aggregated model are accurate as these elements contribute towards the resonant frequencies.

Table IX: Simulink and PowerFactory frequency and impedance comparison

Frequency (Simulink/PowerFactory)	Magnitude (Simulink/PowerFactory)
50 Hz	23.32 Ω / 23.33 Ω
434/433 Hz	2567 Ω / 2022 Ω
500/496 Hz	5.566 Ω / 8.728 Ω
1500 Hz	512 Ω / 516.9 Ω
2120/2123 Hz	11.43 k Ω / 8451 Ω
2205/2206 Hz	31.76 Ω / 46.61 Ω

The damping that is present in each model differs slightly. While the various damping elements presented in the aggregated model were approximated using rated values some of these parameter values are specified in the PowerFactory model. Some factors that introduce additional damping, such as the cable resistance, were also excluded from the simplified model relative to the more detailed PowerFactory model.

3.4 Conclusion

The process for modelling the simplified aggregated representation of the RPP under investigation was elaborated. Assumptions and simplifications were provided to form a basis from which the simplified Simulink model was developed. The results obtained in Section 3.3 proved that the simplified aggregated model represents the detailed model accurately with only slight frequency and damping variations throughout the investigated frequency spectrum.

The aggregated model provides a simplified system approach to analysing harmonic resonance and will be further investigated in Chapter 5 to identify specific components contributing more significantly to resonant conditions.

4 Resonance Analysis of a Simplified RPP Installation Circuit

This chapter covers the frequency domain analysis applied to the simplified aggregated model developed in Chapter 3. Mathematical models for approximating resonant frequencies are presented using an impedance-based analytical approach. The accuracy of the mathematical models is compared to the simulation results obtained from the simplified Simulink model. Models depicting the propagation effect of identified resonant conditions are developed.

4.1 Introduction

A methodology for interpreting the resonant frequencies of the simplified aggregated model developed in Chapter 3 will be presented in this chapter. The accuracy will be compared to the measured resonant frequencies from the aggregated model, as these are the frequencies that will be approximated.

Being able to anticipate the frequencies at which possible harmonic resonances could occur and identifying key components in the installation that cause these resonances is of great importance for harmonic assessments. Some evaluation methods usually only consider the main transformer impedance to represent an installation which neglects any possible resonant conditions that are introduced by additional reactive components [28].

Transfer functions illustrating the contribution that two harmonic sources have at the POC bus will be developed to illustrate the effect that resonant conditions have on the propagation of harmonic sources.

In Chapter 2 it was found that RPPs introduce two capacitive elements that introduce additional resonant conditions. These elements were found to be introduced by the inverter filter capacitor and the cabling capacitance inherent to any RPP. Due to the nature of these elements, variations in the resonant conditions would fluctuate as the operating condition of the RPP changes over time. The effects and contribution of these variations to the resonant conditions will be investigated in this chapter.

4.2 Development of frequency domain impedance function

Considering the simplified aggregated model developed in Chapter 3 a mathematical function to represent the self-impedance of this system at the POC will be developed. This function will provide the necessary poles and zeros to identify high and low resonant conditions. Resistances will be neglected to simplify the equation as the resistive damping does not influence resonant frequencies significantly.

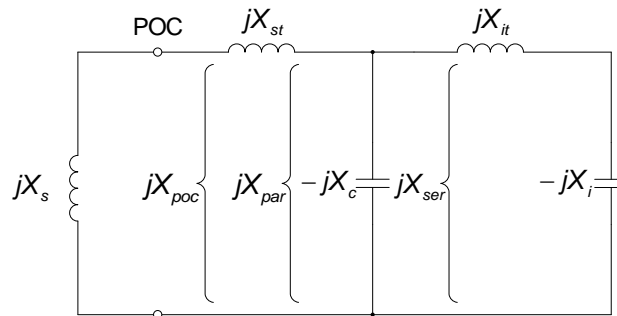


Fig. 4-1. System diagram for calculating POC driving point impedance

To determine the self-impedance, as seen from the POC, the simplified aggregated model will have to be evaluated from the POC as seen in Fig. 4-1. The first equation that will be developed is the inverter-side reactance (jX_{ser}) which includes the inverter-side transformer inductance (L_{it}) in series with the inverters' filter capacitors (C_i).

$$\begin{aligned}
 jX_{ser} &= j\omega L_{it} + \frac{1}{j\omega C_i} \\
 &= \frac{1 - \omega^2 L_{it} C_i}{j\omega C_i}
 \end{aligned} \tag{4.1}$$

The next part is the parallel combination (jX_{par}) of the inverter-side reactance (jX_{ser}) and the MV cable capacitance (C_c).

$$\begin{aligned}
jX_{par} &= \frac{1}{\frac{1}{jX_{ser}} + j\omega C_c} \\
&= \frac{1}{\frac{j\omega C_i}{1 - \omega^2 L_{it} C_i} + j\omega C_c} \\
&= \frac{1 - \omega^2 L_{it} C_i}{j\omega C_i + j\omega C_c (1 - \omega^2 L_{it} C_i)} \\
&= \frac{1 - \omega^2 L_{it} C_i}{j\omega (C_i + C_c) \left[1 - \omega^2 L_{it} \frac{C_i C_c}{C_i + C_c} \right]}
\end{aligned} \tag{4.2}$$

The final derived equation for the harmonic reactance as seen at the POC is the series combination of the installation-side reactance (jX_{par}) and the station transformer inductance (L_{st}) in parallel with the network reactance (L_s). This results in the following equation:

$$\begin{aligned}
jX_{POC} &= \frac{1}{\frac{1}{j\omega L_{st} + jX_{par}} + \frac{1}{j\omega L_s}} \\
&= \frac{1}{\frac{1}{j\omega L_{st} + \frac{1 - \omega^2 L_{it} C_i}{j\omega (C_i + C_c) \left[1 - \omega^2 L_{it} \frac{C_i C_c}{C_i + C_c} \right]}} + \frac{1}{j\omega L_s}} \\
&= j\omega L_s \frac{1 - \omega^2 \left[(L_{st} + L_{it}) C_i + L_{st} C_c (1 - \omega^2 L_{it} C_i) \right]}{1 - \omega^2 \left[(L_s + L_{st} + L_{it}) C_i + (L_s + L_{st}) C_c (1 - \omega^2 L_{it} C_i) \right]}
\end{aligned} \tag{4.3}$$

4.3 Resonant frequency assessment

From (4.3) significant poles and zeros can be determined that represent the frequencies where resonant conditions occur. Using (4.3) the resonant frequency at lower frequencies can be presented with the frequency dominant terms. At higher frequencies, all terms become imperative requiring an alternative solving methodology.

4.3.1 Low order resonance produced by inverter filter capacitor

When considering (4.3) for low frequency resonances the equation can be simplified to the following equation, assuming that $C_i \gg C_c$ which can be expected from a typical RPP:

$$jX_{poc} = j\omega L_s \frac{1 - \omega^2 [(L_{st} + L_{it})C_i]}{1 - \omega^2 [(L_s + L_{st} + L_{it})C_i]} \quad (4.4)$$

This equation ignores the values produced by the excluded terms at low frequencies ($\omega \rightarrow 0$) but still includes the dominant components causing the specified resonance. Applying the concept of assessment loops the dominant components causing the low order resonance can be illustrated as seen in Fig. 4-2.

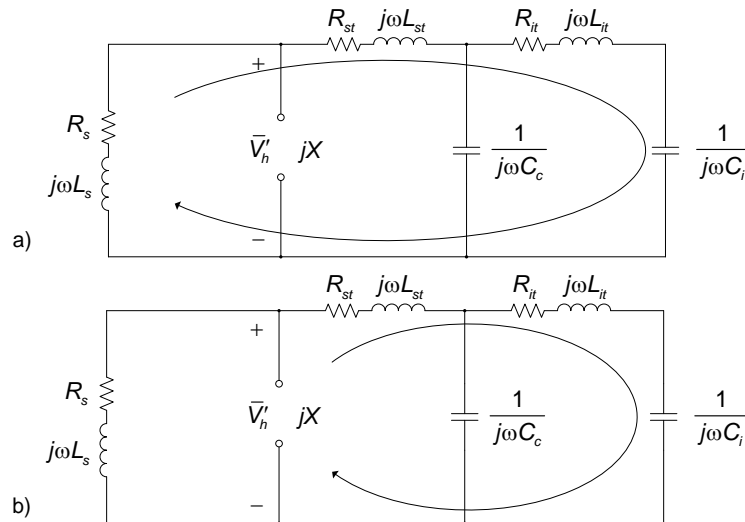


Fig. 4-2. Assessment loops of dominant elements causing low order a) parallel and b) series resonance

The first low order resonance is predominantly caused by the combination of the network, station transformer, inverter transformer and inverter capacitor reactances, as seen in Fig. 4-2 a). This assessment loop causes parallel resonance at the POE due to the network reactance being in parallel with the installation reactance from the POE's perspective. Using (4.4) the frequency at which this parallel resonance will occur is defined as:

$$1 - \omega_1^2 [(L_s + L_{st} + L_{it})C_i] \approx 0$$

$$\therefore \omega_1 \approx \frac{1}{\sqrt{(L_s + L_{st} + L_{it})C_i}} \quad (4.5)$$

The second distinct resonance that occurs is predominantly caused by the combination of the station transformer, inverter transformer and inverter capacitor reactances, as seen in Fig. 4-2 b). The assessment loop includes the POE within the loop and therefore has the equivalent components connected in series causing series resonance. Using the numerator of (4.4) the series resonance is defined as:

$$1 - \omega_2^2(L_{st} + L_{it})C_i \approx 0$$

$$\therefore \omega_2 \approx \frac{1}{\sqrt{(L_{st} + L_{it})C_i}} \quad (4.6)$$

The noticeable difference between the frequencies determined in (4.5) and (4.6) is the inclusion of the network line inductance that determines the difference between the low order parallel and series resonant frequencies. A weak network will have a parallel resonance lower in the frequency spectrum without influencing the series resonant condition.

4.3.2 High order resonance produced by cable capacitance

The anticipated higher order resonances occur at a frequency that makes the previously excluded term, $\frac{1}{j\omega C_c}$, significant and therefore requires the inclusion of this term to calculate the appropriate high order parallel and series resonant conditions. The assessment loops for both the series and parallel resonance can be represented as illustrated in Fig. 4-3.

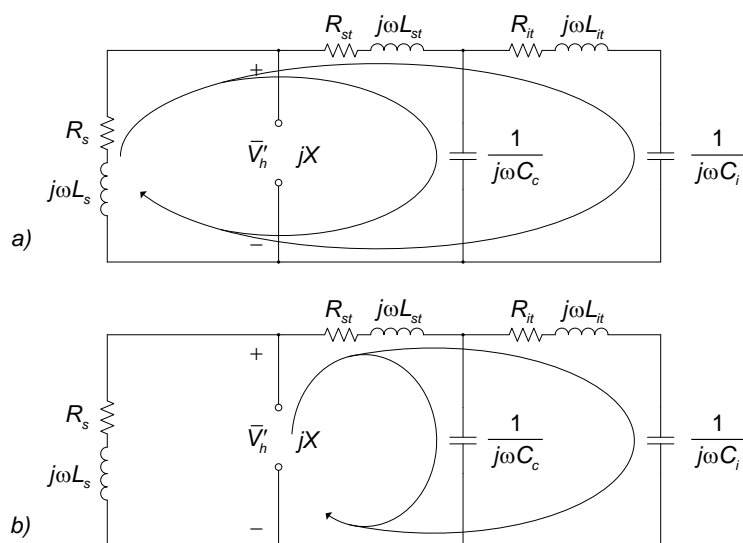


Fig. 4-3. Assessment loops of dominant elements causing high order parallel a) and series b) resonance

Solving the resonant frequencies requires that the 4th degree polynomials presented in the denominator and numerator of (4.3) be solved. This can be achieved by substitution and applying the quadratic formula since the order of the equations are multiples of a standard quadratic equation.

Considering the denominator of (4.3) the following resonant conditions are identified:

$$1 - \omega^2 [(L_s + L_{st} + L_{it})C_i + (L_s + L_{st})C_c(1 - \omega^2 L_{it}C_i)] = 0$$

substituting: $a = \omega^2$

$$1 - a[(L_s + L_{st} + L_{it})C_i + (L_s + L_{st})C_c(1 - aL_{it}C_i)] = 0 \quad (4.7)$$

$$a^2(L_s + L_{st})C_c(L_{it}C_i) - a[(L_s + L_{st} + L_{it})C_i + (L_s + L_{st})C_c] + 1 = 0$$

$$\therefore a = \frac{-[(L_s + L_{st})(C_i + C_c) + L_{it}C_i] \pm \sqrt{[(L_s + L_{st})(C_i + C_c) + L_{it}C_i]^2 - 4(L_s + L_{st})C_c(L_{it}C_i)}}{2(L_s + L_{st})C_c(L_{it}C_i)}$$

Using (4.7) the exact frequency at which the lower and higher order resonant conditions occur can be calculated.

Considering the numerator of (4.3) the following resonant conditions are identified:

$$1 - \omega^2 [(L_{st} + L_{it})C_i + L_{st}C_c(1 - \omega^2 L_{it}C_i)] = 0$$

substituting: $a = \omega^2$

$$1 - a[(L_{st} + L_{it})C_i + L_{st}C_c(1 - aL_{it}C_i)] = 0 \quad (4.8)$$

$$a^2 L_{it} L_{st} C_c C_i - a[(L_{st} + L_{it})C_i + L_{st}C_c] + 1 = 0$$

$$\therefore a = \frac{-[(L_{st} + L_{it})C_i + L_{st}C_c] \pm \sqrt{[(L_{st} + L_{it})C_i + L_{st}C_c]^2 - 4L_{it}L_{st}C_cC_i}}{2L_{it}L_{st}C_cC_i}$$

Substituting ω^2 back into a results in the angular resonant frequencies as follows:

$$\omega = \pm \sqrt{|a|} \quad (4.9)$$

The results of (4.9) provide the exact resonant frequency values of the modelled system. With all the system's reactive components included the results will reflect the system's resonant frequencies accurately. The effect of resistive damping components introduces slight deviations from the estimated frequency values but were deemed insignificant.

4.4 Simulation results comparison

To evaluate the resonant frequencies, calculated in (4.5) - (4.8), the tabulated simulation model values are implemented to determine the accuracy of the approximations. The results from (4.5) - (4.8) will be compared to those obtained in Section 3.3.1.

The results obtained from the simulation and the mathematical equations are illustrated in Table X.

Table X: Resonant frequencies from simulation versus estimations from equations (4.5) - (4.8)

Resonant frequency	Simulation	Estimates (4.5) - (4.6)	Estimates (4.7) - (4.8)
ω_1	434 Hz	470.7 Hz	434.2 Hz
ω_2	500 Hz	534.5 Hz	500 Hz
ω_3	2120 Hz	N/A	2120 Hz
ω_4	2205 Hz	N/A	2205 Hz

The approximated values for the first two lower order resonant frequencies have deviations from the simulated values. This is due to the exclusion of the cable capacitance's contribution in the simplified resonant frequency equations, (4.5) and (4.6). The accuracy falls within one harmonic order from the actual value due to the specified components being dominant in causing these resonances at low frequencies.

The higher order harmonic resonances (ω_3 and ω_4) accurately represent the simulated values due to the inclusion of all elements in calculating the resonant frequency. This validates the developed mathematical model, (4.3), that represents the reactance of the network in parallel with an RPP installation (jX_{POC}).

The effect of the impedance, as seen at the POC, needs to be quantified in terms of harmonic propagation from both the network-side's background harmonic voltage as well as injected harmonic currents from the installation-side. This necessitates that the impedance seen at the POC be compared to the impedances as seen from the harmonic sources.

4.5 The effect of resonance on harmonic propagation

Harmonic propagation of a harmonic source towards a specific node within a system is dependent on the various resistive and reactive elements in the system. Due to resonant conditions reactive elements cause high and low impedances that govern harmonic current flow. Resistive elements are relatively small compared to the reactive elements but are required to introduce damping of resonant conditions. The impedance that is experienced by each harmonic source is dependent on the position of the reactive components relative to the harmonic source.

The propagation towards the POC will be described from both the installation's and the network's harmonic sources' perspectives. Implementing superposition each of these sources' individual contributions can then be illustrated with transfer functions representing the propagation of harmonics toward the POC.

The parameter values summarized in Section 3.2.4 will be used to evaluate the transfer functions, regarding the developed simplified system model.

4.5.1 Propagation of installation harmonic current emission

By applying the harmonic current source as indicated in Fig. 4-4, the propagation towards the network can be determined. The propagation can be expressed in terms of harmonic current distortion, $\frac{\bar{I}'_h}{\bar{I}_h}$, and harmonic voltage distortion, $\frac{\bar{V}'_h}{\bar{I}_h}$, at the POC.

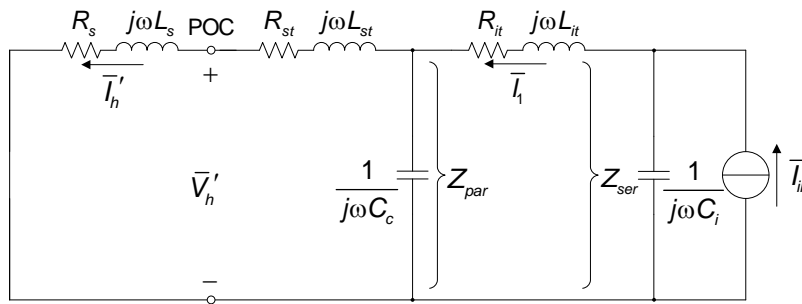


Fig. 4-4. Installation harmonic current source propagation

To determine the propagation of the harmonic current source (\bar{I}_h) the harmonic impedances Z_{par} and Z_{ser} are acquired for current division functions.

$$\begin{aligned} Z_{par} &= \frac{1}{\frac{1}{(R_s + R_{st}) + j\omega(L_s + L_{st})} + j\omega C_c} \\ &= \frac{(R_s + R_{st}) + j\omega(L_s + L_{st})}{1 + j\omega C_c(R_s + R_{st}) - \omega^2 C_c(L_s + L_{st})} \end{aligned} \quad (4.10)$$

$$\begin{aligned} Z_{ser} &= Z_{par} + j\omega L_{it} + R_{it} \\ &= \frac{(R_s + R_{st}) + j\omega(L_s + L_{st})}{1 + j\omega C_c(R_s + R_{st}) - \omega^2 C_c(L_s + L_{st})} + R_{it} + j\omega L_{it} \end{aligned} \quad (4.11)$$

Using the impedances calculated in (4.10) and (4.11), transfer functions representing the propagation of the installation harmonic current source towards the POC can be developed.

Harmonic current propagation

Using (4.11) and the inverter filter capacitor impedance \bar{I}_1 can be calculated as follows:

$$\begin{aligned}
 \bar{I}_1 &= \bar{I}_{ih} \cdot \frac{\frac{1}{j\omega C_i}}{\frac{1}{j\omega C_i} + Z_{ser}} \\
 &= \bar{I}_{ih} \cdot \frac{\frac{1}{j\omega C_i}}{\frac{1}{j\omega C_i} + \frac{(R_s + R_{st}) + j\omega(L_s + L_{st})}{1 + j\omega C_c(R_s + R_{st}) - \omega^2 C_c(L_s + L_{st})} + R_{it} + j\omega L_{it}} \\
 &= \bar{I}_{ih} \cdot \frac{1}{1 + j\omega C_i \cdot \left(\frac{(R_s + R_{st}) + j\omega(L_s + L_{st})}{1 + j\omega C_c(R_s + R_{st}) - \omega^2 C_c(L_s + L_{st})} + R_{it} + j\omega L_{it} \right)} \\
 &= \bar{I}_{ih} \cdot \frac{1 + j\omega C_c(R_s + R_{st}) - \omega^2 C_c(L_s + L_{st})}{1 + j\omega C_i \left[\begin{aligned} &(R_s + R_{st} + j\omega(L_s + L_{st})) \left(1 + \frac{C_c}{C_i} \right) + R_{it} + j\omega(L_{it} + C_c(R_s + R_{st})R_{it}) \\ &\dots - \omega^2 C_c(L_{it}(R_s + R_{st}) + (L_s + L_{st})(R_{it} + j\omega L_{it})) \end{aligned} \right]}
 \end{aligned} \tag{4.12}$$

The current that propagates towards the network can further be expressed as:

$$\begin{aligned}
 \bar{I}'_h &= \bar{I}_1 \cdot \frac{1}{\frac{1}{j\omega C_c} + (R_s + R_{st}) + j\omega(L_s + L_{st})} \\
 &= \bar{I}_1 \cdot \frac{1}{1 + j\omega C_c(R_s + R_{st}) - \omega^2 C_c(L_s + L_{st})} \\
 \frac{\bar{I}'_h}{\bar{I}_{ih}} &= \frac{1}{1 + j\omega C_i \left[\begin{aligned} &(R_s + R_{st} + j\omega(L_s + L_{st})) \left(1 + \frac{C_c}{C_i} \right) + R_{it} + j\omega(L_{it} + C_c(R_s + R_{st})R_{it}) \\ &\dots - \omega^2 C_c(L_{it}(R_s + R_{st}) + (L_s + L_{st})(R_{it} + j\omega L_{it})) \end{aligned} \right]}
 \end{aligned} \tag{4.13}$$

Implementing the established parameter values in the transfer function (4.13) results in Fig. 4-5.

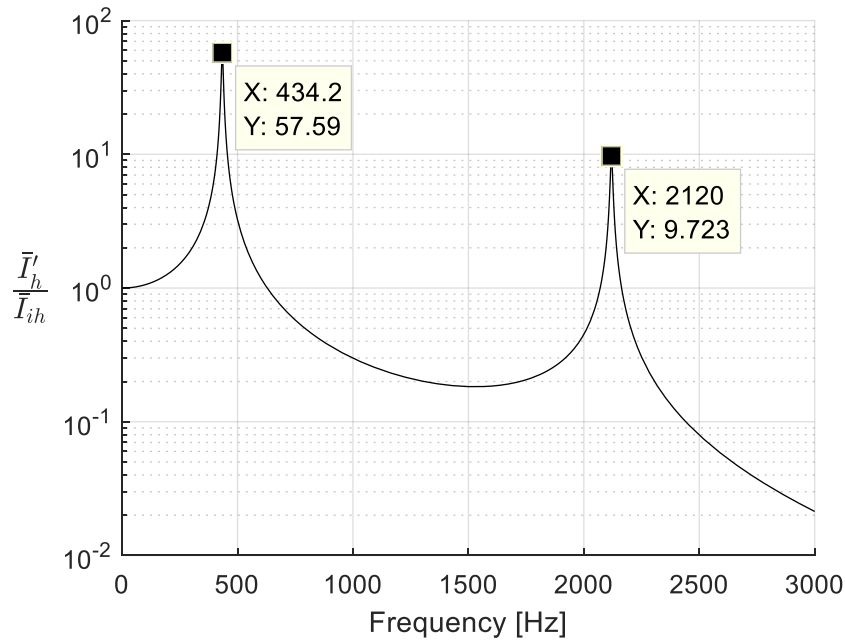


Fig. 4-5. Harmonic current distortion contribution from installation harmonic current emission

Harmonic voltage distortion propagation

The effective harmonic voltage distortion due to the installation harmonic current emission can be expressed as follows:

$$\bar{V}'_h = \bar{I}'_h \cdot (R_s + j\omega L_s)$$

$$\frac{\bar{V}'_h}{\bar{I}_{ih}} = \frac{R_s + j\omega L_s}{1 + j\omega C_i \left[\frac{(R_s + R_{st} + j\omega(L_s + L_{st})) \left(1 + \frac{C_c}{C_i} \right) + R_{it} + j\omega(L_{it} + C_c(R_s + R_{st}))R_{it}}{\dots - \omega^2 C_c (L_{it}(R_s + R_{st}) + (L_s + L_{st})(R_{it} + j\omega L_{it}))} \right]} \quad (4.14)$$

Implementing the established parameter values in the transfer function (4.14) results in Fig. 4-6.

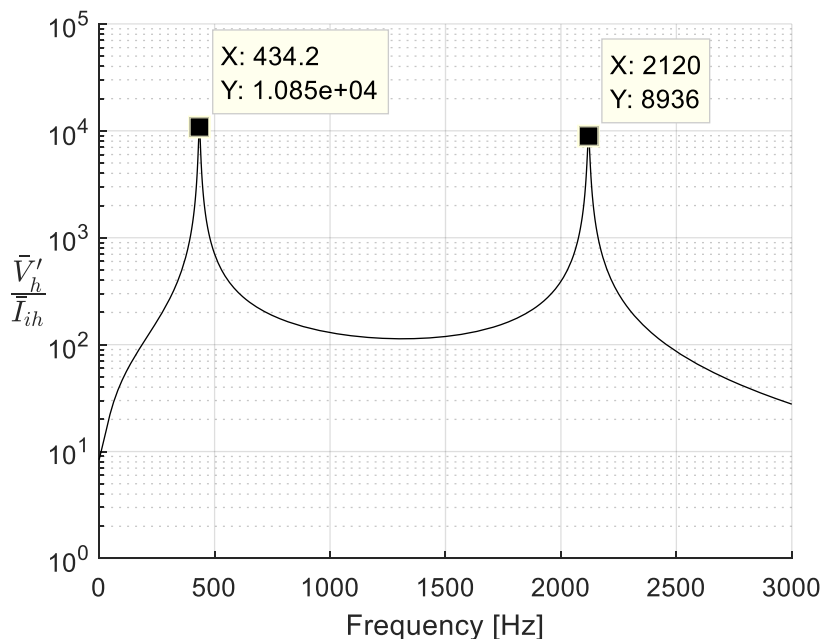


Fig. 4-6. Harmonic voltage distortion contribution from installation harmonic current emission

4.5.2 Propagation of background harmonic voltage distortion

By applying the background harmonic voltage distortion as indicated in Fig. 4-7, the propagation from the network towards the POC can be determined. The propagation can once again be expressed in terms of harmonic current emission, $\frac{\bar{I}_h''}{\bar{V}_{sh}}$, and harmonic voltage distortion, $\frac{\bar{V}_h''}{\bar{V}_{sh}}$, at the POC.

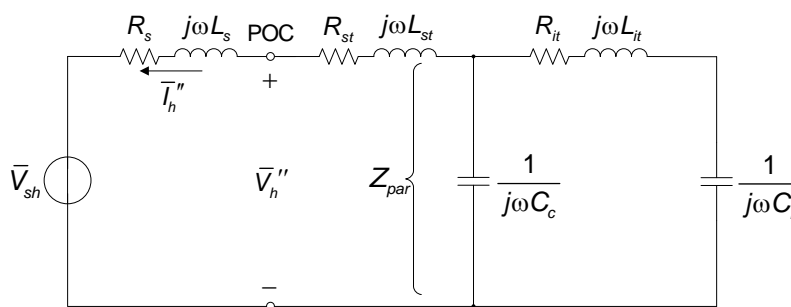


Fig. 4-7. Background harmonic voltage distortion propagation

To determine the propagation of the background harmonic voltage source (\bar{V}_{sh}) the harmonic impedance Z_{par} from Fig. 4-7 is required.

$$\begin{aligned}
Z_{par} &= \frac{1}{\frac{1}{R_{it} + j\omega L_{it}} + \frac{1}{j\omega C_i} + j\omega C_c} \\
&= \frac{1}{\frac{j\omega C_i}{j\omega C_i (R_{it} + j\omega L_{it}) + 1} + j\omega C_c} \\
&= \frac{j\omega C_i (R_{it} + j\omega L_{it}) + 1}{j\omega (C_c + C_i) - \omega^2 C_c C_i (R_{it} + j\omega L_{it})}
\end{aligned} \tag{4.15}$$

Using the impedance calculated in (4.15), transfer functions representing the propagation of the network harmonic voltage source towards the POC can be developed.

Harmonic current propagation

Using the impedance calculated in (4.15) the propagated harmonic current emission can be expressed as follows:

$$\begin{aligned}
\bar{I}_h'' &= \frac{\bar{V}_{sh}}{R_s + R_{st} + j\omega(L_s + L_{st}) + Z_{par}} \\
&= \frac{\bar{V}_{sh}}{R_s + R_{st} + j\omega(L_s + L_{st}) + \frac{j\omega C_i (R_{it} + j\omega L_{it}) + 1}{j\omega (C_c + C_i) - \omega^2 C_c C_i (R_{it} + j\omega L_{it})}} \\
\frac{\bar{I}_h''}{\bar{V}_{sh}} &= \frac{j\omega (C_c + C_i) - \omega^2 C_c C_i (R_{it} + j\omega L_{it})}{1 + j\omega C_i C_c \left[\left(\frac{1}{C_c} + \frac{1}{C_i} \right) [R_s + R_{st} + j\omega(L_s + L_{st})] \right. \\
&\quad \left. \dots + j\omega (R_{it} + j\omega L_{it}) (R_s + R_{st} + j\omega(L_s + L_{st})) \right]}
\end{aligned} \tag{4.16}$$

Implementing the established parameter values in the transfer function (4.16) results in Fig. 4-8.

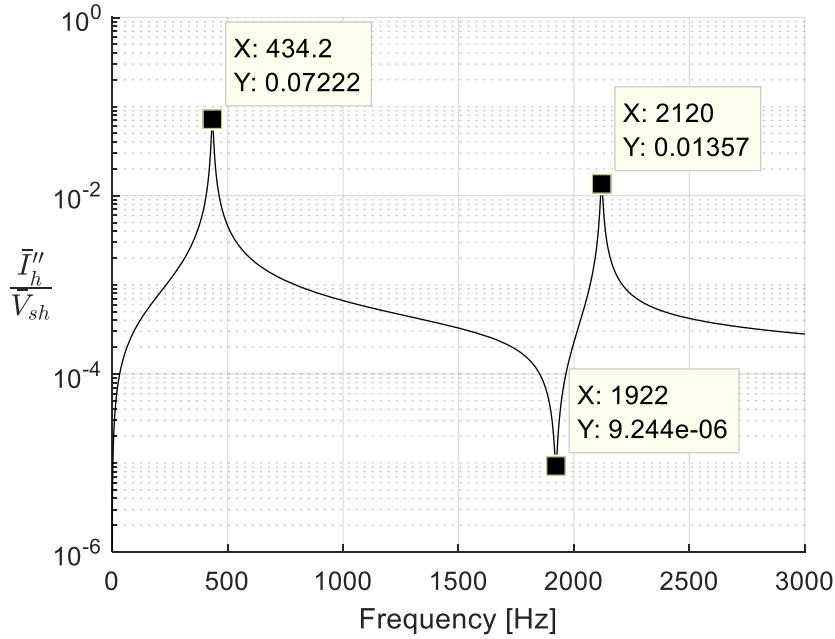


Fig. 4-8. Harmonic current emission contribution from background harmonic voltage distortion

Harmonic voltage distortion propagation

The effective harmonic voltage distortion that is contributed due to the background harmonic voltage distortion can be expressed as follows:

$$\begin{aligned}
 \bar{V}_h'' &= \bar{V}_{sh} \cdot \frac{R_{st} + j\omega L_{st} + Z_{par}}{R_s + R_{st} + j\omega(L_s + L_{st}) + Z_{par}} \\
 &= \bar{V}_{sh} \cdot \frac{R_{st} + j\omega L_{st} + \frac{j\omega C_i (R_{it} + j\omega L_{it}) + 1}{j\omega(C_c + C_i) - \omega^2 C_c C_i (R_{it} + j\omega L_{it})}}{R_s + R_{st} + j\omega(L_s + L_{st}) + \frac{j\omega C_i (R_{it} + j\omega L_{it}) + 1}{j\omega(C_c + C_i) - \omega^2 C_c C_i (R_{it} + j\omega L_{it})}} \\
 \frac{\bar{V}_h''}{\bar{V}_{sh}} &= \frac{j\omega C_i \left[\left(\frac{C_c}{C_i} + 1 \right) (R_{st} + j\omega L_{st}) \right. \\
 &\quad \left. \dots + j\omega [C_c (R_{it} + j\omega L_{it}) (R_{st} + j\omega L_{st}) + L_{it}] + R_{it} \right] + 1}{j\omega C_i \left[\left(\frac{C_c}{C_i} + 1 \right) (R_s + R_{st} + j\omega(L_s + L_{st})) \right. \\
 &\quad \left. \dots + j\omega [C_c (R_{it} + j\omega L_{it}) (R_s + R_{st} + j\omega(L_s + L_{st})) + L_{it}] + R_{it} \right] + 1} \quad (4.17)
 \end{aligned}$$

Implementing the established parameter values in the transfer function (4.17) results in Fig. 4-9.

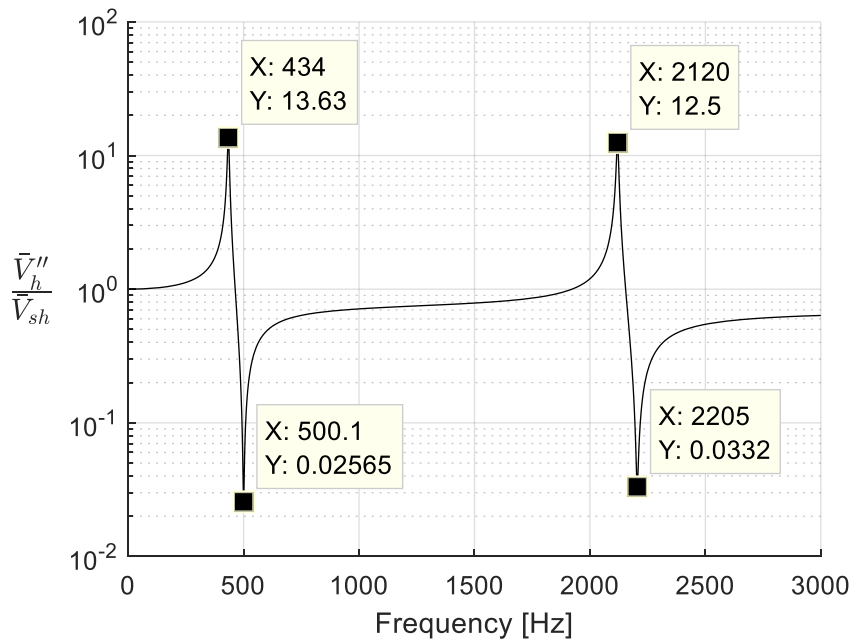


Fig. 4-9. Harmonic voltage distortion contribution from background harmonic voltage distortion

4.6 RPP installation resonance sensitivity analysis

The inverter filter capacitor and MV cabling capacitance resonates with the system's inductive components introducing resonant conditions. A resonance sensitivity analysis is performed on each of these elements to illustrate how it affects the resonant conditions.

4.6.1 Inverter filter capacitor sensitivity analysis

The equivalent inverter filter capacitance is expected to change as inverters connect and disconnect during their normal operational condition. The change in equivalent capacitance introduces changes in resonant frequencies and the impedance magnitudes at resonant conditions.

Changing the equivalent inverter filter capacitance from 0 to 371.9 nF illustrates the sensitivity of the system's impedance profile with respect to this variable. The sensitivity analysis is illustrated in Fig. 4-10.

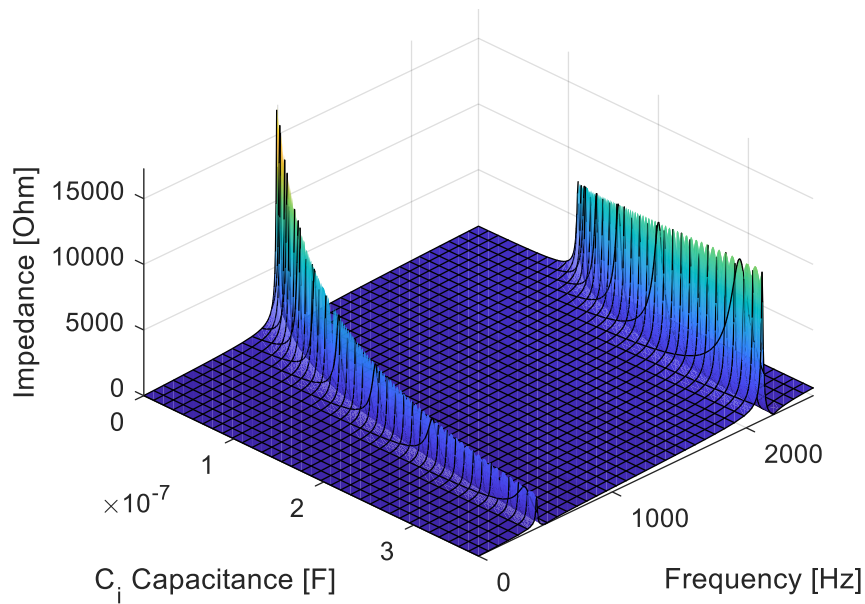


Fig. 4-10. System 3D resonance sensitivity mesh graph of the function $f(f, C_i)$

As seen in Fig. 4-10 the lower order harmonic impedance increases with a decrease in the inverter filter capacitance while the higher order resonant condition slightly shifts to a higher frequency. This is attributed towards the inverter filter capacitor's dominant participation towards the lower order resonant condition as previously discussed.

4.6.2 Medium voltage cabling sensitivity analysis

The equivalent MV cabling capacitance is a function of the length and amount of parallel cables and could therefore introduce significant variability when considering various lengths and branch configurations. The MV cabling capacitance is therefore set to vary between 0 and 250 nF to illustrate its contribution towards the resonant conditions, as illustrated in Fig. 4-11.

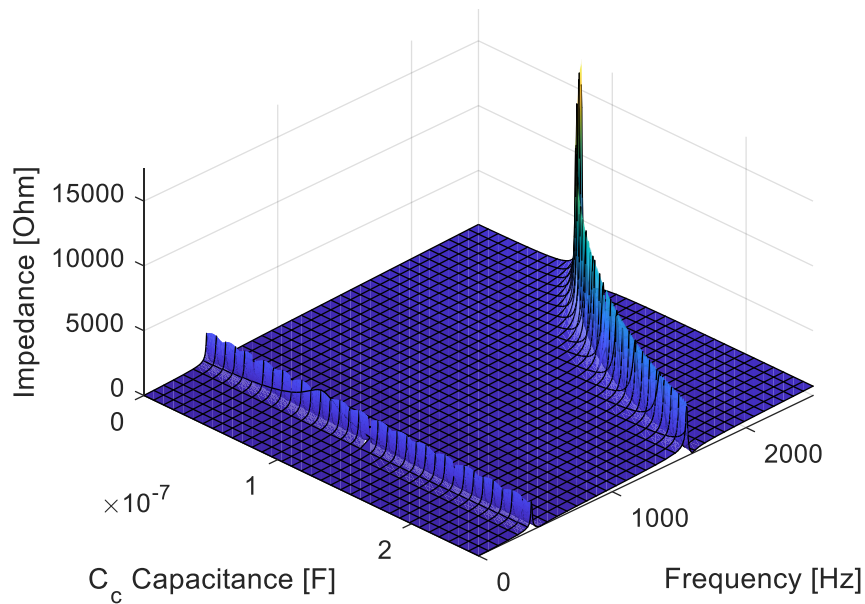


Fig. 4-11. System 3D resonance sensitivity mesh graph of the function $f(f, C_c)$

As seen in Fig. 4-11 the MV cabling capacitance has a very small effect on the lower order resonant condition both in its frequency and impedance magnitude. The cabling capacitance has a large effect on the higher order resonant condition shifting the frequency and impedance magnitude significantly.

The sensitivity analysis of both these capacitive elements illustrates that even though both capacitive elements participate towards the various resonant conditions, the extent of the participation varies for different resonant conditions.

4.7 Conclusion

Resonant conditions introduced due to the interaction of reactive elements within the RPP system were identified and approximations of the dominant interacting elements at lower frequencies were made. The developed impedance-based analytical equation, (4.3), as seen at the POC, along with the assessment loops illustrate which elements interact to causing resonant conditions.

The introduction of resonant conditions due to the presence of installation capacitive elements such as the inverter filter capacitor and the cabling capacitance were illustrated. Even though specific resonant conditions could be associated with these capacitive elements, as the inverter filter capacitor is dominantly associated with the lower order resonant condition, they have a joint influence on the creation of resonant conditions. It was found that the extent of the influence of each capacitive element still needs to be quantified.

The effect that resonant conditions have on harmonic propagation, both from the installation- and network-side, was illustrated. It was concluded that increased harmonic current and voltage contributions occur from both sides at characteristic parallel resonant conditions. The network-side contribution also illustrated decreased contributions at series resonant conditions.

The resonance sensitivity analysis that was performed on the RPP installation illustrated the participation that each of the two capacitive elements have towards the two resonant conditions. A way to quantify the resonant conditions would provide greater insight into the participation of different elements towards resonant conditions and will be further investigated in Chapter 5.

5 Resonant Mode Analysis of an RPP Installation Circuit

This chapter covers modal domain analysis of resonance on the developed RPP model from Chapter 3. The modal domain's simplification of the resonance analysis is discussed and methodically explained. The quantification of the contribution of elements, lacking from the impedance-based analytical approach, is addressed with greater focus on bus elements' participation towards resonant conditions. The propagation of harmonics is determined through transformed modal state variables.

5.1 Introduction

The introduction of resonant conditions caused by reactive elements in an RPP was discussed in Chapter 4. It was shown that resonant modes can be created, but that all elements have partial influence in creating these modes. Various current loops present in the creation of complex resonant conditions were identified. It becomes impossible to intuitively determine which elements have greater influence on specific resonant conditions in complex power systems with various capacitive elements.

RMA is a method that clarifies which elements take part in specific resonant modes. The participation factor is an indication of how system elements influence the system's natural modes and thus harmonic propagation through the system.

Modal analysis is typically used to identify the dynamic properties of a power system by decoupling its different natural resonant conditions. This decoupling produces orthogonal modes meaning that each mode is independent from the other modes. Modes identify modal resonances found in large power systems that contribute towards characteristic parallel nodal resonant conditions throughout the system. These resonant modes are implemented for QoS analysis and harmonic propagation assessment.

Applying modal analysis allows for the analysis of larger power systems, than have been investigated thus far using impedance-based analytical methods, through transformation of system parameters to the modal domain. Singular large characteristic resonances and the causes thereof can be identified in the modal domain to isolate and investigate problematic resonant conditions. These problematic

resonant conditions can be examined to identify dominant resonant components through their participation factors (PFs).

The proportional superimposition of the different modes in the modal domain results in the system's nodal frequency domain response producing the self-impedance. The frequency domain response investigated in Chapter 4 will be represented as the contribution of different resonant modes at the POC. These contributions will be mathematically described using the eigenvectors associated with the various resonant modes' impedances.

5.2 RMA of the simplified system

The process of transforming a system to independent modal state variables will be discussed in this section. RMA will be performed on the simplified model developed in Chapter 4 to illustrate the process of acquiring the modal impedance as well as the PFs of the various modes.

5.2.1 Establishing the admittance matrix

Consider the developed simplified system with a Norton equivalent grid connection and nodes as labelled in Fig. 5-1. This system is represented using admittances to simplify the system equations.

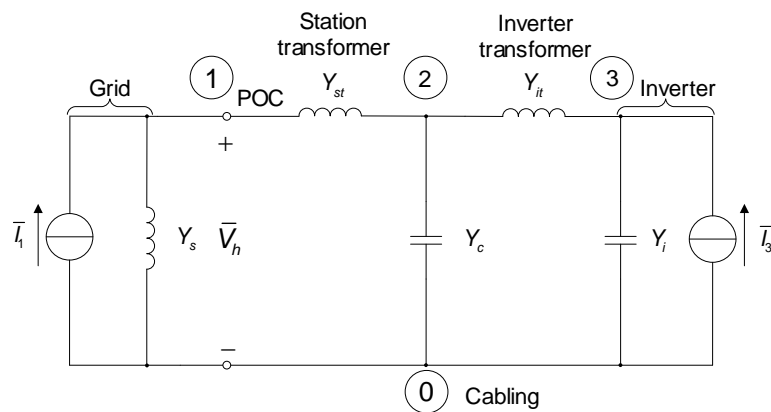


Fig. 5-1. Labelled simplified network and RPP installation model

The system's admittance matrix needed to be constructed as it represents the nodal state space of the power system at the point of equilibrium [34]. This is achieved through application of Kirchhoff's current law (KCL) on the modelled power system. Considering the simplified system in Fig. 5-1, this would result in the following equations implementing admittance parameters as follows:

$$\text{KCL} \Rightarrow \sum \bar{I}_{in} = \sum \bar{I}_{out}$$

$$1 \rightarrow \bar{I}_1 - \bar{V}_{10} \cdot \frac{1}{j\omega L_s} + (\bar{V}_{20} - \bar{V}_{10}) \cdot \frac{1}{j\omega L_{st}} = 0 \quad (5.1)$$

$$2 \rightarrow \bar{I}_2 + (\bar{V}_{10} - \bar{V}_{20}) \cdot \frac{1}{j\omega L_{st}} - \bar{V}_{20} \cdot j\omega C_c + (\bar{V}_{30} - \bar{V}_{20}) \cdot \frac{1}{j\omega L_{it}} = 0$$

$$3 \rightarrow \bar{I}_3 - \bar{V}_{30} \cdot j\omega C_i + (\bar{V}_{20} - \bar{V}_{30}) \cdot \frac{1}{j\omega L_{it}} = 0$$

Simplifying the results from (5.1) these equations can be written in the matrix form:

$$\mathbf{I} = \mathbf{YV}$$

$$\begin{bmatrix} \bar{I}_1 \\ \bar{I}_2 \\ \vdots \\ \bar{I}_n \end{bmatrix} = \begin{bmatrix} Y_{11} & Y_{12} & \dots & Y_{1n} \\ Y_{21} & Y_{22} & \dots & Y_{2n} \\ \vdots & \vdots & \ddots & \vdots \\ Y_{n1} & Y_{n2} & \dots & Y_{nn} \end{bmatrix} \begin{bmatrix} \bar{V}_1 \\ \bar{V}_2 \\ \vdots \\ \bar{V}_n \end{bmatrix} \quad (5.2)$$

where \mathbf{I} is the current vector, \mathbf{Y} is the admittance matrix and \mathbf{V} is the voltage vector. The admittance matrix (\mathbf{Y}) for (5.1) is defined in (5.3):

$$\begin{bmatrix} Y_{11} & Y_{12} & Y_{13} \\ Y_{21} & Y_{22} & Y_{23} \\ Y_{31} & Y_{32} & Y_{33} \end{bmatrix} = \begin{bmatrix} \frac{1}{j\omega L_s} + \frac{1}{j\omega L_{st}} & -\frac{1}{j\omega L_{st}} & 0 \\ -\frac{1}{j\omega L_{st}} & \frac{1}{j\omega L_{st}} + j\omega C_c + \frac{1}{j\omega L_{it}} & -\frac{1}{j\omega L_{it}} \\ 0 & -\frac{1}{j\omega L_{it}} & j\omega C_i + \frac{1}{j\omega L_{it}} \end{bmatrix} \quad (5.3)$$

For this section, the values that will be implemented for the admittance matrix, obtained from a real installation, are illustrated in Table XI.

Table XI: Simplified system parameter values

Parameter	Value
Network inductance (L_s)	69 mH
Station transformer inductance (L_{st})	159 mH
Cable capacitance (C_c)	112.5 nF
Inverter transformer inductance (L_{it})	79.38 mH
Inverter filter capacitance (C_i)	371.9 nF

5.2.2 Eigenvalue calculation

The system's admittance matrix from (5.3) is used to calculate the current vector (\mathbf{I}) through matrix multiplication with the voltage vector (\mathbf{V}). This operation can also be performed using eigenvalues and eigenvectors decoupling the system's admittance matrix. This transforms higher order state equations into n decoupled first-order differential equations [34].

The system's eigenvalues can be determined solving the following characteristic equation associated with each eigenvalue:

$$\begin{aligned} \mathbf{Y}\Phi &= \lambda\Phi \\ \mathbf{Y}\Phi - \lambda\mathbf{I}\Phi &= \mathbf{0} \\ (\mathbf{Y} - \lambda\mathbf{I})\Phi &= \mathbf{0} \end{aligned} \tag{5.4}$$

where \mathbf{Y} is the symmetrical $n \times n$ admittance matrix, λ is the scalar eigenvalue, \mathbf{I} is the identity matrix and Φ is a nonzero eigenvector. For (5.4) to have non-trivial solutions, for the nonzero eigenvector Φ , the characteristic equation is expressed as follows to acquire the eigenvalues of \mathbf{Y} :

$$|\mathbf{Y} - \lambda\mathbf{I}| = 0 \tag{5.5}$$

where the roots of the characteristic equation (determinant of $\mathbf{Y} - \lambda\mathbf{I}$) provide the eigenvalues. Applying (5.5) to the power system admittance matrix (\mathbf{Y}) results in the eigenvalues that represent the decoupled admittance modes.

Calculating the eigenvalue characteristic equation expressed by (5.5) for the system admittance matrix in (5.3) results in the following symbolic equation:

$$\begin{aligned}
|\mathbf{Y} - \lambda \mathbf{I}| &= \left| \begin{bmatrix} Y_{11} & Y_{12} & 0 \\ Y_{12} & Y_{22} & Y_{23} \\ 0 & Y_{23} & Y_{33} \end{bmatrix} - \begin{bmatrix} \lambda & 0 & 0 \\ 0 & \lambda & 0 \\ 0 & 0 & \lambda \end{bmatrix} \right| = 0 \\
&= \left| \begin{bmatrix} Y_{11} - \lambda & Y_{12} & 0 \\ Y_{12} & Y_{22} - \lambda & Y_{23} \\ 0 & Y_{23} & Y_{33} - \lambda \end{bmatrix} \right| \\
&= (Y_{11} - \lambda) \left[(Y_{22} - \lambda)(Y_{33} - \lambda) - Y_{23}^2 \right] - Y_{12} \left[Y_{12} (Y_{33} - \lambda) \right] \\
0 &= -\lambda^3 + \lambda^2 (Y_{11} + Y_{22} + Y_{33}) - \lambda \left[Y_{11} (Y_{22} + Y_{33}) - (Y_{23}^2 + Y_{12}^2) + Y_{22} Y_{33} \right] \\
&\quad \dots + Y_{11} Y_{22} Y_{33} - (Y_{11} Y_{23}^2 + Y_{12}^2 Y_{33})
\end{aligned} \tag{5.6}$$

The roots of this 3rd degree polynomial equation provide the eigenvalues of the system. It is, however, cumbersome to solve the 3rd degree polynomial equation, therefore a recursive method for solving the roots is implemented. The recursive method implemented in this case is the Newton-Raphson method defined as:

$$x_{n+1} = x_n - \frac{df(x_n)}{dx_n} \tag{5.7}$$

where x_{n+1} is the next approximation value for λ , x_n is the current approximation value for λ and $f(x_n)$ is the characteristic function as stated in (5.6). Since the equation that is being solved is a 3rd degree polynomial the Newton-Raphson will be implemented to obtain three roots that represent the system's three eigenvalues.

5.2.3 Eigenvalue decomposition

Having obtained the eigenvalues for the system in Fig. 5-1 the system's admittance matrix can be represented as follows:

$$\mathbf{Y} = \mathbf{\Psi} \mathbf{\Lambda} \mathbf{\Phi} \tag{5.8}$$

with the transformed eigensystem equation defined as:

$$\mathbf{I} = \mathbf{\Psi} \mathbf{\Lambda} \mathbf{\Phi} \mathbf{V} \tag{5.9}$$

where $\mathbf{\Psi}$ is the left eigenvector, $\mathbf{\Lambda}$ is the diagonalized eigenvalue matrix and $\mathbf{\Phi}$ is the right eigenvector. Since the inverse of the left eigenvector is equal to the right eigenvector, $\mathbf{\Psi}^{-1} = \mathbf{\Psi}^T = \mathbf{\Phi}$, [35] and the inverse of the diagonal eigenvalue matrix produces the modal impedance matrix this leads to (5.9) being expressed as:

$$\begin{aligned}
\mathbf{V} &= \Psi \Lambda^{-1} \Phi \mathbf{I} \\
\begin{bmatrix} \bar{V}_1 \\ \bar{V}_2 \\ \vdots \\ \bar{V}_n \end{bmatrix} &= \begin{bmatrix} \psi_{11} & \psi_{12} & \cdots & \psi_{1n} \\ \psi_{21} & \psi_{22} & \cdots & \psi_{2n} \\ \vdots & \vdots & \ddots & \vdots \\ \psi_{n1} & \psi_{n2} & \cdots & \psi_{nn} \end{bmatrix} \begin{bmatrix} \lambda_1^{-1} & 0 & \cdots & 0 \\ 0 & \lambda_2^{-1} & \cdots & 0 \\ \vdots & \vdots & \ddots & \vdots \\ 0 & 0 & \cdots & \lambda_n^{-1} \end{bmatrix} \begin{bmatrix} \phi_{11} & \phi_{12} & \cdots & \phi_{1n} \\ \phi_{21} & \phi_{22} & \cdots & \phi_{2n} \\ \vdots & \vdots & \ddots & \vdots \\ \phi_{n1} & \phi_{n2} & \cdots & \phi_{nn} \end{bmatrix} \begin{bmatrix} \bar{I}_1 \\ \bar{I}_2 \\ \vdots \\ \bar{I}_n \end{bmatrix} \\
\Phi \mathbf{V} &= \Lambda^{-1} \Phi \mathbf{I} \\
\mathbf{U} &= \Lambda^{-1} \mathbf{J} \\
\begin{bmatrix} \bar{U}_1 \\ \bar{U}_2 \\ \vdots \\ \bar{U}_n \end{bmatrix} &= \begin{bmatrix} \lambda_1^{-1} & 0 & \cdots & 0 \\ 0 & \lambda_2^{-1} & \cdots & 0 \\ \vdots & \vdots & \ddots & \vdots \\ 0 & 0 & \cdots & \lambda_n^{-1} \end{bmatrix} \begin{bmatrix} \bar{J}_1 \\ \bar{J}_2 \\ \vdots \\ \bar{J}_n \end{bmatrix}
\end{aligned} \tag{5.10}$$

Expressing the system equation as observed in the modal domain introduces two new parameters. These parameters are the modal voltage vector ($\mathbf{U} = \Phi \mathbf{V}$) and the modal current vector ($\mathbf{J} = \Phi \mathbf{I}$) which are the linear projections of the voltage and current vectors, respectively, in the direction of the eigenvector.

To obtain the right eigenvector, also known as the eigenvector (Φ), (5.4) needs to be solved for each of the system's eigenvalues. The eigenvectors of the system are not unique, but the ratio of the eigenvectors is unique as it provides the direction of the eigenvector. The eigenvectors are normalised to normalise the results.

5.2.4 Participation factor

The concept of a PF is introduced to identify the sensitivity that a node has towards a resonant mode. Nodes with larger PFs experience greater risk for potential resonance leading to increased voltage distortions from current injections throughout the system.

The PF is defined as the combination of the observability and excitability characteristics of a node in a power system. Where the left and right eigenvectors represent the observability and excitability, respectively. This is mathematically described as:

$$PF_{bm} = \psi_{bm} \phi_{mb} \tag{5.11}$$

where PF_{bm} is the participation of bus b to mode m , ψ_{bm} is the observability/left eigenvector value for bus b to mode m and ϕ_{mb} is the excitability/right eigenvector value for mode m to bus b .

5.2.5 Results

Implementing the eigenvalue decomposition from the previous section on the system admittance ultimately results in the inverse diagonalized eigenvalue matrix which represents the modal impedance of the system.

Since it is tedious to perform eigenvalue decomposition on a frequency dependant admittance matrix a MATLAB script, included in Appendix C, is implemented to plot the modal impedance using the above methodology. This resulted in the modal impedances as illustrated in Fig. 5-2 for the system represented in Fig. 5-1.

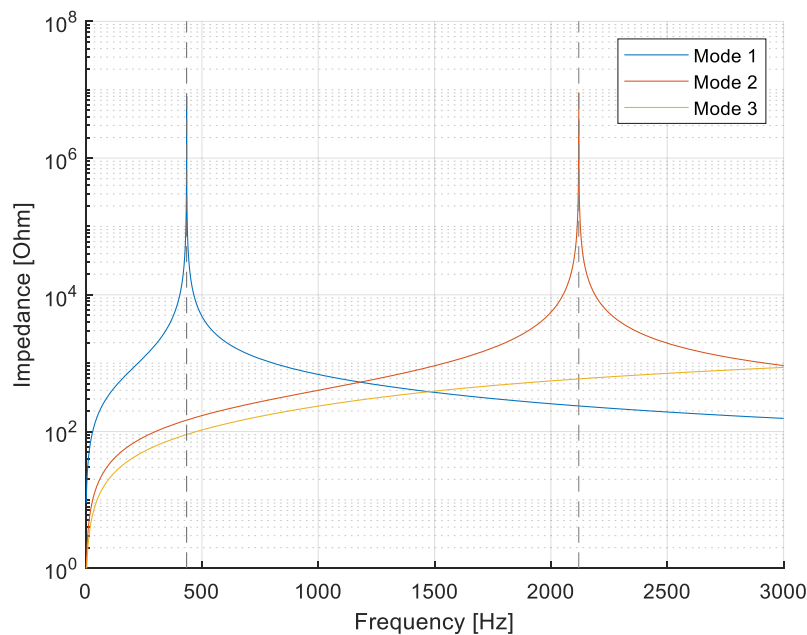


Fig. 5-2. Modal impedance of simplified system

Two of the three modes experience resonances which coincide with the resonances that were identified at the POC from Chapter 4 and are illustrated in Table XII. The number of resonant conditions typically coincide with the number of capacitors in the system [35].

Table XII: Modal resonant frequencies of simplified system model

Mode	Resonant frequency
Mode 1	434.2 Hz
Mode 2	2120 Hz
Mode 3	None

The critical impedance is defined as the maximum impedance as illustrated in Fig. 5-2. The mode segmented critical mode impedance is also illustrated in Fig. 5-3.

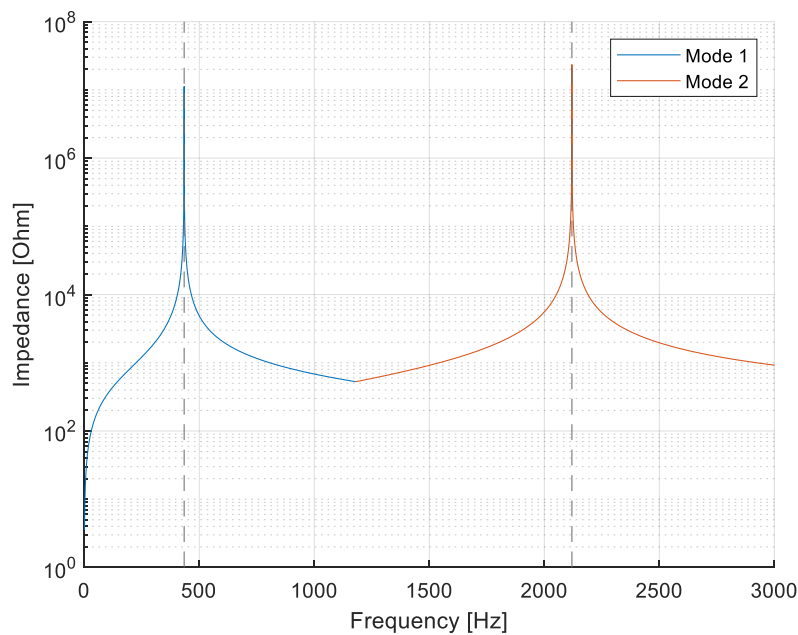


Fig. 5-3. Critical mode impedance of simplified system

From the system's critical mode impedance, the relevant resonant frequencies can be identified and analysed to determine which nodes are most susceptible to these specific resonant conditions. Resistor values are implemented, with values as illustrated in Table XIII, to introduce damping when calculating the PFs at the resonant frequencies. The PFs are calculated using (5.11) and the results are illustrated in Table XIV.

Table XIII: Simplified system resistive damping values

Parameter	Value
Network resistance (R_s)	8.39 Ω
Station transformer resistance (R_{st})	2.177 Ω
Inverter transformer resistance (R_{it})	5.01 Ω

Table XIV: PFs of simplified system resonant modes at each node for peak resonant frequencies

PF _{mode} \ Node	1	2	3
PF ₁	0.0336	0.3657	0.6008
PF ₂	0.0799	0.8716	0.0486

From Table XIV it is identified that the cabling node (node 2) and the inverter-side components (node 3), particularly the inverter filter capacitor, have a dominant contribution towards the lower order harmonic resonance. The mode 2 resonance has a dominant contribution from the cabling node (node 2) suggesting that the cabling capacitance introduces the higher order harmonic resonance, as it is smaller than the inverter filter capacitor therefore dominating the current assessment impedance loop at the higher frequency.

A node's self-impedance is the composition of the modal impedances and the PFs that the node has toward each mode. The modal impedance composition of the self-impedance can mathematically be described as follows:

$$\begin{aligned}
Z_{kk} &= \frac{\bar{V}_k}{I_k} \\
&= \Psi_k \Lambda^{-1} \Phi_k \\
&= [\psi_{k1} \quad \psi_{k2} \quad \cdots \quad \psi_{kn}] \begin{bmatrix} \lambda_1^{-1} & 0 & \cdots & 0 \\ 0 & \lambda_2^{-1} & \cdots & 0 \\ \vdots & \vdots & \ddots & \vdots \\ 0 & 0 & \cdots & \lambda_n^{-1} \end{bmatrix} \begin{bmatrix} \phi_{1k} \\ \phi_{2k} \\ \vdots \\ \phi_{nk} \end{bmatrix} \\
&= \lambda_1^{-1} \psi_{k1} \phi_{1k} + \lambda_2^{-1} \psi_{k2} \phi_{2k} + \cdots + \lambda_n^{-1} \psi_{kn} \phi_{nk} \\
&= \sum_{i=1}^n \lambda_i^{-1} \psi_{ki} \phi_{ik}
\end{aligned} \tag{5.12}$$

where k is the bus number and n the mode number. Applying this to the modal impedances, obtained from implementing the resistive damping from Table XIII, results in the nodal self-impedances as illustrated in Fig. 5-4.

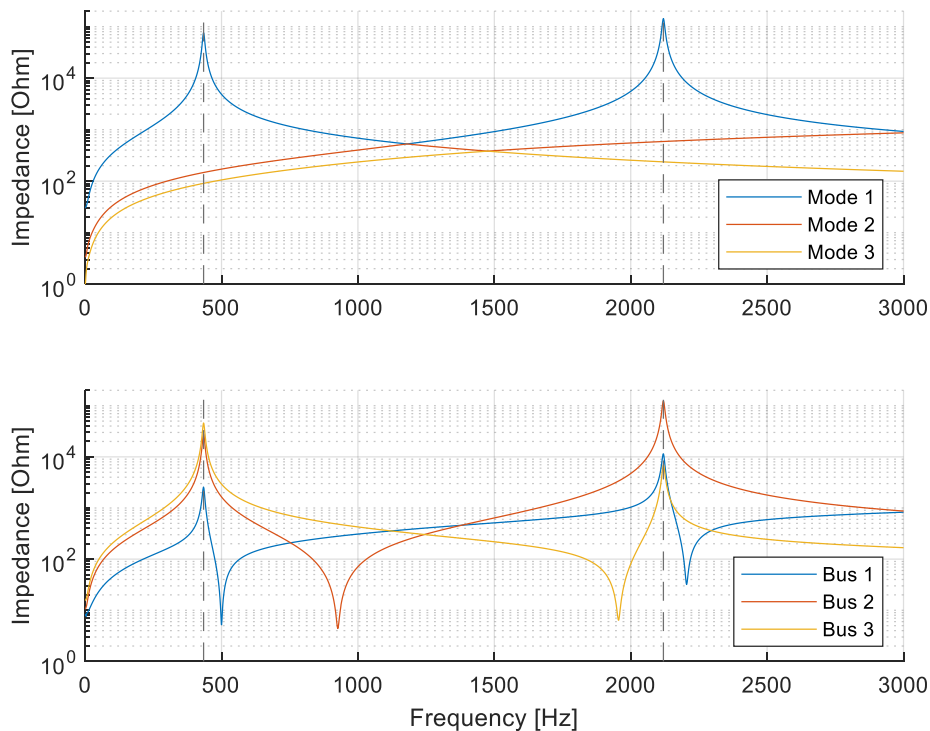


Fig. 5-4. Driving point impedance (bottom) decomposition from modal impedances (top) of simplified network model

The self-impedances seen in Fig. 5-4 corresponds with the Simulink model's impedances, as measured at the same nodes. This indicates that the modal decomposition produced accurate results.

5.3 Harmonic propagation as affected by modes

As done using network reduction in Chapter 4 the harmonic propagation of the installation's harmonic current emission and the background harmonic voltage distortion will be described.

The propagation can be described in terms of the harmonic voltage distortion \bar{V}_l , at node l , for a specific harmonic current injection \bar{I}_k , at node k , representing the transfer impedance between these two nodes as follows:

$$\begin{aligned}
Z_{lk} &= \frac{\bar{V}_l}{\bar{I}_k} \\
&= \Psi_l \Lambda^{-1} \Phi_k \\
&= [\psi_{l1} \quad \psi_{l2} \quad \cdots \quad \psi_{ln}] \begin{bmatrix} \lambda_1^{-1} & 0 & \cdots & 0 \\ 0 & \lambda_2^{-1} & \cdots & 0 \\ \vdots & \vdots & \ddots & \vdots \\ 0 & 0 & \cdots & \lambda_n^{-1} \end{bmatrix} \begin{bmatrix} \phi_{1k} \\ \phi_{2k} \\ \vdots \\ \phi_{nk} \end{bmatrix} \\
&= \lambda_1^{-1} \psi_{l1} \phi_{1k} + \lambda_2^{-1} \psi_{l2} \phi_{2k} + \cdots + \lambda_n^{-1} \psi_{ln} \phi_{nk} \\
&= \sum_{i=1}^n \lambda_i^{-1} \psi_{li} \phi_{ik}
\end{aligned} \tag{5.13}$$

Where node current \bar{I}_k and node voltage \bar{V}_l can be calculated from the column eigenvectors Ψ_l and Φ_k of the transformation matrix. The $\psi_{li} \phi_{ik}$ term in (5.13) is defined as the cross-participation factor as it indicates the participation between node l and k for the modal impedance λ_i^{-1} .

Describing the harmonic propagation in terms of the harmonic current distortion requires that the equivalent harmonic voltage distortion be converted with respect to the appropriate impedance as seen at the POC. This leads to the transfer functions being described as follows for the installation's (5.14) and the network's (5.15) harmonic current contribution respectively.

$$\begin{aligned}
A_i &= \frac{\bar{V}_l / Z_{sn}}{\bar{I}_k} \\
&= \frac{Z_{lk}}{Z_{sn}}
\end{aligned} \tag{5.14}$$

$$\begin{aligned}
A_i &= \frac{\bar{V}_l / Z_{si}}{\bar{I}_k} \\
&= \frac{Z_{lk}}{Z_{si}}
\end{aligned} \tag{5.15}$$

Where Z_{sn} and Z_{si} are the system network and installation harmonic impedances as seen from the POC, respectively, and Z_{lk} is the transfer impedance between the injection node (k) and the POC node (l).

5.3.1 Propagation of installation's current emission

Considering the same simplified system configuration from Fig. 5-1, the voltage distortion contribution due to the installation's harmonic current emission can be described using (5.13). Applying this function, the transfer impedance is calculated as illustrated in Fig. 5-5.

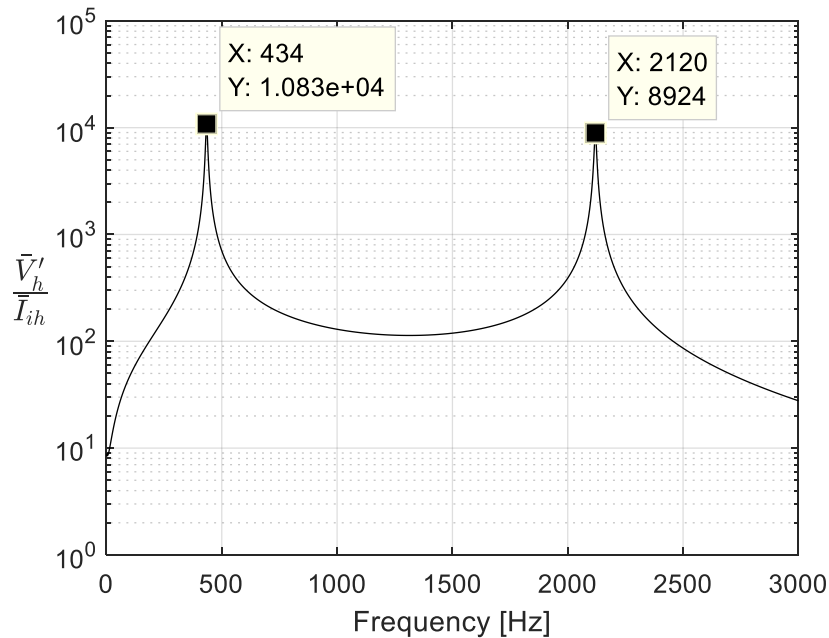


Fig. 5-5. Harmonic voltage distortion contribution from installation harmonic current emission using modal analysis

The results from Fig. 5-5 correlate with the results obtained in Chapter 4, Fig. 4-6.

Describing the harmonic current contribution requires that the harmonic voltage distortion \bar{V}'_h be converted to the harmonic current equivalent \bar{I}'_h dividing by the network impedance (Z_{sn}), as seen at the POC. This results in Fig. 5-6 for the simplified system.

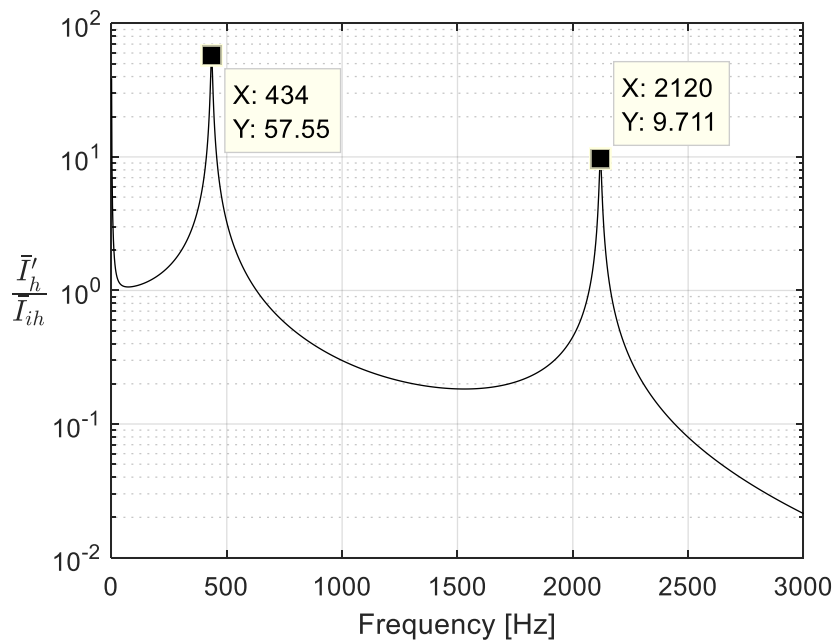


Fig. 5-6. Simplified system harmonic current emission contribution from installation harmonic current emission using modal analysis

The current contribution results also correlate with the numerical results obtained in Chapter 4, Fig. 4-5.

5.3.2 Propagation of background harmonic voltage

Describing the network's harmonic voltage contribution can be done using (5.13). Due to the system configuration the current is injected directly into the observation node, leading to a transfer function representing the self-impedance. The results are illustrated in Fig. 5-7.

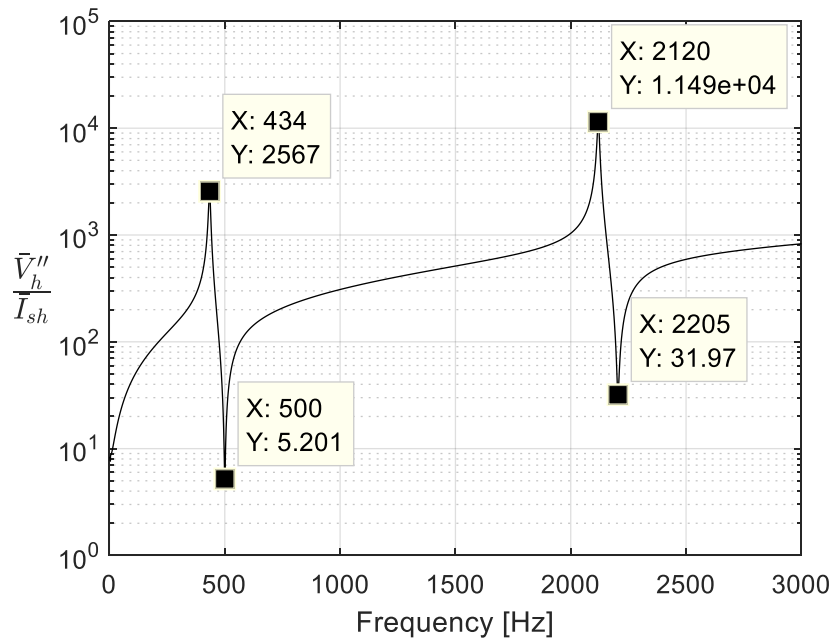


Fig. 5-7. Simplified system harmonic voltage distortion contribution from background harmonic current emission using modal analysis

The harmonic current transfer at the POC towards the installation is subsequently determined using (5.15). This result is illustrated in Fig. 5-8.

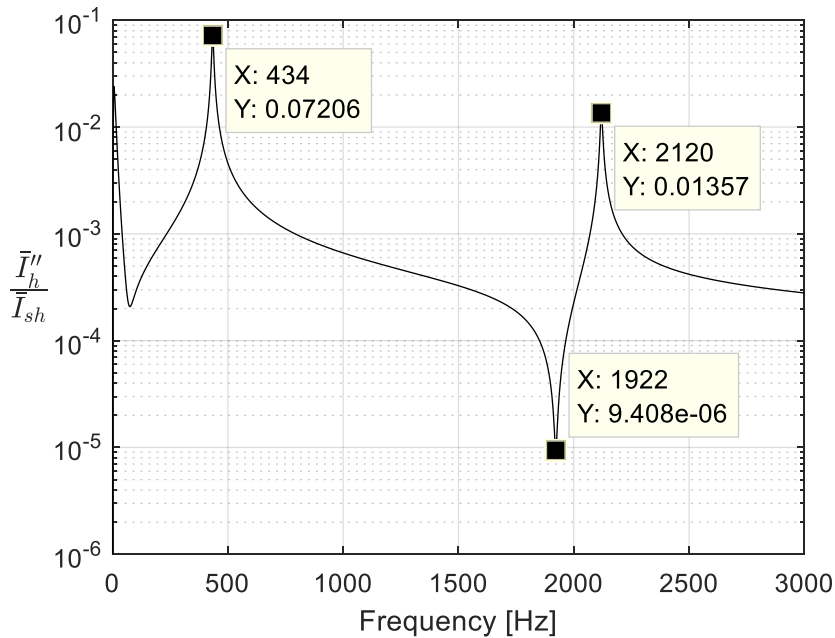


Fig. 5-8. Simplified system harmonic current distortion contribution from network harmonic current emission using modal analysis

Since the network is modelled using the Norton equivalent the harmonic voltage source is converted to an equivalent harmonic current source. The transfer functions that were developed in Chapter 5, however, considered the transfer of the network harmonics as a harmonic voltage source.

The results obtained for the harmonic current source representation can be converted by dividing with the network's Norton impedance to obtain the harmonic voltage transfer function equivalent. This is done as follows to obtain the harmonic voltage contribution:

$$\begin{aligned} \frac{\bar{V}_h''}{\bar{V}_{sh}} &= \frac{V_I}{I_k \cdot Z_{sn}} \\ &= \frac{Z_{lk}}{Z_{sn}} \end{aligned} \quad (5.16)$$

Applying (5.16) with the current transfer function calculated for the network's contribution results in Fig. 5-9.

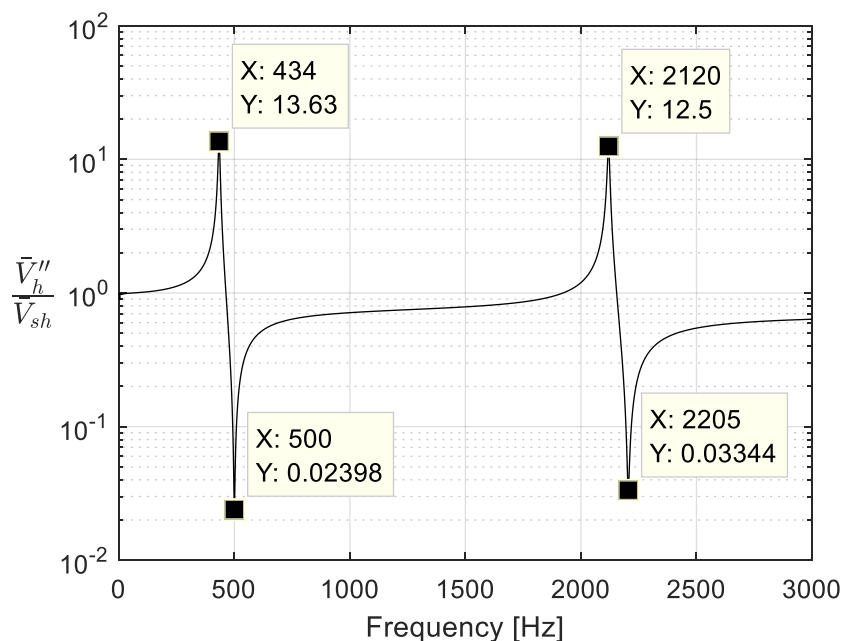


Fig. 5-9. Simplified system harmonic voltage distortion contribution from background harmonic voltage distortion using modal analysis

Comparing Fig. 5-9 with the results obtained in Chapter 4, Fig. 4-9 the harmonic voltage propagations are identical.

Transforming (5.15) to obtain the harmonic current contribution from a harmonic voltage source is done as follows:

$$A_i = \frac{\bar{V}_i / Z_{si}}{\bar{I}_k \cdot Z_{sn}} \quad (5.17)$$

$$= \frac{Z_{ik}}{Z_{si} \cdot Z_{sn}}$$

Applying (5.17) to the current transfer function calculated for the network's contribution results in Fig. 5-10.

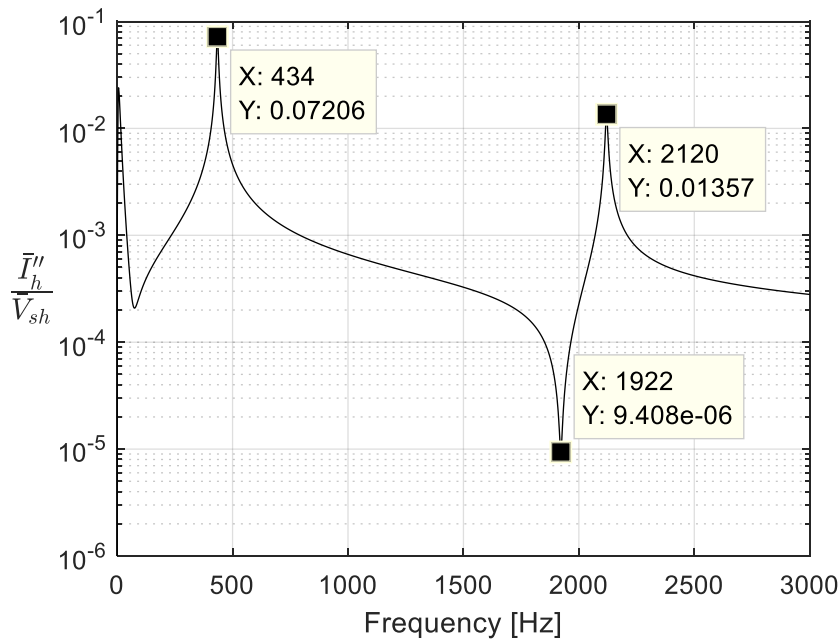


Fig. 5-10. Simplified system harmonic current emission contribution from background harmonic voltage distortion using modal analysis

The results from Fig. 5-10 correlate well with the results obtained in Chapter 4, Fig. 4-8. The discrepancy at the lower frequencies (<100 Hz) are due to the Norton equivalent network circuit causing harmonic current to dissipate both in the network as well as the installation, where the network has a significantly smaller impedance at the lower frequencies. In Chapter 4 the harmonic current was considered to only propagate towards the installation.

5.4 Conclusion

In this chapter the RMA process was discussed and applied. The results that were obtained from the RMA produced the same self-impedances as those analytically calculated in Chapter 4. This indicates that RMA can be used to identify resonant conditions without requiring the construction of tedious impedance-based analytical models.

The PFs calculated for each mode allowed for the identification of dominant nodes responsible for resonant conditions. The PFs provide a metric of how injected harmonics influence a system's harmonic state variables. Larger participation factors at buses throughout the network indicate their susceptibility to harmonic current injections causing greater harmonic voltage distortion at those buses. The controllability of buses with greater participation factors also indicate where harmonic current can best be mitigated.

The concept of a cross-participation factor was introduced and implemented to calculate the transfer impedance between nodes from the system modal impedances. The cross-participation factor is used in conjunction with the resonant modal impedances to determine the significance of the resonant condition on the propagation of harmonics between those nodes. This allows for the quantification of the effect of characteristic parallel resonance on propagation between nodes.

6 Application of RMA on Complex PowerFactory Model using Python

This chapter covers the development and RMA of a representative, real network and RPP model, developed in DigSILENT PowerFactory. The PowerFactory Python API is implemented to automatically construct a complex power system admittance matrix. The methodology for constructing the system admittance matrix is discussed. RMA is applied to the constructed admittance matrix and the relevant resonant modes' participation factors are evaluated. Propagation is analysed through transfer impedances calculated using cross-participation factors.

6.1 Introduction

As discussed in Chapter 5, RMA provides a simplified evaluation methodology for the identification of problematic components that cause additional resonant conditions and have an influence on harmonic propagation. This is achieved through determining buses' participation factors towards critical resonant mode conditions in the modal domain. This assessment methodology has been applied to a simplified circuit in Chapter 5 and will be further investigated in this chapter to make provision for analysing a larger network through automatically constructing the admittance matrix of a complex power systems.

The simplified RPP circuit, developed in Chapter 3, connected to a representative real network model will be considered in this chapter. The system's dynamic topological deviations are neglected as they fall outside of the scope of this thesis. The network model, that has been developed in PowerFactory, expands upon the complexity of the network, introducing additional resonant conditions which have previously been disregarded.

Due to PowerFactory containing detailed models of network equipment the model will be analysed using Python instead of MATLAB. The built in Python application programming interface (API) from PowerFactory will be utilized to analyse the network. The analyses include the construction of the model's positive sequence admittance matrix, as this feature is not available in PowerFactory, and the application, evaluation, and visualisation of RMA in Python.

6.2 System model development

A largely integrated network consists of various possible network states making state selection for harmonic assessment onerous. It is also difficult to determine accurate steady-state parameters for a given network model, even with resources such as [25] and [42]. The IEC 61000-3-6 states that when an accurate network model, as connected to the POC, cannot be provided a generic system covering different operating condition can be implemented to characterise the network [25].

6.2.1 Network reduction methodology

This chapter investigates a large integrated network model developed in PowerFactory, illustrated in Appendix A. The network impedance characteristics were determined through frequency sweeps executed at the RPP's POC, while the installation was disconnected. Six network conditions were identified, considering possible network variations around the connected RPP, and are illustrated in Fig. 6-1. These network conditions provided a basis from which a reduced network configuration could be constructed.

A reduced network configuration would allow for a more precise evaluation of the interaction between the RPP and selected network elements. Evaluating the various network conditions, illustrated in Fig. 6-1, identified 3 to 5 prominent resonant conditions throughout the investigated frequency spectrum. The objective was to reduce the number of network elements whilst maintaining 5 distinctive resonant conditions in the various frequency regions (intervals of 500 Hz).

The network was therefore altered, considering the various network conditions from Fig. 6-1, to a reduced network configuration which only included elements between the Bacchus, Boskloof and Laingsburg buses of the 132 kV network. The HV network connected to the Bacchus busbar was also linearised to simplify the modelling. This reduced the number of participating buses to 14, as illustrated in Appendix A.5, which produced sensible results when performing RMA.

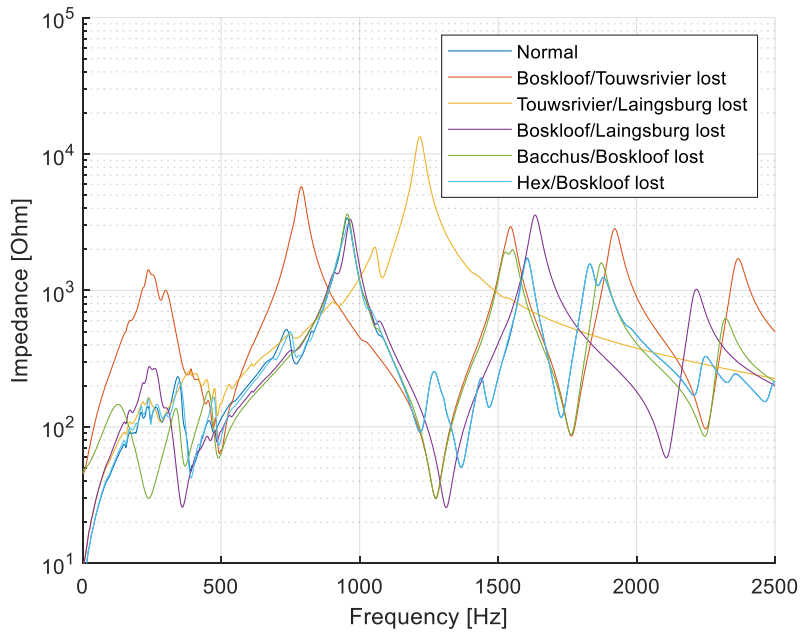


Fig. 6-1. Various network conditions' frequency sweep impedances

6.2.2 Network model

Having identified the reduced network configuration the network elements that are incorporated into the reduced network needed to be identified. Firstly, the source impedance needed to be established. The Bacchus busbar is connected to the 400 kV network which includes many generating units connected throughout the network system, as seen in Appendix A.1. The Bacchus self-impedance was acquired from a frequency sweep and is illustrated in Fig. 6-2.

The phase angle observed in Fig. 6-2 revealed that the connected network is predominantly inductive with various capacitive components causing partial resonant conditions. Partial resonance is defined as a resonant condition where impedance does not undergo a large phase angle change (± 180 degrees) as it changes from inductive to capacitive and vice versa. The network was therefore modelled as a voltage source with a series RL input impedance, as previously simplified in Chapter 3, illustrated in Fig. 6-3.

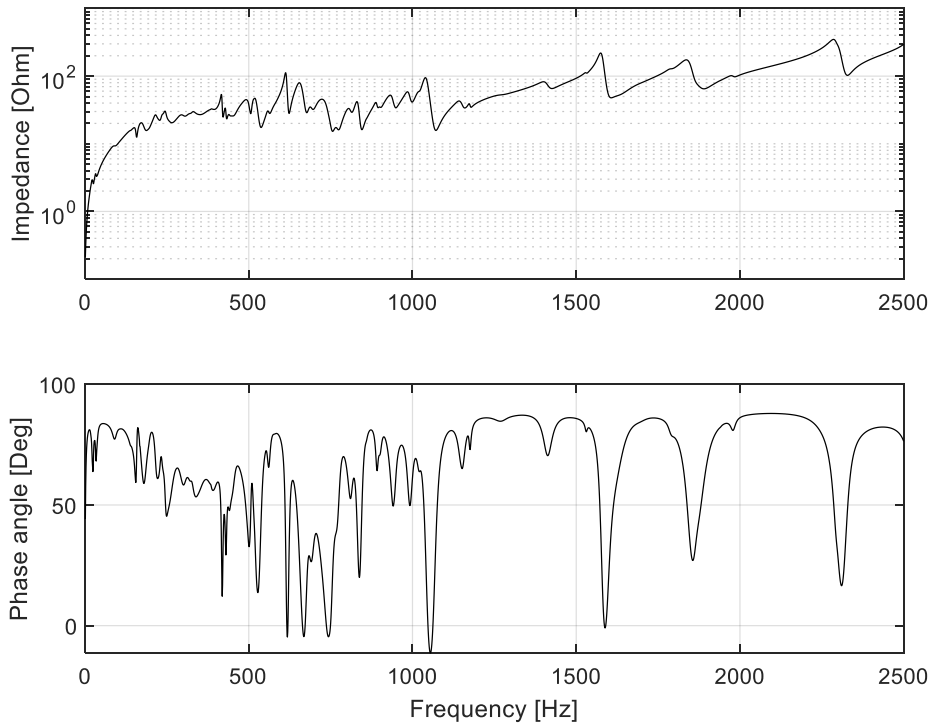


Fig. 6-2. Bacchus self-impedance (top) and phase angle (bottom)

The value for the source input impedance had to be determined and two approaches were considered. The first approach implemented the 50 Hz component to extrapolate the network impedance, as is done when network data is not available. The second method applied a simple linear regression model (LRM), using the method of least squares, on the network impedance data that was acquired in Fig. 6-2.

The 50 Hz component interpolation model was calculated as follows:

$$\begin{aligned}
 R_s &= 0.556 \, \Omega \\
 X_s &= 4.931 \, \Omega \\
 \Rightarrow L_s &= \frac{4.931}{100\pi} = 15.696 \, \text{mH}
 \end{aligned}
 \tag{6.1}$$

From (6.1) a simplistic network impedance could be constructed. The line of best fit, however, was calculable with the LRM which is represented in the following form [43]:

$$y = \beta_0 + \beta_1 x + \varepsilon \tag{6.2}$$

where x is the regressor variable, y is the response variable, β_0 and β_1 are the regression coefficients, representing the intercept and slope respectively, and ε is the random error component.

The considered LRM method of least squares minimizes the difference between the observed y-values and the regressed function y-values, optimizing the selected impedance for the specific network dataset. For the method of least squares the following criteria needed to be met:

$$S(\beta_0, \beta_1) = \sum_{i=1}^n (y_i - \beta_0 - \beta_1 x_i)^2 \quad (6.3)$$

for which the partial derivatives needed to be satisfied:

$$\left. \frac{\partial S}{\partial \beta_0} \right|_{\hat{\beta}_0, \hat{\beta}_1} = -2 \sum_{i=1}^n (y_i - \hat{\beta}_0 - \hat{\beta}_1 x_i) = 0 \quad (6.4)$$

and

$$\left. \frac{\partial S}{\partial \beta_1} \right|_{\hat{\beta}_0, \hat{\beta}_1} = -2 \sum_{i=1}^n (y_i - \hat{\beta}_0 - \hat{\beta}_1 x_i) x_i = 0 \quad (6.5)$$

where $\hat{\beta}_0$ and $\hat{\beta}_1$ are the least squares estimators for the fitted linear regression model, y_i is the observed value and n is the number of datapoints in the dataset. The fitted LRM is represented by the following function:

$$\hat{y} = \hat{\beta}_0 + \hat{\beta}_1 x \quad (6.6)$$

where \hat{y} is the estimated result. Rewriting (6.4) and (6.5) results in the following equations, also known as the least-squares normal equations:

$$n\hat{\beta}_0 + \hat{\beta}_1 \sum_{i=1}^n x_i = \sum_{i=1}^n y_i \quad (6.7)$$

$$\hat{\beta}_0 \sum_{i=1}^n x_i + \hat{\beta}_1 \sum_{i=1}^n x_i^2 = \sum_{i=1}^n y_i x_i \quad (6.8)$$

Simplifying (6.7) results in the solution of $\hat{\beta}_0$ as follows:

$$\begin{aligned} n\hat{\beta}_0 + \hat{\beta}_1 \sum_{i=1}^n x_i &= \sum_{i=1}^n y_i \\ \hat{\beta}_0 + \hat{\beta}_1 \frac{\sum_{i=1}^n x_i}{n} &= \frac{\sum_{i=1}^n y_i}{n} \\ \hat{\beta}_0 &= \bar{y} - \hat{\beta}_1 \bar{x} \end{aligned} \quad (6.9)$$

where \bar{x} and \bar{y} are the mean values of x and y respectively, as calculated in (6.9). The solution for $\hat{\beta}_1$ is derived by substituting (6.9) in (6.8) as follows:

$$\begin{aligned}
 \hat{\beta}_0 \sum_{i=1}^n x_i + \hat{\beta}_1 \sum_{i=1}^n x_i^2 &= \sum_{i=1}^n y_i x_i \\
 (\bar{y} - \hat{\beta}_1 \bar{x}) \sum_{i=1}^n x_i + \hat{\beta}_1 \sum_{i=1}^n x_i^2 &= \sum_{i=1}^n y_i x_i \\
 \hat{\beta}_1 \left(\sum_{i=1}^n x_i^2 - \sum_{i=1}^n x_i \bar{x} \right) &= \sum_{i=1}^n y_i x_i - \sum_{i=1}^n x_i \bar{y} \\
 \hat{\beta}_1 &= \frac{\sum_{i=1}^n y_i x_i - \sum_{i=1}^n x_i \bar{y}}{\sum_{i=1}^n x_i^2 - \sum_{i=1}^n x_i \bar{x}} \\
 \hat{\beta}_1 &= \frac{\sum_{i=1}^n y_i x_i - \frac{\left(\sum_{i=1}^n y_i \right) \left(\sum_{i=1}^n x_i \right)}{n}}{\sum_{i=1}^n x_i^2 - \frac{\left(\sum_{i=1}^n x_i \right)^2}{n}} \\
 \hat{\beta}_1 &= \frac{\sum_{i=1}^n y_i (x_i - \bar{x})}{\sum_{i=1}^n (x_i - \bar{x})^2} \tag{6.10}
 \end{aligned}$$

Applying the described LRM method of least squares on the impedance dataset with a training set up to 2000 Hz results in the following fitted LRM:

$$\hat{y} = 4.4108 + 0.04956 \hat{x} \tag{6.11}$$

(6.11) can be interpreted as having impedance values as follows:

$$\begin{aligned}
 R_s &= 4.4108 \, \Omega \\
 X_s &= 0.04956 \times 50 = 2.478 \, \Omega \\
 \Rightarrow L_s &= \frac{2.478}{100\pi} = 7.888 \, \text{mH}
 \end{aligned} \tag{6.12}$$

Both linear network representations (6.1) and (6.12) could be implemented in Fig. 6-3. Due to both linear network representations being significantly different a comparative analysis needed to be conducted, as done in Section 6.2.3.

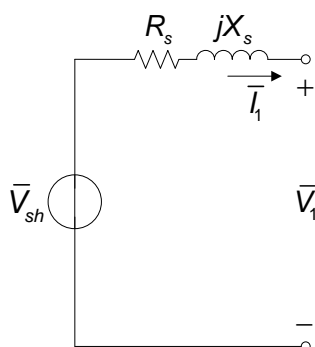


Fig. 6-3. Network AC voltage source representation with source impedance

The rest of the network consists of various short length (shorter than 80 km) aluminium conductor steel reinforced (ACSR) overhead lines (OHLs). Two types of ACSRs were present in the reduced network and are characterised by the codename which reflects the number of aluminium (Al) and steel strands as well as the wire diameter (D) in mm [44].

The OHLs were represented as equivalent PI circuits and have properties as listed in Table XV. The long line effect was acknowledged but ignored to reduce the complexity of modelling the network using distributed parameters which would result in multiple capacitors operating on a single OHL.

Table XV: Reduced network OHL properties

Connected buses	ACSR Type Codename (Al/Steel/D)	Length
Bacchus–Boskloof	Bear (30/7/3.35)	25.6 km
Boskloof–Touwsrivier	Wolf (30/7/2.59)	50 km
Boskloof–Quarry	Wolf (30/7/2.59)	75 km
Touwsrivier–Quarry	Wolf (30/7/2.59)	35 km
Quarry–Pietermeintjies	Wolf (30/7/2.59)	22.49 km
Pietermeintjies–Bantam	Wolf (30/7/2.59)	11.41 km
Bantam–Whitehill	Wolf (30/7/2.59)	11.17 km
Whitehill–Baviaan	Wolf (30/7/2.59)	9.96 km
Baviaan–Laingsburg	Wolf (30/7/2.59)	13.81 km

Lastly, a load needed to be added to the network to resemble the loading effect which introduces additional damping. The load was selected as 150Ω to provide a $\pm 20\%$ resistive loading effect, based on the Bacchus network's 500 MVA rating. The load has a power rating as follows:

$$\begin{aligned}
 P_{load} &= \frac{V^2}{R_{load}} \\
 &= \frac{(132 \cdot 10^3)^2}{150} \\
 &= 116.16 \text{ MW}
 \end{aligned} \tag{6.13}$$

6.2.3 Validation

The network impedance, as seen from the Bacchus 132 kV busbar, could be represented using the 50Hz component interpolated model or through the simple LRM. A discrepancy throughout the frequency spectrum was, therefore, expected. These two models were, compared against the network impedance, as seen in Fig. 6-2, and resulted in Fig. 6-4.

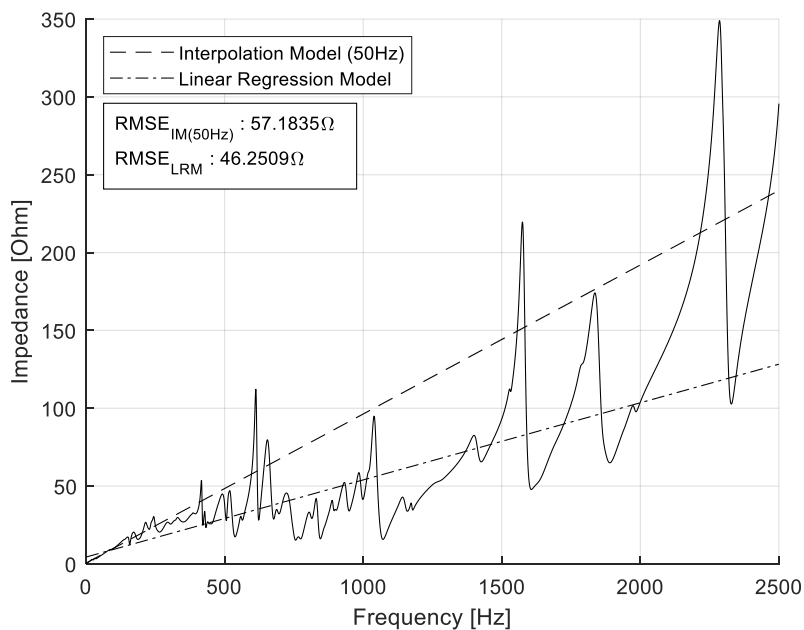


Fig. 6-4. Bacchus network impedance and interpolated model impedance

The adequacy of each of the models was subsequently calculated through the root mean squared error (RMSE) as follows:

$$\begin{aligned}
 RMSE_{IM(50Hz)} &= \sqrt{\frac{\sum_{i=1}^n (y_i - \hat{y}_i)^2}{n}} \\
 &= 57.1835 \Omega
 \end{aligned} \tag{6.14}$$

and

$$RMSE_{LRM} = \sqrt{\frac{\sum_{i=1}^n (y_i - \hat{y}_i)^2}{n}} \quad (6.15)$$

$$= 46.2509 \Omega$$

where y_i is the observed network impedance value at point i , \hat{y}_i is the respective model's impedance value at point i and N is the number of datapoints.

Evaluating the RMSE values led to the conclusion that the error that is introduced by the linearization of the network impedance is negligible, with respect to the expected impedance on the 132 kV network. The LRM was selected as it had a lower RMSE.

Another metric on which the LRM is evaluated is the coefficient of determination (R^2). The R^2 value ranges between 0 and 1 for LRMs and serves as a metric that explains the amount of variation introduced by the regressor variable [43]. R^2 was calculated as follows:

$$R^2 = \frac{\sum_{i=1}^n (\bar{y} - \hat{y}_i)^2}{\sum_{i=1}^n (y_i - \bar{y})^2} \quad (6.16)$$

$$= 0.6911$$

The R^2 value is strong and identified that the network model is indeed dominantly inductive. The linear model can therefore be represented using an inductive reactive component, providing a positive slope, with a resistive component to introduce damping. The R^2 also illustrated that the LRM has a significant fit to the observed impedance data and could be implemented with the reduced network model.

Lastly, the POC bus impedance, with the simplified installation connected, was evaluated from both the reduced and detailed network's perspectives. The evaluation aimed to provide insight into the discrepancies and similarities between the two models. The comparison can be seen in Fig. 6-5.

Evaluating the compared impedances led to the conclusion that the same number of total resonant conditions are present in each model's impedance. The resonant frequencies, however, differ slightly and the detailed network model has a significant number of partial resonant conditions.

It was concluded that quite a few elements that participate in each total resonant condition are present in the reduced model. Therefore, RMA could adequately be applied to the reduced model, identifying the participating components.

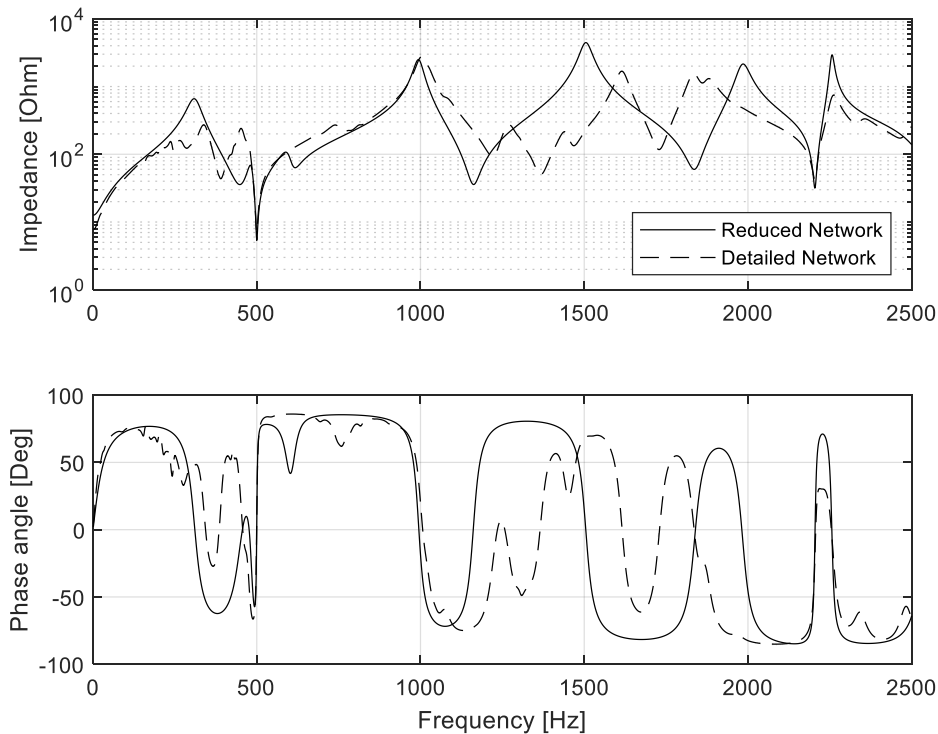


Fig. 6-5. Impedance (top) and phase angle (bottom) comparison of reduced and detailed network models

This concluded the evaluation of the developed reduced network model. The system admittance matrix subsequently had to be developed for the reduced network model to perform RMA.

6.2.4 Admittance matrix construction methodology

An alternative method for establishing the bus admittance matrix will be considered for this section to remove the need for KCL equations.

The elemental values for the admittance matrix are expressed in accordance with the following conditions [45]:

$$\begin{aligned} \text{diagonal elements: } Y_{kk} &= \text{sum of admittances connected} \\ &\text{to bus } k \\ &(k = 1, 2, \dots, N) \end{aligned} \quad (6.17)$$

$$\begin{aligned} \text{off-diagonal elements: } Y_{kn} &= -(\text{sum of admittances connected} \\ &\text{between buses } k \text{ and } n) \quad (k \neq n) \end{aligned} \quad (6.18)$$

the Y_{kk} elements represent the self-admittance and the Y_{kn} represents the mutual admittance.

6.3 PowerFactory Python API

PowerFactory provides a vast number of network components that are used to develop intricate network models used for various applications. The simplified models that were implemented, however, required a significant amount of computation to develop. Implementing a graphical user interface (GUI) power system oriented suite, such as PowerFactory, for developing large network models would therefore be more efficient.

Since the focus of this thesis is on RMA the system positive sequence admittance matrix is required to obtain the system's various resonant modes. PowerFactory, however, does not provide the capability to export the system's admittance matrix. PowerFactory's Python API was implemented to develop the admittance matrix, as discussed in the following sections.

An overview of the process implemented with Python code to construct the admittance matrix and the various analyses results is illustrated in the flow diagram in Fig. 6-6.

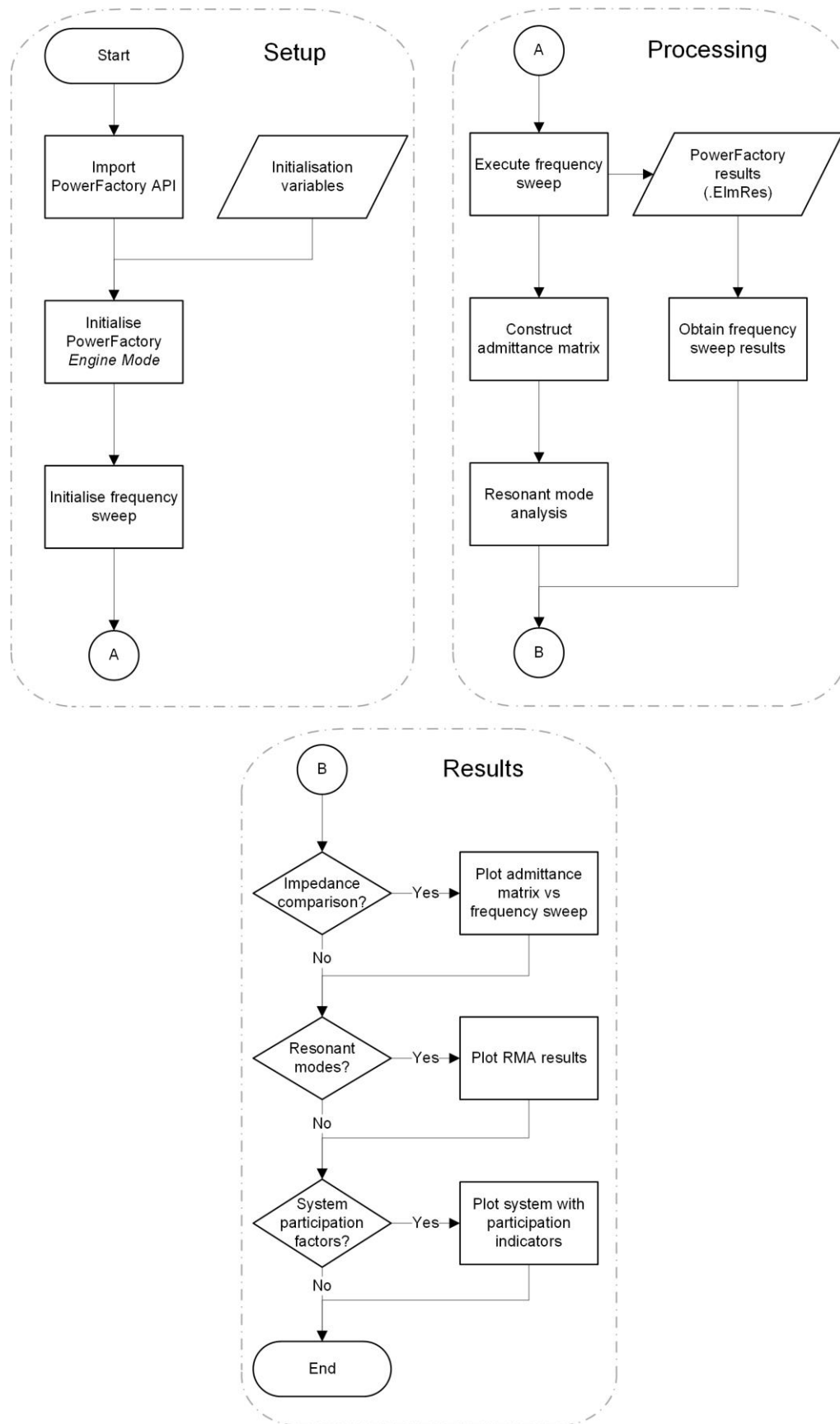


Fig. 6-6. Flow diagram of Python code process overview

6.3.1 Setup

For this thesis PowerFactory was run in *engine mode* which provides all the functionality of PowerFactory without requiring GUI interactions. This enabled the control of PowerFactory functions from an external Python IDE. The interactions between the Python script, developed in the external Python IDE, and PowerFactory are managed by PowerFactory's Python API [46], as illustrated in Fig. 6-7.

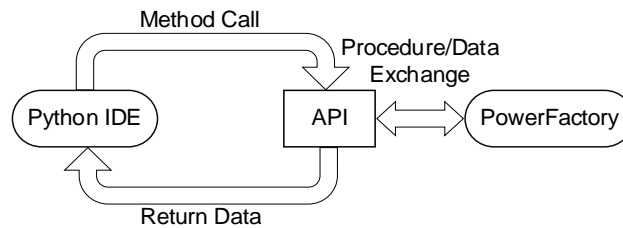


Fig. 6-7. Python IDE interaction with PowerFactory API

The API is accessed through the built-in Python dynamic module which is included with PowerFactory. The Python module, “*powerfactory.pyd*”, located in the PowerFactory installation directory, needed to be imported. This was done using the code included in Appendix B.

All the PowerFactory API functionality could be utilized after importing the module. The module contains various defined PowerFactory functions and objects for the PowerFactory components located in the project file.

A PowerFactory simulation object that could be used to access the various simulation functionalities needed to be defined. A class was defined to develop the required user-defined functions. The implementation of a class also allowed for the initialisation of PowerFactory, in *engine mode*, implementing the special `__init__()` method that executes upon instantiating a PowerFactorySim object.

When the PowerFactory simulation class is initiated the project and study case information needs to be passed as arguments. These parameters are used to activate the specified project and study case, as labelled in PowerFactory. The study case holds the management information used to determine the operational scenario and perform calculation to reproduce results [47].

The last part of the setup phase involved preparing the frequency sweep function to obtain model specific bus impedance frequency sweeps. This will later be compared against the impedance acquired from the admittance matrix.

6.3.2 Processing

Using the API to perform simulation based tasks such as performing frequency sweeps and acquiring line impedance parameters to construct the admittance matrix are part of the processing section. The defined class also contains a function that is used to execute the RMA.

The frequency sweep results that were stored in the PowerFactory results object (*Freq.Sweep.ElmRes*) needed to be accessed to obtain a bus frequency sweep impedance. The results object stores the results in a structure, represented in Table XVI.

Table XVI: PowerFactory frequency sweep results object structure

Column number							
	-1	0	1	...	n	n+1	...
Row Number	Harmonic Order	<i>BB Bacchus.ElmTerm</i>		...	BB Laignsburg.ElmTerm		...
		m:Z	m:phiz	...	m:Z	m:phiz	...
0	0.02	4.285	0.609	...	18.588	2.262	
1	0.04	4.286	1.219		18.632	4.517	
⋮			⋮			⋮	⋮

The code listed in Appendix B illustrates how the column number was determined for the corresponding variable name and result type. To obtain the *BB Bacchus* impedance magnitude column **0** would be stored and returned with a function call. The returned magnitude array could then be compared against the constructed admittance matrix to verify the results.

The admittance matrix was constructed using element-wise admittance analysis. All the connected network elements were evaluated, and the admittance matrix values calculated as described in Section 6.2.4. The process is illustrated in Fig. 6-8.

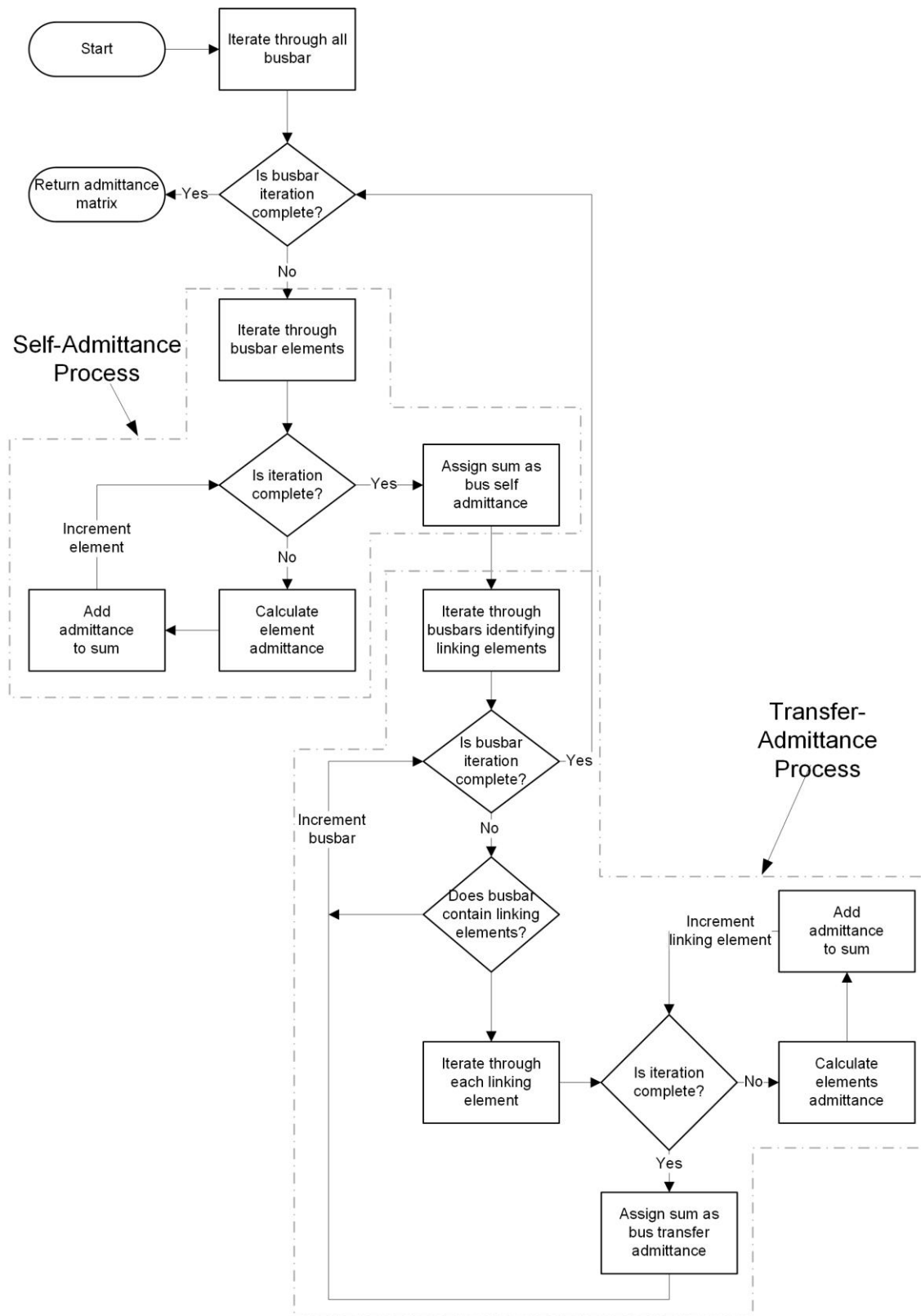


Fig. 6-8. Construction of the admittance matrix flow diagram

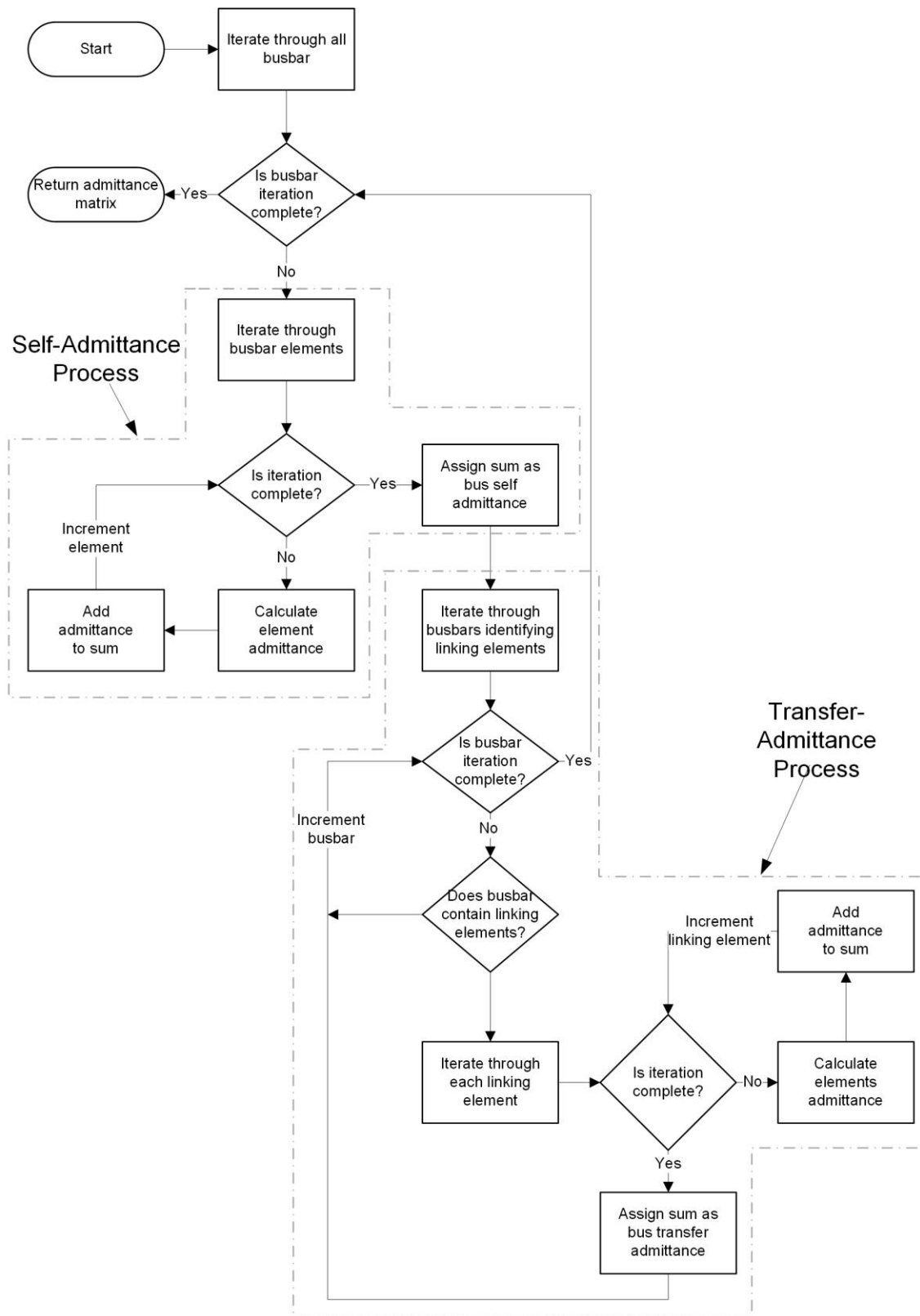


Fig. 6-9. Admittance matrix construction process flow diagram

The code that was developed for the admittance matrix construction is included in Appendix B. After the admittance matrix was constructed RMA could be applied to the constructed matrix. Applying the same principles as in Section 5.2.3 the modal domain impedance was calculated. The process of applying RMA to the constructed admittance matrix is illustrated in Fig. 6-10.

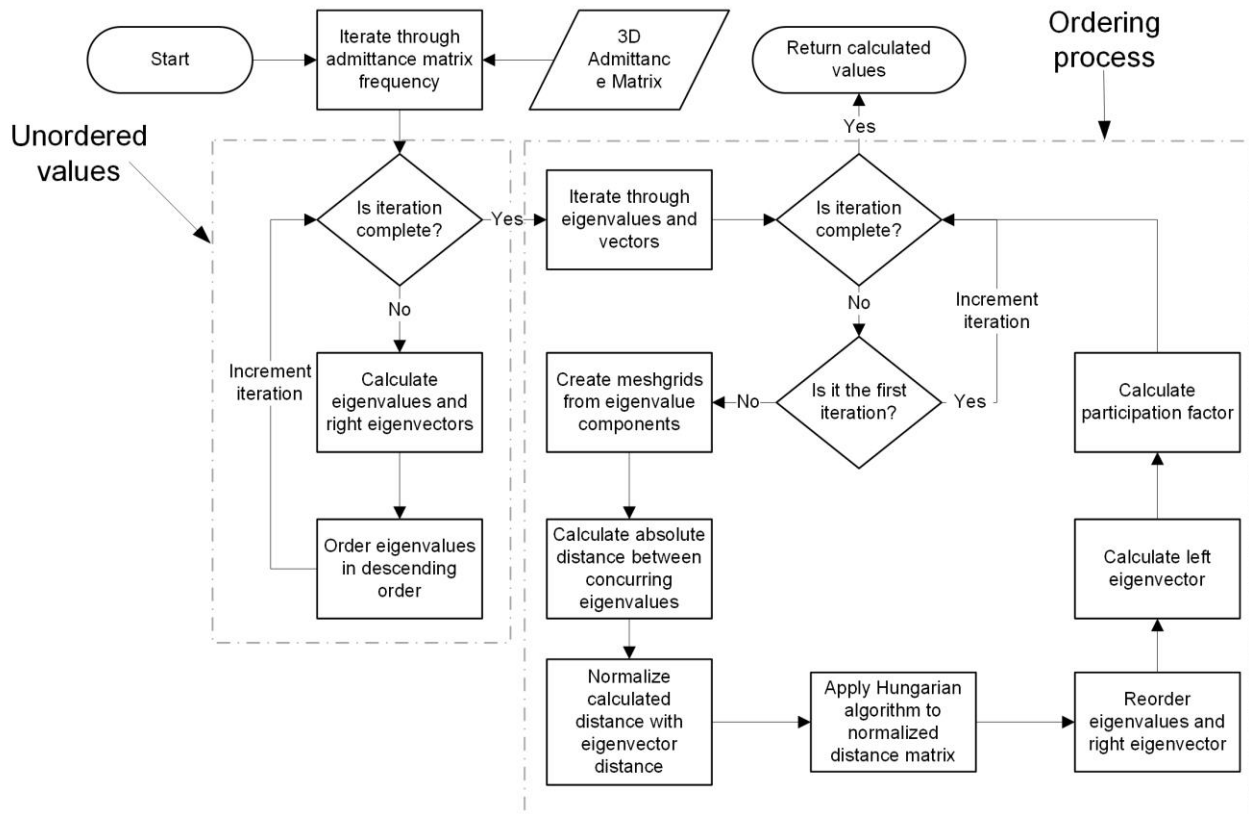


Fig. 6-10. Modal analysis and eigenvalue/vector sorting method

6.3.3 Results

The final section of the code development process involved generating clear figures depicting the results. The frequency sweep results that were obtained for a specific bus were compared to the corresponding inverse constructed admittance matrix self-impedance (illustrated in Fig. 6-13). Modes that displayed a significant resonant condition were plotted (illustrated in Fig. 6-14). Participation factors were visualised on a system figure using various circle sizes, with larger circles signifying a greater participation towards the resonant modes (included in Appendix D) and summarised using a pie chart (illustrated in Fig. 6-15).

This section only provided an overview of the output results but will be discussed in greater detail in the following sections.

6.4 Python model validation

The detailed PowerFactory model was approximated according to the characteristics of each element. This introduced slight discrepancies which needed to be evaluated to validate the approximated element values. Discrepancies that were introduced were due to ignoring the long line effect (LLE) and using the UK's National Grid Company's (NGC) correction factor model for the skin effect of overhead lines [48].

All discrepancies between the developed Python and PowerFactory models were assessed at the RPP POC namely, the Touwsrivier busbar.

6.4.1 Long line effect

The LLE is introduced for overhead lines that exceeds the 240/h km threshold [49][42]. Assessing the frequency spectrum up to the 40th or 50th harmonic (2000 Hz or 2500 Hz), as specified by regulatory bodies [25][26], caused the LLE to be considered for OHLs longer than 4.8 km.

From Table XV it can be seen that all the OHLs exceed this 4.8 km threshold and therefore need to be compared with the developed Python model which disregards the long line effect. The comparison can be seen in Fig. 6-11 and illustrates the significance of the LLE at higher frequencies. The slight frequency shift that is apparent is small enough to disregard and insignificant amplitude shifts up to 2000 Hz are present. The resonant condition between 2000 and 2500 Hz introduced the only significant divergence.

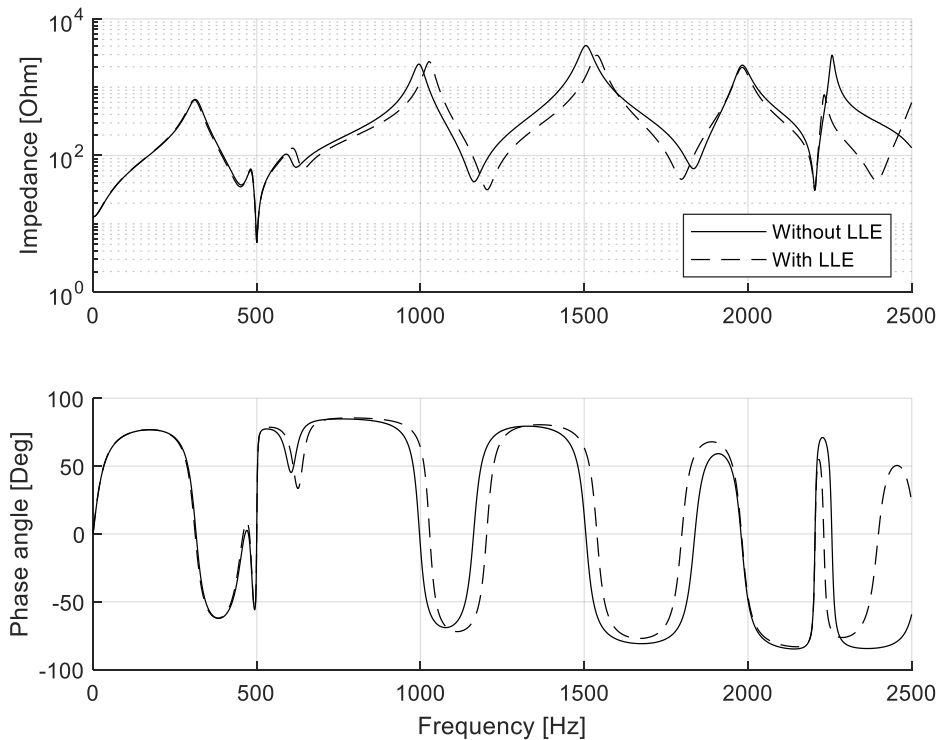


Fig. 6-11. Long line effect influence on Touwsrivier busbar impedance

The exclusion of the LLE was selected as the same number of complete resonant peaks are evident when comparing the system with and without the long line effect. This would result in a slightly different participation factor distribution for modal resonant peaks when applying RMA.

6.4.2 Skin effect

The skin effect is another effect that introduces discrepancies at higher frequencies if it is disregarded. Damping introduced by the skin effect is the main reason for including it. The damping effect that the skin effect has on the Python model is illustrated in Fig. 6-12.

The NGC correction factor for approximating the skin effect was implemented as it provided a significant resemblance to the more complex Bessel function for 132 kV systems. The NGC correction factor is defined as follows [48]:

$$R = R_1 \left(1 + \frac{0.6465h^2}{192 + 0.518h^2} \right) \quad (6.19)$$

where R is the resistance at the harmonic order h and R_1 is the resistance at the fundamental frequency.

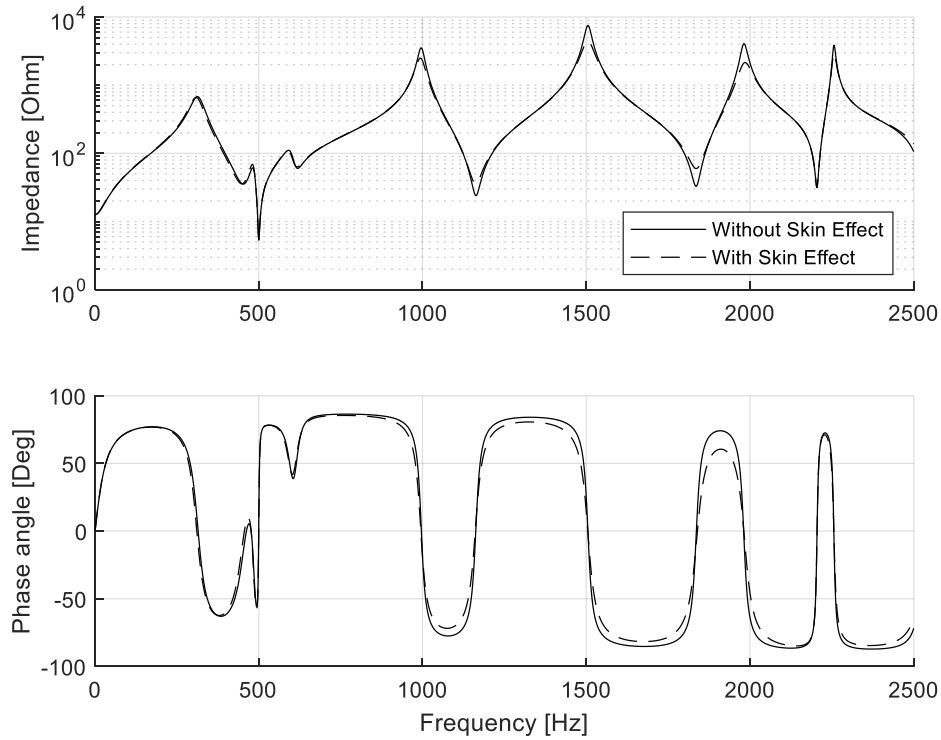


Fig. 6-12. Comparison of Python model without and with skin effect

PowerFactory uses the complex Bessel function for calculating the skin effect characteristics [50], defined as follows:

$$Z_{int} = \frac{1}{2} \times R_{DC} \times (\zeta \cdot \sqrt{-j}) \times \frac{J_0(\zeta \cdot \sqrt{-j})}{J_1(\zeta \cdot \sqrt{-j})} \quad (6.20)$$

where Z_{int} is the internal impedance of the conductor, R_{DC} is the DC resistance, J_0 and J_1 are the Bessel function of the first kind and of order zero and one respectively, and ζ is the angular wavenumber in the conductor calculated, as follows:

$$\zeta = r \times \sqrt{\frac{\omega \cdot \mu_r \cdot \mu_0}{\rho}} \quad (6.21)$$

where r is the conductor radius, ω is the angular frequency, μ_r and μ_0 are the relative permeability and the permeability of free space respectively, ρ is the resistivity of the conducting material.

The comparison between the application of the NGC and the Bessel function correction factor is illustrated in Fig. 6-13.

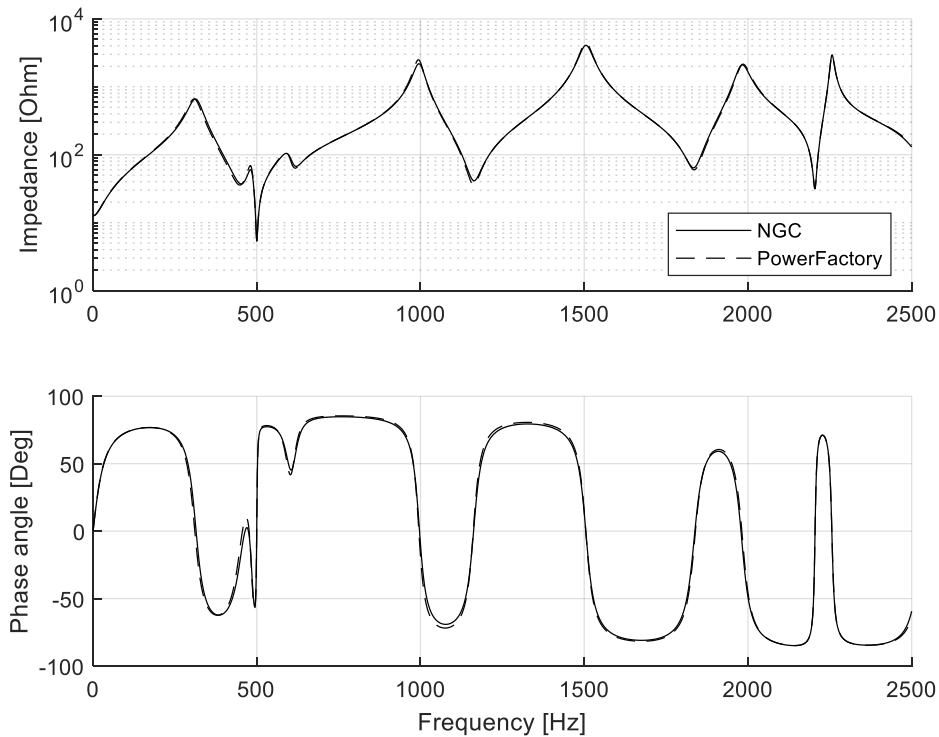


Fig. 6-13. Comparison between NGC and PowerFactory skin effects

Implementing the NGC correction factors was considered sufficient due to the negligible difference between the results in Fig. 6-13.

6.5 RMA results

Applying RMA to the developed Python model's admittance matrix produced participation factors indicating how various components in the network interact. These participation factors were calculated, as discussed previously in Chapter 5, and the results were visualised on the developed PowerFactory system, as illustrated in Appendix D.

Significant resonant conditions of the system model in Appendix A.4 needed to be identified. Transforming the system admittance matrix to the modal domain results in the identification of 7 resonant modes within the 2500 Hz evaluation frequency spectrum. These resonant modes are illustrated in Fig. 6-14.

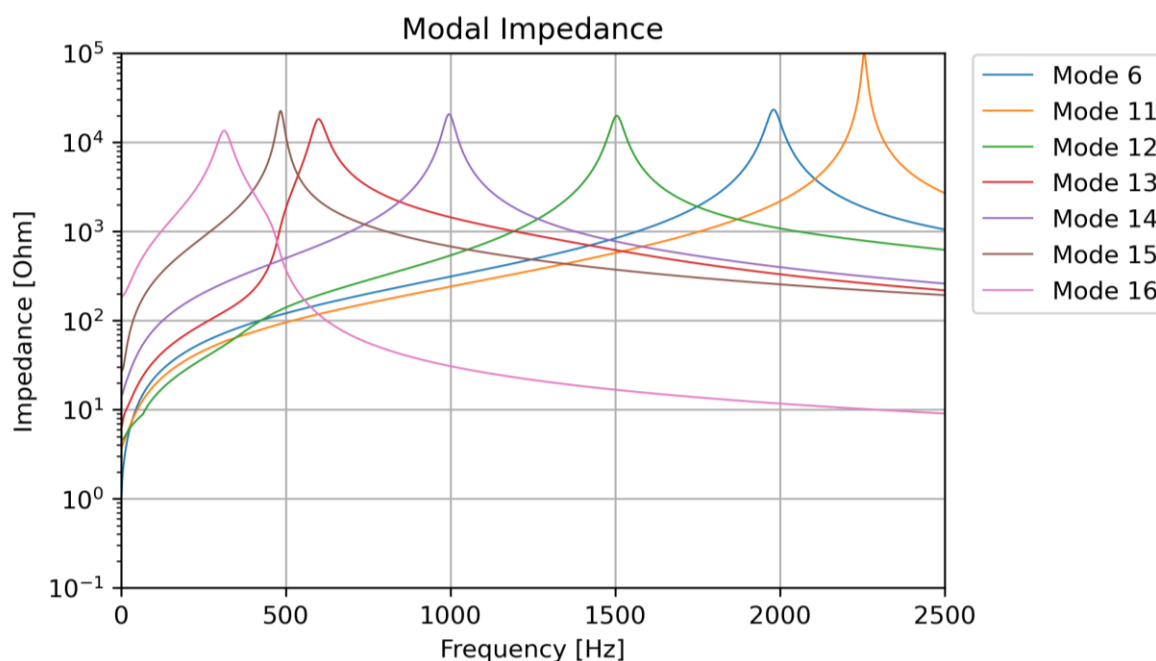


Fig. 6-14. Identified system resonant modes

These 7 resonant modes were identified from a variety of modes up to the 16th mode. The 7 resonant modes have peak resonant conditions as illustrated in

Table XVII. The additional 9 modes did not contain a resonant condition within the evaluation frequency spectrum and were therefore excluded. The complete 16 mode system plot is included in Appendix D.

Table XVII: Modal resonant frequencies of PowerFactory reduced network model

Mode	Resonant frequency
<i>Mode 6</i>	1981 Hz
<i>Mode 11</i>	2256 Hz
<i>Mode 12</i>	1505 Hz
<i>Mode 13</i>	600.3 Hz
<i>Mode 14</i>	996.1 Hz
<i>Mode 15</i>	485.0 Hz
<i>Mode 16</i>	313.7 Hz

Due to the diversity of capacitances located within the system, resonant conditions were evident throughout the entire frequency spectrum. This is due to multiple energy exchange loops introduced by capacitive elements. These capacitive elements continue to form resonant conditions at higher frequencies forming unique resonant loop conditions.

After the appropriate resonant modes and frequencies were identified the participation factors could be investigated to identify any dominant component contribution towards the resonant conditions. The contribution of each bus is illustrated in Appendix D and the installation- and network-side's aggregated contributions are defined as follows:

$$PF_{network} = \sum_{i=1}^n PF_{im}, \quad \{i \in \text{network buses}\} \quad (6.22)$$

and

$$PF_{installation} = \sum_{i=1}^n PF_{im}, \quad \{i \in \text{installation buses}\} \quad (6.23)$$

where the *network buses* are defined as all buses connected prior to the installation's connection and the *installation buses* are defined as additional buses introduced by the inclusion of the installation. The PFs that are aggregated in (6.22) and (6.23) are the participation factors associated with the specific buses *i* and specific mode *m*.

From Fig. 6-15 it is seen that the network-side has a dominant contribution towards most of the 7 resonant conditions. In the 2500 Hz evaluation frequency spectrum these resonant conditions ranged from 313 Hz to 1981 Hz.

The installation-side, referring to all the components within the installation, presented a dominant contribution at 485 Hz and 2256 Hz. These resonant conditions are attributed to the introduced inverter capacitors and the installation cabling. This corroborates the results that were presented in Chapter 4, which identified that the inverter filter capacitor and MV cabling capacitance introduced similar resonant conditions within the simplified system's analysis.

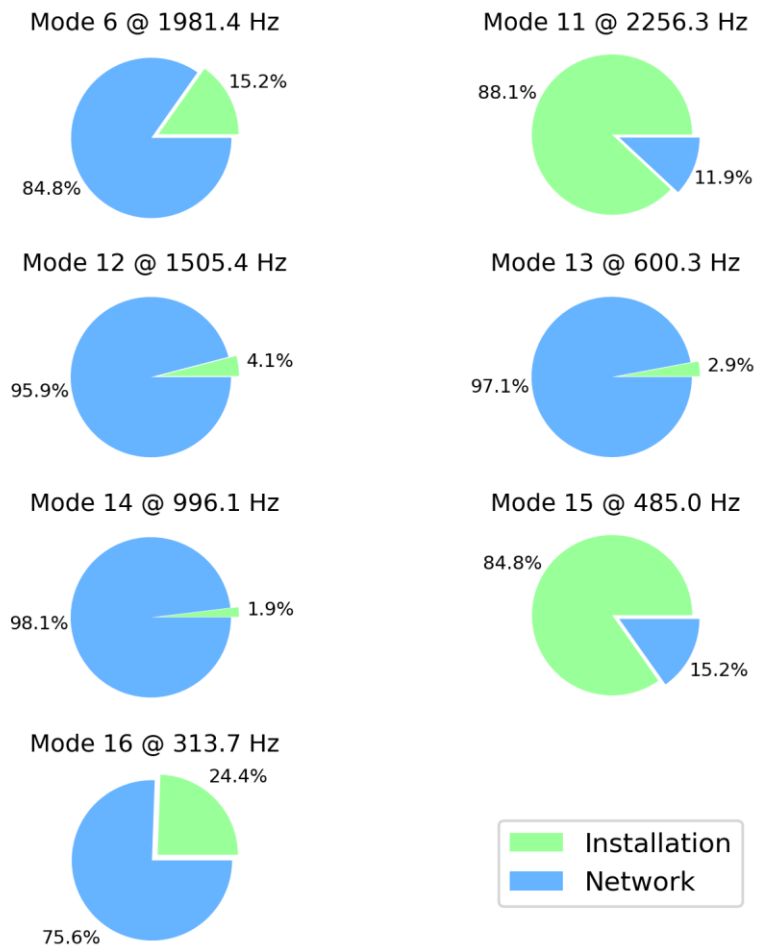


Fig. 6-15. Installation- and network-side aggregated participation towards the resonant modes

Reconstructing the system admittance matrix from all the different modes, as illustrated in Appendix D, using Eq. (5.12) provided final validation that the RMA was applied correctly. The reconstructed POC bus impedance from the modal domain can be seen in Fig. 6-16.

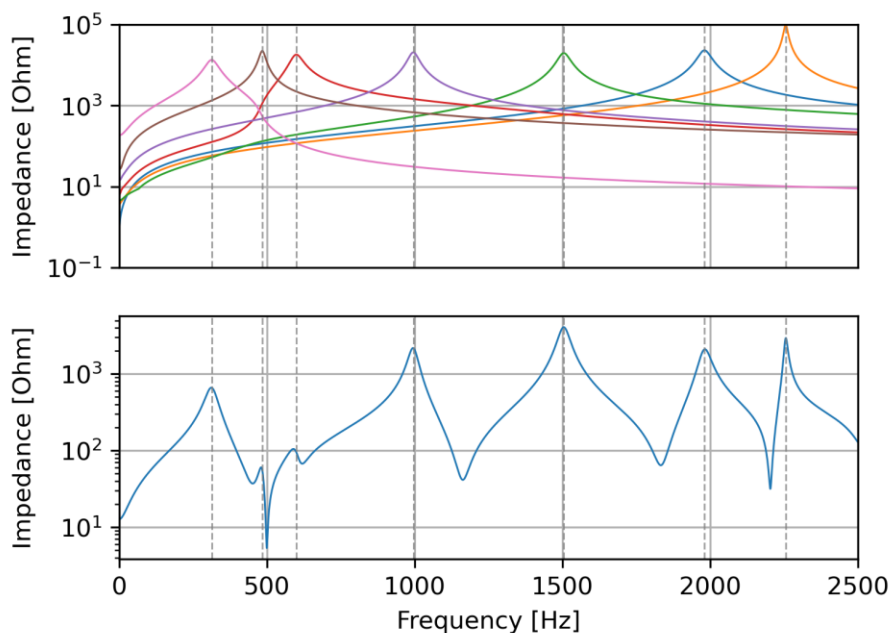


Fig. 6-16. POC bus impedance (bottom) decomposition from modal impedances (top) of reduced network PowerFactory model

As seen from Fig. 6-16, the modal domain resonant frequencies correspond with the characteristic parallel resonant conditions seen in the POC bus impedance. The modal domain results reliably represent the bus impedance and, therefore the participation of the various buses.

6.6 PowerFactory RMA propagation results

To test using participation factors for harmonic propagation analysis a harmonic current was injected, throughout the analysed frequency spectrum (up to 2500 Hz), at two buses and the propagation of the harmonic voltage distortion observed. Harmonic current was injected at the installations' inverter container bus, simulating harmonic injection from the inverters, and at the Laingsburg bus, simulating harmonic current injection from the network.

6.6.1 Harmonic voltage propagation

The harmonic voltage distortion was observed for two study cases. An excitation bus as well as two observation buses were observed for both study cases. The harmonic voltage measurements were obtained from a harmonic *loadflow* executed on the PowerFactory model.

The first study case had a harmonic current injection of 10 A, injected throughout the frequency spectrum, at the inverter containers bus. This value was derived assuming a $\pm 0.6\%$ harmonic current injection (I_{pu}) of the inverter containers' 1212 A rated current (I_R) value at 300 V (V_{LV}), after the filter.

The 60 parallel inverters' (N_{inv}) harmonic current injections were aggregated and transformed to 132 kV (V_{HV}). The injection value after the filter was assumed to be 10% ($I_{\%}$) of the total harmonic current injection before the filter leading to an equivalent harmonic injection as follows:

$$\begin{aligned} I_o &= I_{pu} \times I_R \times N_{inv} \times \frac{V_{LV}}{V_{HV}} \times \frac{100}{I_{\%}} \\ &= 0.0061 \times 1212 \times 60 \times \frac{300}{132000} \times \frac{100}{10} = 10.08 \text{ A} \end{aligned} \quad (6.24)$$

This injected harmonic current, injected at integer multiples of the fundamental frequency, induces harmonic voltage distortions throughout the system, as illustrated in Fig. 6-17. Harmonic voltage distortion (blue) and transfer impedance approximated harmonic voltage distortion (black) for a 10 A @ 132 kV harmonic current injection at the inverter containers. The harmonic voltage distortion was approximated using the sum of the cross-participation factors and the system eigenvalues to approximate the transfer impedance, as illustrated in (5.13).

The implementation of the transfer impedance, using (5.13), was introduced to illustrate the relationship between the harmonic voltage distortion at the injection bus (l) and the observation bus (k). This relationship for a single harmonic current injection is defined as:

$$\begin{aligned} \frac{\bar{V}_k}{\bar{I}_l} = Z_{lk} \\ \frac{\bar{V}_l}{\bar{I}_l} = Z_{ll} \end{aligned} , \quad \begin{cases} \bar{I}_l \neq 0 \\ \bar{I}_{1,2,\dots,n} = 0 \end{cases} \quad (6.25)$$

$$\begin{aligned} \frac{\bar{V}_k}{\bar{I}_l} \times \frac{\bar{I}_l}{\bar{V}_l} &= \frac{Z_{lk}}{Z_{ll}} \\ \frac{\bar{V}_k}{\bar{V}_l} &= \frac{Z_{lk}}{Z_{ll}} \\ \bar{V}_k &= \frac{\bar{V}_l}{Z_{ll}} \times Z_{lk} \end{aligned} \quad (6.26)$$

where Z_{lk} is the transfer impedance between the injection (l) and observation (k) buses, calculated using (5.13), Z_{ll} is the injection bus self-impedance, calculated using (5.12), \bar{V}_l is the voltage distortion at the injection bus and \bar{V}_k is the voltage distortion at the observation bus.

This relationship allows for the identification of buses which will experience greater harmonic voltage distortion levels.

RPP installation harmonic current emission

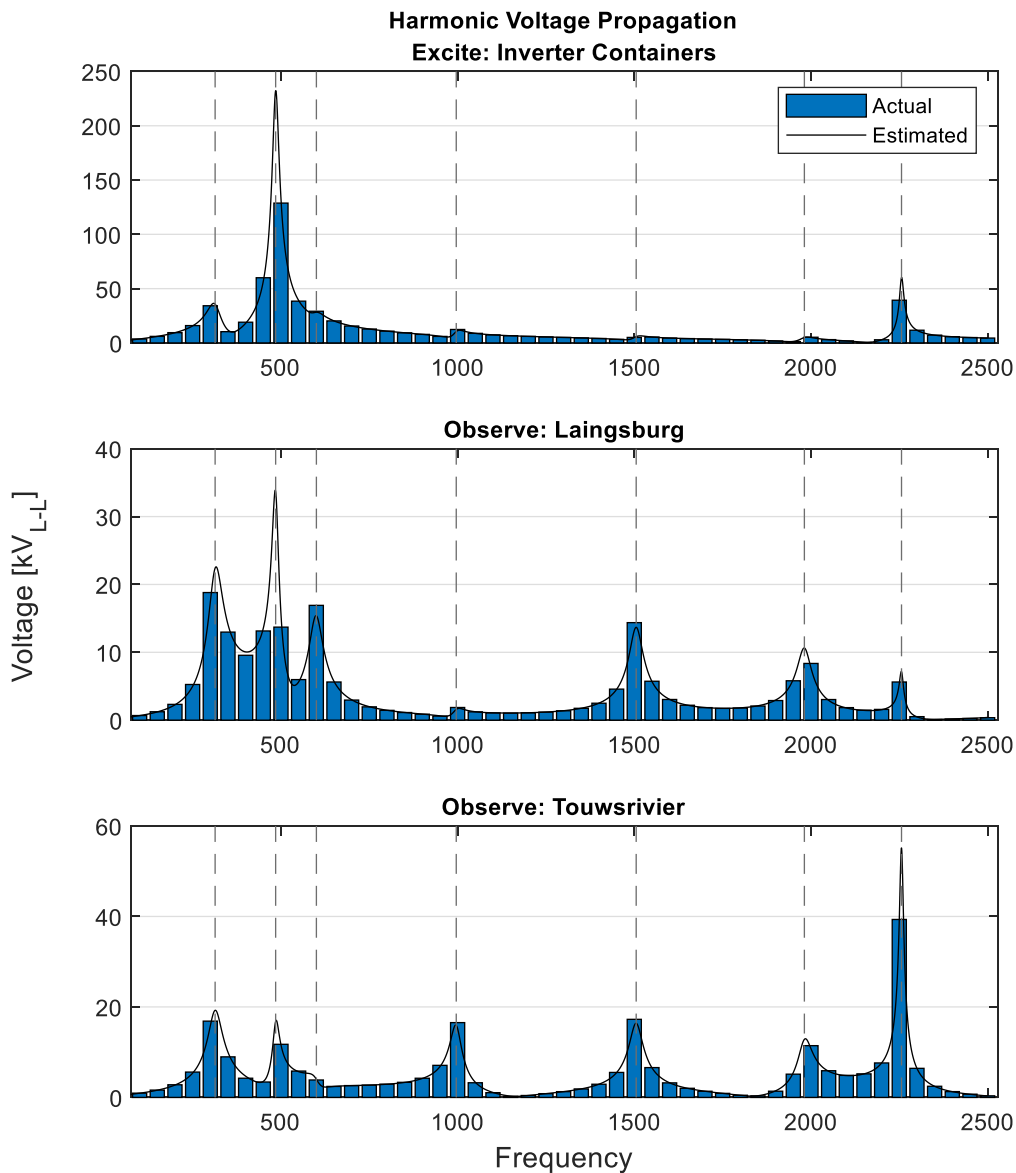


Fig. 6-17. Harmonic voltage distortion (blue) and transfer impedance approximated harmonic voltage distortion (black) for a 10 A @ 132 kV harmonic current injection at the inverter containers

From Fig. 6-17 resonant conditions are identified, and the amplification effect caused by these resonant conditions is illustrated. The harmonic voltage distortion at the point of injection primarily correlates with the transfer impedance as it represents the self-impedance of the bus. The estimated values as illustrated in Fig. 6-17 correlate with the actual harmonic voltage values acquired from the PowerFactory simulation.

The estimated values are slightly lower than the actual values due to the over-estimation of damping introduced by the simplified skin effect formula, (6.19), introduced in the admittance matrix construction. This slightly lower estimated harmonic voltage distortions are insignificant but can be

observed at the 1000 Hz and 1500 Hz harmonic voltage components which occurs very closely to peak resonant conditions.

Investigating the observation buses' resonant condition results, illustrated in Table XVIII, of the first study case from the Laingsburg and Touwsrivier observation buses corroborated (6.26). The ratio between an observation buses transfer impedance and an excitation buses self-impedance were roughly equivalent to their harmonic voltage distortion ratio.

Table XVIII: Transfer impedance and harmonic voltage distortion for selected system buses with a 10 A @ 132 kV harmonic current injection at the inverter containers

		Frequency [Hz]	300	500	600	1000	1500	2000	2250
Transfer Impedance [Ohm]	<i>Inverters</i>		1942 Ω	7703 Ω	1632 Ω	651.8 Ω	286.5 Ω	290.7 Ω	2277 Ω
	<i>Laingsburg</i>		1000 Ω	907.2 Ω	888.8 Ω	98.27 Ω	762.9 Ω	445.1 Ω	313.4 Ω
	<i>Touwsrivier</i>		910.6 Ω	674 Ω	233.1 Ω	876.9 Ω	916.5 Ω	622.5 Ω	2276 Ω
Harmonic Voltage Distortion [pu]	<i>Inverters</i>		0.2593	0.9758	0.2210	0.0939	0.0384	0.0398	0.2980
	<i>Laingsburg</i>		0.1425	0.1039	0.1282	0.0142	0.1089	0.0633	0.0426
	<i>Touwsrivier</i>		0.1277	0.889	0.0292	0.1252	0.1308	0.0867	0.2980

From Table XVIII and Fig. 6-17 it can be observed that the harmonic propagation at the lower end of the frequency spectrum propagates far into the network reaching Laingsburg, which is located more than 100 km from the injection point. The almost 1 pu harmonic voltage distortion observed at the aggregated inverters terminal, introduced due to the high impedance seen from the inverter terminals where the harmonic current is injected, quickly dissipates within the installation and reduces to 0.0889 and 0.1039 pu when it reaches the POC bus at Touwsrivier and Laingsburg.

It is also observed that the 2250 Hz harmonic voltage distortion does not dissipate as it propagates from the inverter terminals towards the Touwsrivier bus but significantly dissipates as it propagates further into the network towards Laingsburg. This can be attributed to higher frequency harmonics dissipating through network capacitive coupling as the impedance presented by this capacitance is low as high frequencies.

The second study case also had a 10 A harmonic current injection, throughout the entire frequency spectrum, but this time at a bus on the network. The Laingsburg bus was chosen as the bus where

the harmonic current would be injected. This represents a harmonic injection from equipment connected to the Laingsburg network. The results of this study case are illustrated in Fig. 6-18.

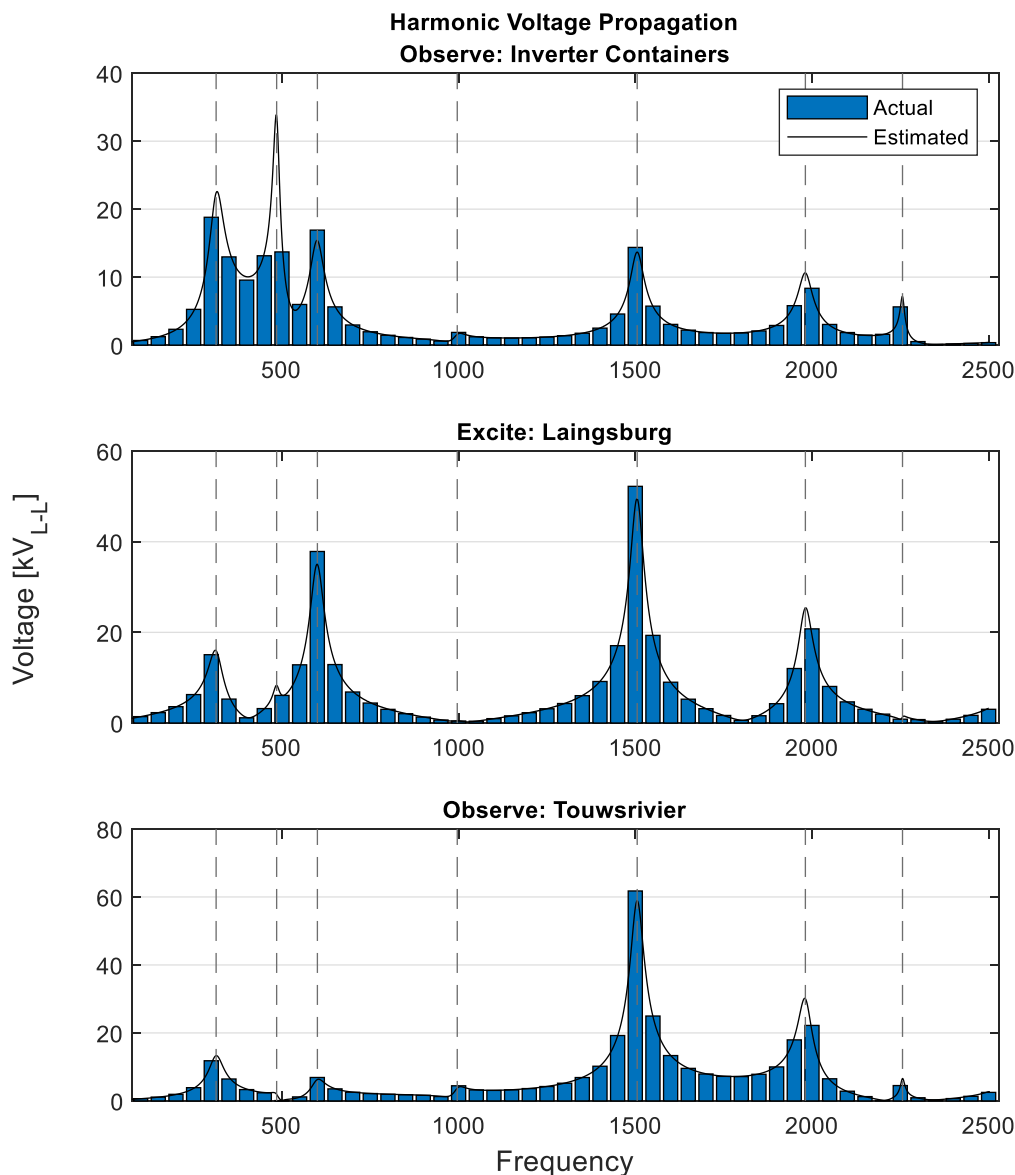


Fig. 6-18. Harmonic voltage distortion (blue) and transfer impedance approximated harmonic voltage distortion (black) for harmonic current injection from the Laingsburg busbar

Applying the same analysis on the second study case reiterates the ratios as suggested by (6.26). The summary of the resonant condition results is illustrated in Table XIX. The overlaid approximation of the harmonic voltage distortion is once again lower due to a higher damping factor but correlates with the actual harmonic voltage distortion.

Table XIX: Transfer impedance and harmonic voltage distortion for selected system buses with 10 A @ 132 kV harmonic current injection at the Laingsburg busbar

		Frequency [Hz]	300	500	600	1000	1500	2000	2250
Transfer Impedance [Ohm]	<i>Inverters</i>		1000 Ω	907.2 Ω	888.8 Ω	98.27 Ω	762.9 Ω	445.1 Ω	313.4 Ω
	<i>Laingsburg</i>		822.3 Ω	355.3 Ω	2021 Ω	26.49 Ω	2774 Ω	1121 Ω	47.71 Ω
	<i>Touwsrivier</i>		628.2 Ω	7.175 Ω	362.3 Ω	234.2 Ω	3278 Ω	1182 Ω	251.6 Ω
Harmonic Voltage Distortion [pu]	<i>Inverters</i>		0.1425	0.1039	0.1282	0.0142	0.1089	0.0633	0.0426
	<i>Laingsburg</i>		0.1142	0.0461	0.2867	0.0034	0.3956	0.1574	0.0064
	<i>Touwsrivier</i>		0.0895	0.0008	0.0522	0.0337	0.4679	0.1683	0.0342

From Table XIX and Fig. 6-18 it can be observed that lower frequency harmonics dissipate within the network as it propagated towards the Touwsrivier bus over a distance of ±100 km but is amplified within the installation due to a higher transfer impedance towards the aggregated inverters terminal.

The higher frequency harmonics increases as it propagates from the Laingsburg bus towards the Touwsrivier bus with the aggregated inverter terminals not observing high harmonic distortion expect at the 2250 Hz component for which the installation has 'n dominant contribution as illustrated by the participation factors in Appendix D.

6.6.2 Harmonic current propagation

Having investigated the propagation of harmonic voltage the harmonic voltage values can be implemented along with the impedance matrix to convert the harmonic voltage values to harmonic current equivalent values. The harmonic current that propagated towards the various buses were calculated using the approximated harmonic voltage distortion values as the previous section proved that the approximated results are accurate enough to implement on the system.

The propagation of harmonic current is defined as follows [21]:

$$\bar{I}_{jk} = \frac{\bar{V}_l - \bar{V}_k}{Z_{jk}} \quad (6.27)$$

where I_{lk} is the propagation harmonic current between the excitation and observation bus, \bar{V}_l is the harmonic voltage at the excitation bus, \bar{V}_k is the harmonic voltage at the observation bus and Z_{lk} is the transfer impedance between the excitation and observation bus.

The harmonic current equivalent values, calculated using (6.27), for the measured voltage distortion values are illustrated in Fig. 6-19 and Fig. 6-20.

The harmonic current propagation for the first study case is illustrated in Fig. 6-19. The inverter containers bus indicates the 10 A harmonic current injection at each integer harmonic frequency whilst the remaining buses indicate the propagation of the injected harmonic current.

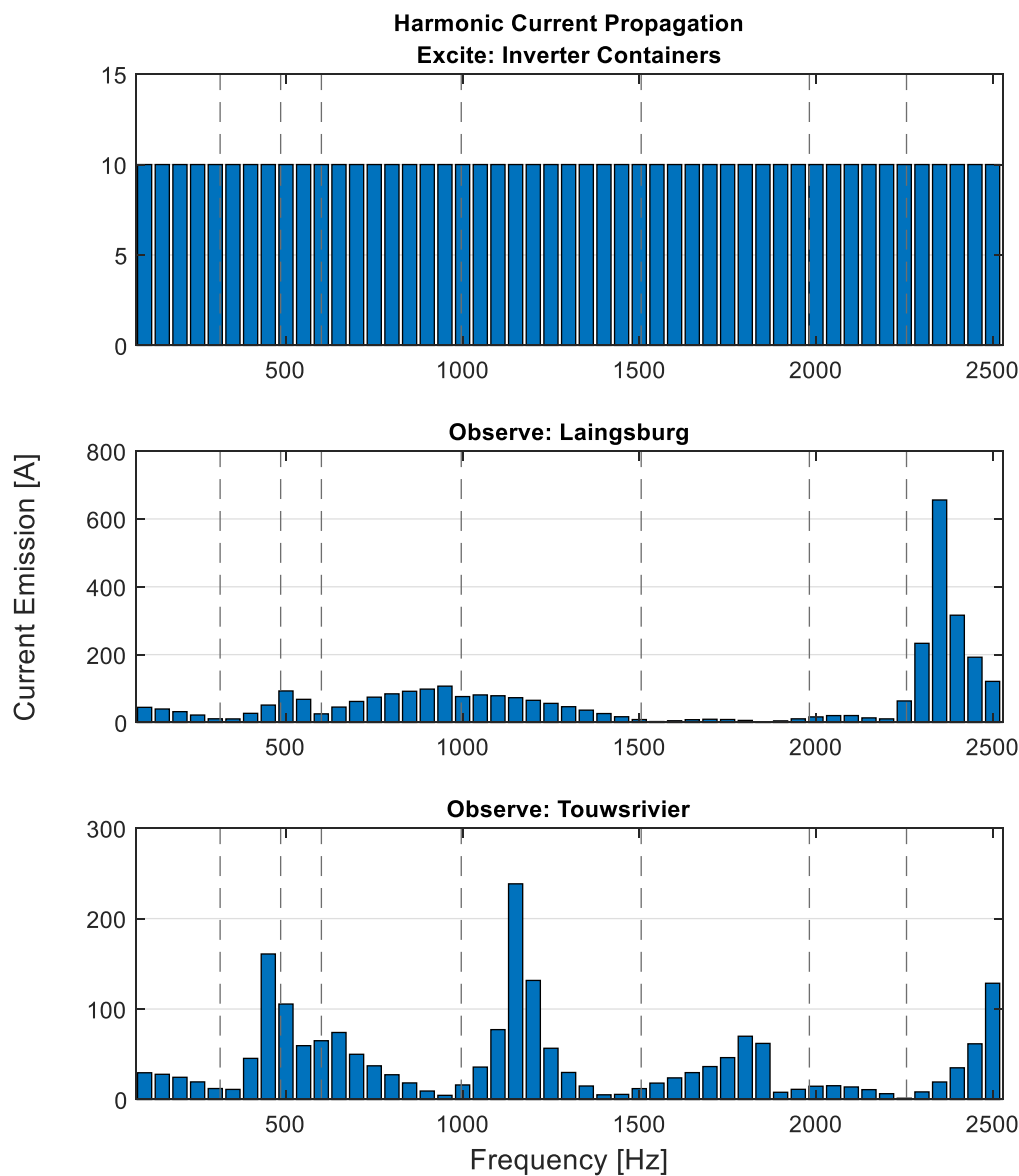


Fig. 6-19. Harmonic current propagation for harmonic current injection at the inverter containers

From Fig. 6-19 significant amplification of the injected harmonic current can be observed at both observation buses. The most significant harmonic current distortion is realized at the frequency which the excitation bus has the greatest participation factor towards the resonant condition. The participation factor includes the excitability of the bus illustrating the applicability of using RMA to identify the frequency at which the excitation bus will influence the rest of the system.

The harmonic current propagation for the second study case is illustrated in Fig. 6-20. The Laingsburg bus is used as the excitation bus this time with the remaining buses operating as observation buses. The same amount of harmonic current was injected at the Laingsburg bus as was injected at the inverter containers in the first study case to maintain the current injection control variable.

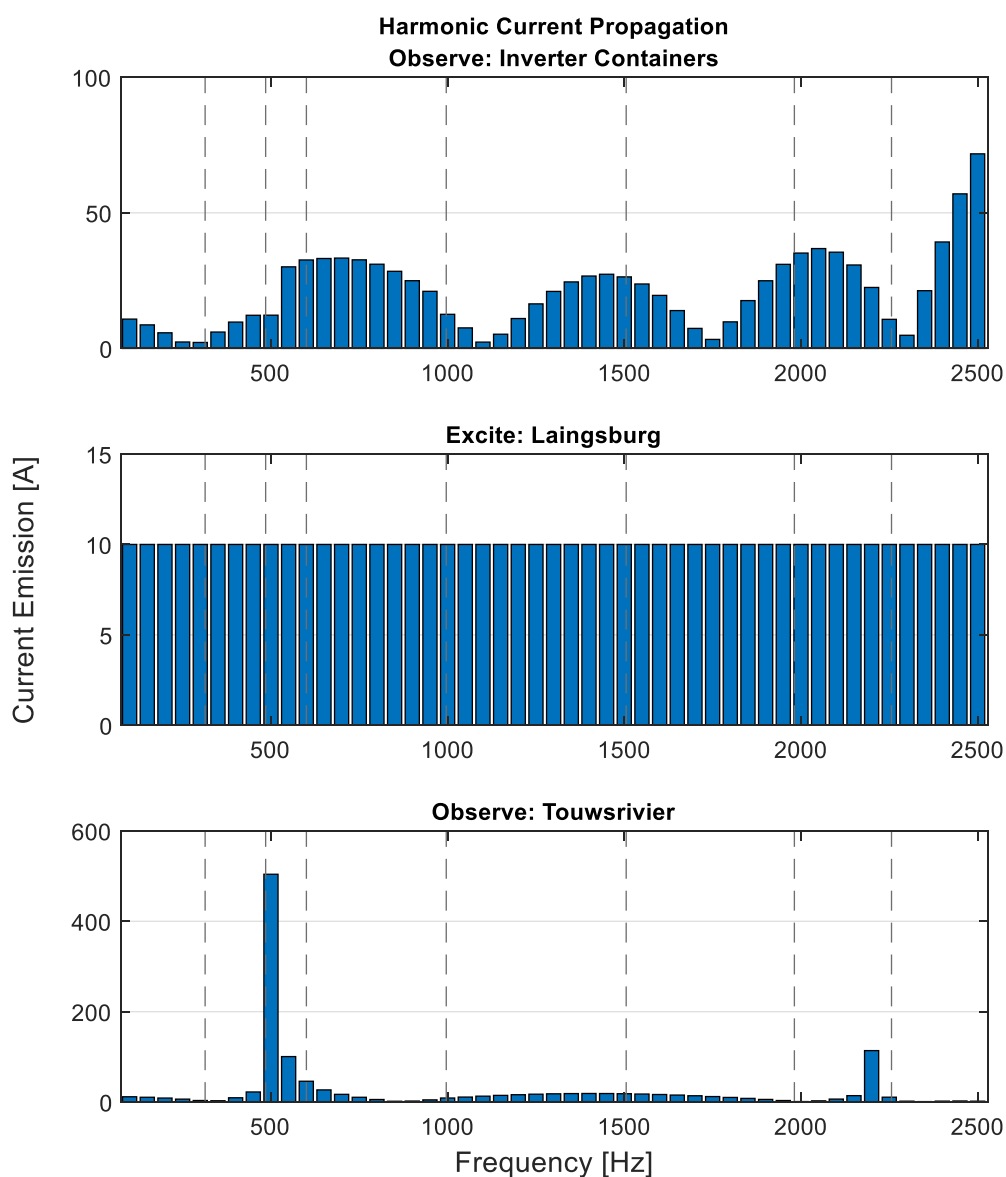


Fig. 6-20. Harmonic current propagation for harmonic current injection at the Laingsburg busbar

From Fig. 6-20 the resonant conditions where the Laingsburg bus has the greatest participation factors are amplified the most significantly throughout the observation buses. Comparing these amplifications with the amplifications observed in the first study case reveals that a more significant participation factor induces greater harmonic current amplification throughout the network.

6.7 Conclusion

The developed detailed PowerFactory model of a complex power system was adapted to reduce the number of resonating elements present in the model. This allowed for greater insight into the contribution that the selected elements had towards the resonant conditions.

The developed reduced PowerFactory model was analysed using the PowerFactory Python API and a method for automatically constructing the positive sequence admittance matrix was developed in Python. RMA was subsequently performed on the constructed admittance matrix.

The RMA results provided insight into individual contributions towards resonant mode conditions, illustrated in Appendix D, as well as the aggregated installation/network contributions. This corroborated the findings from Chapter 5 which identified the inverter filter capacitor and installation cabling capacitance as the dominant contributors towards two of the resonant conditions at a low and high frequency, respectively.

The installation in conjunction with several network reactive elements interact to introduce a low (485 Hz) and high frequency (2256.3 Hz) resonant condition, similar to the previously identified contributing components of the simplified installation model in Chapter 4. The participation factors helped to identify the dominant source of these two resonant conditions, attributed towards the inverter filter capacitors and MV cabling capacitance, respectively. Even though various modes did not present a significantly dominant contribution but a clear distinction between network components and installation components could be made, as illustrated in Fig. 6-15.

The propagation of harmonic voltage and current was also determined using cross participation factors to calculate the transfer impedance. The harmonic voltage propagation was determined through a harmonic *loadflow* simulation performed on the developed PowerFactory model and was illustrated in Fig. 6-17 and Fig. 6-18. The harmonic voltage propagation on the developed model coincided with the estimated combined contribution values of the various modes of the system.

The harmonic current propagation was calculated using the estimated harmonic voltage distortion values. This was achieved using (6.27) to determine the transfer current that propagates from the

excitation bus to the observation bus. The estimated propagation current was illustrated in Fig. 6-19 and Fig. 6-20, with the excitation bus indicating the injection harmonic current.

The implementation of Python in conjunction with PowerFactory models has made it possible to analyse more complex systems without requiring remodelling of the PowerFactory models. The additional network-side reactive elements also significantly increased the complexity of resonant conditions. The automation of this analysis can therefore be extended to larger power system.

7 Conclusions

This chapter covers the findings and conclusions of this study's research questions. The results and contributions thereof are discussed accordingly. Recommendations for future research to expand upon this research is discussed.

7.1 Summary

This study set out to identify the effects and causes of resonant conditions, as well as to quantify the contribution that various types of equipment have on these resonant conditions. RPPs were identified to introduce two critical capacitive elements in the power system model, namely, the cabling capacitance and the inverter filter capacitors that introduce additional resonant conditions. The network, however, consists of various capacitive elements that introduce a significant number of resonant conditions.

An analytical impedance-based approach was implemented to identify resonant loops introduced by various elements in a simplified system model. Propagation analyses were performed using the developed analytical models to identify the effects of resonant conditions.

Resonant mode analysis was incorporated as a method to decouple the contributions of various elements to the identified resonant conditions. Using dominant modal domain impedances, the contribution of each bus in the power system could be evaluated and used to illustrate the effect that the connected buses' elements have towards specific resonant conditions. This process allows for an accountability assessment of the power system as the cause of resonant conditions introduces harmonic voltage distortion amplification throughout the entire network.

Lastly, Python was implemented to construct the power system admittance matrix automatically easing the process required to perform RMA on the corresponding admittance matrix. PowerFactory's Python API proved to provide significant functionality and enabled the construction of the admittance matrix which could not be exported from the PowerFactory model.

7.2 Main conclusions to objectives

Identifying harmonic generating mechanisms. VSDs and inverters were reviewed in Chapter 2 and identified as a major source of harmonic distortion in RPP installations connected to the power system. The effect of sampling in VSIs introduce additional harmonic current emissions throughout the frequency spectrum. The amplification of these harmonic current emissions is caused by resonant conditions introduced by the interaction of reactive elements throughout the entire power system.

Modelling of simplified RPP. The simplified aggregate modelling process that was followed for the case study RPP proved to be successful in representing the impedance of a complex RPP installation. The validation process identified significant similarities between the detailed RPP installation model developed in PowerFactory and the simplified aggregated model developed in MATLAB.

Harmonic impedance analysis. Through an impedance-based analytical approach, the interaction between various elements in a simplified power system was illustrated. The results identified that characteristic parallel resonant conditions exist throughout the entire power system, while series resonant conditions varied. Through propagation analysis, the parallel resonant conditions were identified as the cause for harmonic current emission amplification.

Modal domain analysis. RMA was incorporated to analyse the power system in the modal domain. The interaction of system elements was further analysed in the modal domain, where resonant conditions are decoupled, and quantified using PFs. It was concluded that complex systems are more appropriately assessed using RMA as it becomes difficult to model larger power systems using the impedance-based analytical approach.

DigSILENT PowerFactory modelling. Models were developed in PowerFactory and used to approximate static network conditions, as well as develop the simplified RPP installation model. PowerFactory provided a comprehensive suite of tools to develop accurate models but lacked the capability to export a system admittance matrix required for RMA.

Python programming. Python was implemented to construct the admittance matrix. The implementation of the PowerFactory Python API required reviewing the API documents to be able to analyse individual components in the power system and construct the admittance matrix. The admittance matrix was found to produce corresponding results to those generated by the frequency sweeps in PowerFactory.

7.3 Contributions

The relevant contributions of this thesis are discussed.

A simplification process for developing a single-phase equivalent model of a large RPP installation was described. This provides guidelines for aggregating a large RPP, providing simplifications and assumptions that were required in the process of the development.

An impedance-based analysis of the simplified system model was performed to illustrate resonant loops introduced by capacitive elements. This presented an intuitive illustration of the interaction between components within a simplified system, specifically the dominant loops introduced by the installation cabling capacitance and the inverter filter capacitors.

RMA was investigated as a method to analyse the contribution of various power system elements to specific resonant conditions. This provided a means to identify dominant contributing elements that cause resonant conditions and subsequently, amplification of harmonics.

Python programming used to develop the system admittance matrix of a PowerFactory model introduced additional modularity capabilities, easing the process of obtaining the admittance matrix for the RMA. The developed Python code enabled modelling of more complex power systems to be performed in PowerFactory and still perform RMA on the power system.

7.4 Future research

Some challenges associated with this study and possible methods for improvements in the future are presented below.

Modelling methodology. The simplified modelling methodology could be expanded to include more comprehensive models of grounded cables and transformers. An equivalent π -circuit and second-order harmonic transformer could be implemented for the MV cabling capacitance and the installation transformers, respectively. It is, however, suggested that further modelling of larger power systems be developed in PowerFactory, simplifying the modelling process significantly.

Python admittance matrix construction. Currently the code developed for the construction of the power system admittance matrix is limited to the components that were required to develop the admittance matrix of the specific power system. Inclusion of additional elements to the power system's admittance matrix construction methodology would require adding methods for each of the additional elements. This would enable greater modularity and functionality to the developed method and would allow

different types of loads, sources, transformers, branch and shunt elements and filters to be added to the power system to further expand on the contribution of different types of connected elements.

Power system simulation. The power system investigated in this thesis was a static system that was considered for a single operating condition. The inclusion of various operating conditions, implementing stochastic network conditions, would provide a greater scope of the effect of different amounts of network loading as well as equipment failures throughout the network. This could be achieved by implementing the Monte Carlo simulation method on various simulation parameters.

Data analysis. This thesis focused on the principle of identifying resonant conditions and the causes thereof through simulations and the implementation of RMA. Even though data was acquired from the case study RPP, it could not be used to validate propagation analyses as presented in this thesis. The propagation of harmonics should be evaluated on a physical model of an RPP by taking simultaneous current and voltage measurements throughout various points in the power system. These results could then be compared against the simulated propagation results obtained from the RMA.

8 References

- [1] S. Liang, Q. Hu, and W. Lee, "A Survey of Harmonic Emissions of a Commercially Operated Wind Farm," *IEEE Trans. Ind. Appl.*, vol. 48, no. 3, pp. 1115–1123, 2012.
- [2] N. Hamzah, A. Mohamed, and A. Hussain, "A New Method to Detect the Source of Harmonic at the Point of Common Coupling," *J. Tek. Gelagar*, vol. 17, no. 1, pp. 54–63, 2006.
- [3] Wilsun Xu and Yilu Liu, "A Method for Determining Customer and Utility Harmonic Contributions at the Point of Common Coupling," *IEEE Trans. Power Deliv.*, vol. 15, no. 2, pp. 804–811, 2000.
- [4] W. Xu, X. Liu, and Y. Liu, "An Investigation on the Validity of Power-Direction Method for Harmonic Source Determination," *IEEE Trans. Power Deliv.*, vol. 18, no. 1, pp. 214–219, 2003.
- [5] Department of Mineral Resources and Energy, "Integrated Resource Plan 2019," 2019.
- [6] Eskom Holdings SOC Ltd, "Integrated Report 2020," 2020.
- [7] Department of Minerals and Energy, "The South African Energy Sector Report 2019," Pretoria, 2019.
- [8] J. K. Phipps, J. P. Nelson, and P. K. Sen, "Power Quality and Harmonic Distortion on Distribution Systems," *IEEE Trans. Ind. Appl.*, vol. 30, no. 2, pp. 476–484, 1994.
- [9] International Electrotechnical Commission, "Electromagnetic compatibility (EMC) – Part 2: Environment - Section 1: Description of the environment - Electromagnetic environment for low-frequency conducted disturbances and signalling in public power supply systems," 1990.
- [10] S. K. Khadem, M. Basu, and M. F. Conlon, "Power Quality in Grid connected Renewable Energy Systems: Role of Custom Power Devices," in *International Conference on Renewable Energies and Power Quality*, 2010, pp. 1–6.
- [11] J. Arrillaga and N. R. Watson, *Power System Harmonics*, 2nd ed. John Wiley & Sons Ltd, 2003.
- [12] Y. Liu and G. T. Heydt, "Power system even harmonics and power quality indices," *Electr.*

Power Components Syst., vol. 33, no. 8, pp. 833–844, 2005.

- [13] N. Mohan, T. M. Undeland, and W. P. Robbins, *Power Electronics: Converters, Applications, and Design*. John Wiley & Sons, 2003.
- [14] S. Hansen, L. Asiminoaei, and F. Blaabjerg, "Simple and Advanced Methods for Calculating Six-Pulse Diode Rectifier Line-Side Harmonics," in *38th IAS Annual Meeting on Conference Record of the Industry Applications Conference*, 2003, pp. 2056–2062.
- [15] D. G. Holmes and T. A. Lipo, "Modulation of One Inverter Phase Leg," *Pulse Width Modul. Power Convert.*, 2010.
- [16] E. Fuchs and M. Masoum, *Power Quality in Power Systems and Electrical Machines*. Elsevier, 2008.
- [17] H. S. Black, *Modulation Theory*. New York : Van Nostrand Reinhold, 1953.
- [18] H. D. T. Mouton, B. McGrath, D. G. Holmes, and R. H. Wilkinson, "One-dimensional spectral analysis of complex PWM waveforms using superposition," *IEEE Trans. Power Electron.*, vol. 29, no. 12, pp. 6762–6778, 2014.
- [19] "Grid Connection Code for Renewable Power Plants (RPPs) connected to the Electricity Transmission System (TS) or the Distribution System (DS) in South Africa." National Energy Regulator of South Africa, 2016.
- [20] Electricity Suppliers Liaison Committee, "NRS 048-2:2003," 2003.
- [21] A. A. Mahmoud and R. D. Shultz, "A Method for Analyzing Harmonic Distribution in A.C. Power Systems," *IEEE Trans. Power Appar. Syst.*, vol. PAS-101, no. 6, pp. 1815–1824, 1982.
- [22] J. Holtz and H.-J. Klein, "The Propagation of Harmonic Currents Generated by Inverter-Fed Locomotives in the Distributed Overhead Supply System," *IEEE Trans. Power Electron.*, vol. 4, no. 2, pp. 168–174, 1989.
- [23] D. Tong, V. G. Nikolaenko, N. Ginbey, and I. Lau, "Harmonic Propagation in Transmission System with Multiple Capacitor Installations," in *PowerCon 2000. 2000 International Conference on Power System Technology. Proceedings (Cat. No.00EX409)*, 2000, vol. 2, pp. 1007–1012.
- [24] V. E. Wagner *et al.*, "Effects of Harmonics on Equipment," *IEEE Trans. Power Deliv.*, vol. 8, no. 2, pp. 672–680, 1993.

- [25] International Electrotechnical Commission, “Electromagnetic compatibility (EMC) – Part 3-6: Assessment of harmonic emission limits for the connection of distorting installations to MV, HV and EHV power systems,” 2008.
- [26] “IEEE Recommended Practice and Requirements for Harmonic Control in Electric Power Systems,” *IEEE Std 519-2014 (Revision IEEE Std 519-1992)*, pp. 1–213, 2014.
- [27] JWG Cigré C4.103, “Assessment of Emission Limits for the Connection of Disturbing Installations to Power Systems,” 2007.
- [28] JWG Cigré C4.109, “Review of Disturbance Emission Assessment Techniques,” 2011.
- [29] T. M. Blooming and D. J. Carnovale, “Application of IEEE STD 519-1992 Harmonic Limits,” *Conf. Rec. 2006 Annu. Pulp Pap. Ind. Tech. Conf.*, pp. 1–9, 2006.
- [30] International Electrotechnical Commission, “Electromagnetic compatibility (EMC) - Part 4-30: Testing and measurement techniques - Power quality measurement methods,” 2015.
- [31] F. M. Mwaniki, “Modelling and Performance Evaluation of a Pseudo-Random Impulse Sequence for In situ Parameter Estimation in Energy Applications,” Stellenbosch University, 2020.
- [32] Aurecon South Africa (Pty) Ltd, “Touwsrivier CPV Quality of Supply Assessment Rev. 2,” 2018.
- [33] I. J. Pérez-Arriaga, G. C. Verghese, and F. C. Scheweppe, “Selective Modal Analysis with Applications to Electric Power Systems, Part I: Heruistic Introduction,” *IEEE Trans. Power Appar. Syst.*, vol. PAS-101, no. 9, pp. 3117–3125, 1982.
- [34] P. Kundur, *Power System Stability And Control by Prabha Kundur*. New York: McGraw-Hill, 1994.
- [35] W. Xu, Z. Huang, Y. Cui, and H. Wang, “Harmonic Resonance Mode Analysis,” *IEEE Trans. Power Deliv.*, vol. 20, no. 2, pp. 1182–1190, 2005.
- [36] M. Esmaili, H. Ali Shayanfar, and A. Jalilian, “Modal analysis of power systems to mitigate harmonic resonance considering load models,” *Energy*, vol. 33, no. 9, pp. 1361–1368, 2008.
- [37] L. Hong, W. Shu, J. Wang, and R. Mian, “Harmonic Resonance Investigation of a Multi-Inverter Grid-Connected System Using Resonance Modal Analysis,” *IEEE Trans. Power Deliv.*, vol. 34, no. 1, pp. 63–72, 2019.

- [38] D. Scheepers and J. Beukes, "Understanding Resonance in a Renewable Energy Power Plant," *Renew. Energy Power Qual. J.*, vol. 18, pp. 397–402, 2020.
- [39] B. Badrzadeh, M. Gupta, N. Singh, A. Petersson, L. Max, and M. Høgdahl, "Power System Harmonic Analysis in Wind Power Plants - Part I: Study Methodology and Techniques," in *2012 IEEE Industry Applications Society Annual Meeting*, 2012, pp. 1–11.
- [40] J. Rodríguez *et al.*, "Predictive Current Control of a Voltage Source Inverter," *IEEE Trans. Ind. Electron.*, vol. 54, no. 1, pp. 495–503, 2007.
- [41] J. He, Y. W. Li, D. Bosnjak, and B. Harris, "Investigation and Active Damping of Multiple Resonances in a Parallel-Inverter-Based Microgrid," *IEEE Trans. Power Electron.*, vol. 28, no. 1, pp. 234–246, 2013.
- [42] WG C4/B4.38, "Network Modelling for Harmonic Studies," 2017.
- [43] D. C. Montgomery, E. A. Peck, and G. G. Vining, *Introduction to Linear Regression Analysis*, 5th ed. John Wiley & Sons, INC., 2012.
- [44] Midal Cables Ltd., "Conductor Data Sheet - Aluminum Conductors Steel Reinforced (ACSR)." pp. 1–13, 2010.
- [45] J. D. Glover, M. S. Sarma, and T. J. Overbye, *Power System Analysis and Design*, Fifth. Cengage Learning, 2010.
- [46] F. Gonzalez-Longatt and J. L. R. Torres, *Advanced Smart Grid Functionalities Based on PowerFactory*. Springer International Publishing, 2018.
- [47] DigSILENT, "User Manual - PowerFactory 2019," p. 1269, 2019.
- [48] R. Memisevic, "Impact of the modelling of transmission network components on the emission limits for distorting loads in HV system." DigSILENT Pacific Pty Ltd, pp. 1–16, 2011.
- [49] A. Bonner *et al.*, "Modeling and Simulation of the Propagation of Harmonics in Electric Power Networks, Part I: Concepts, Models, and Simulation Techniques," *IEEE Trans. Power Deliv.*, vol. 11, no. 1, pp. 452–465, 1996.
- [50] DigSILENT GmbH, "DigSILENT PowerFactory - Overhead Line Constants." DigSILENT GmbH, pp. 1–24, 2018.
- [51] J. D'Errico, "Eigenshuffle." MathWorks, 2020.

Appendix A Network Models

A.1 PowerFactory Karoo Network Overview

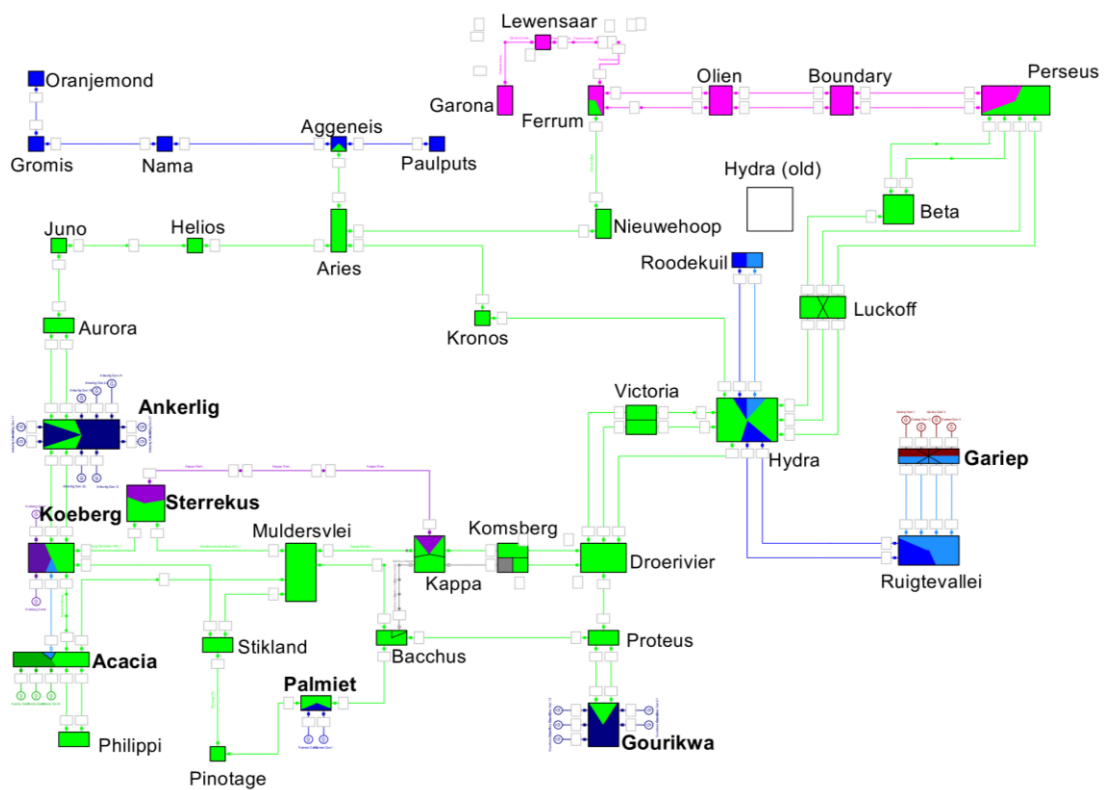


Fig. A-8-1. Large Western Cape generating network overview

A.2 PowerFactory Karoo Network Overview

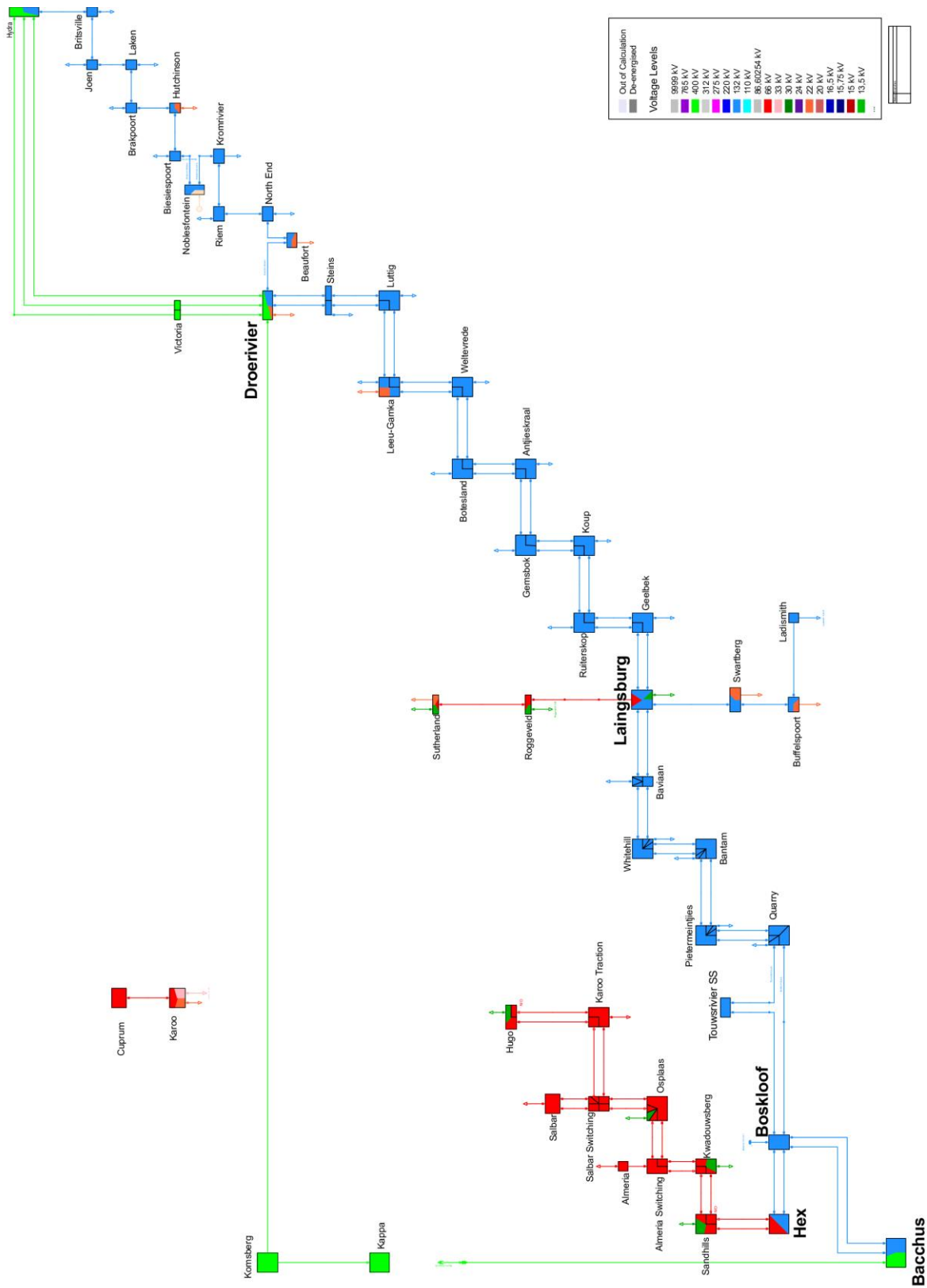


Fig. A-8-2. Complete Karoo network overview

A.3 Complete RPP PowerFactory Model

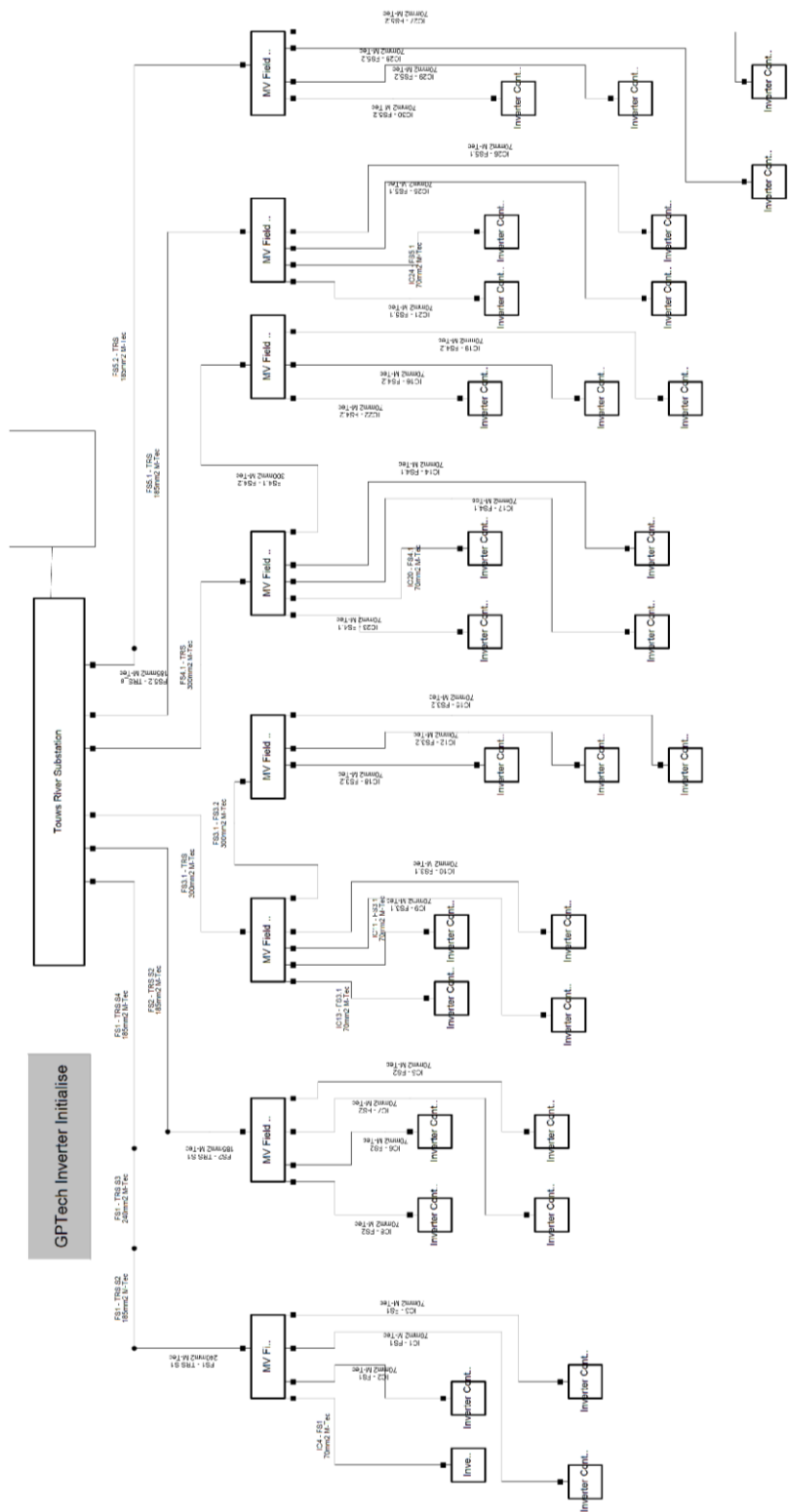


Fig. A-8-3. Complete RPP PowerFactory Model

A.4 Partial Network Configuration Representation

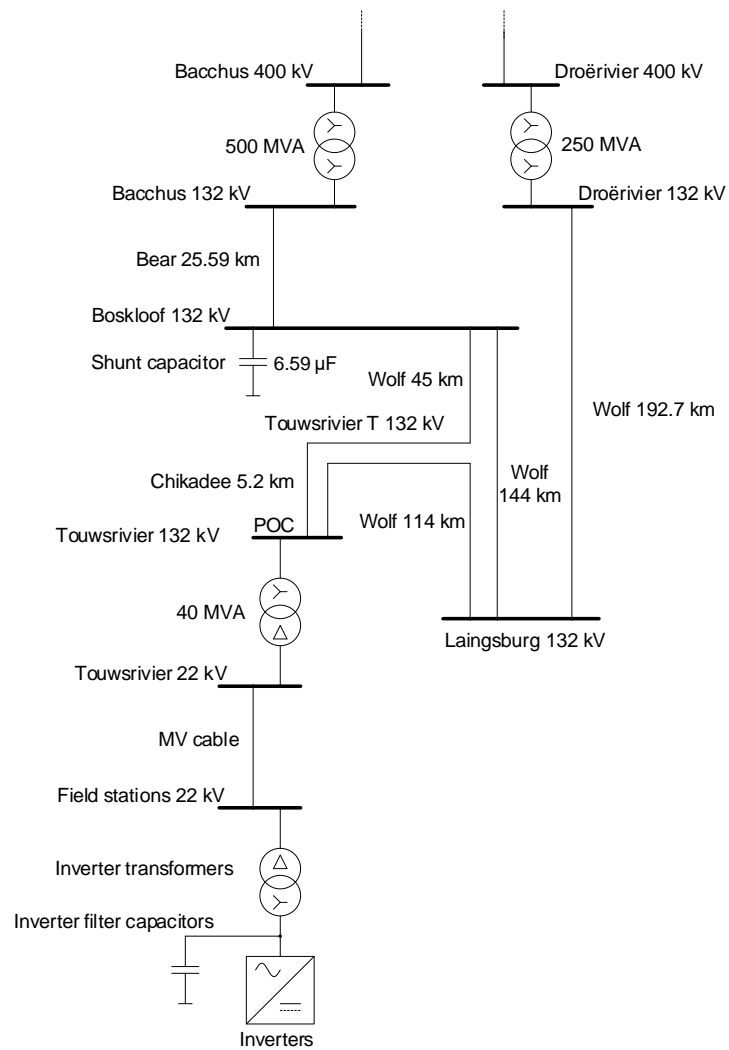


Fig. A-8-4. Partial network representation with connected RPP installation

A.5 Partial Network PowerFactory Model

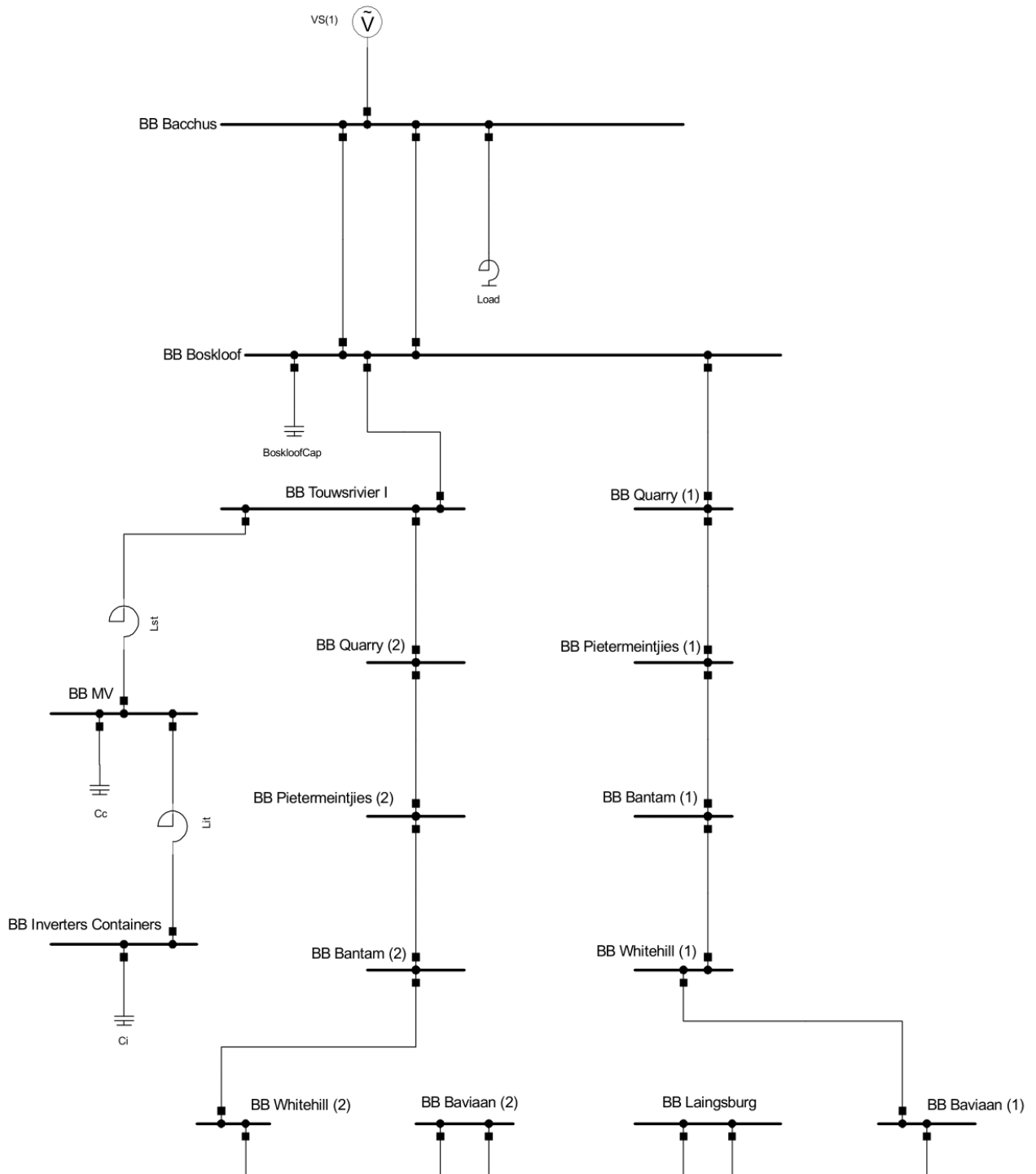


Fig. A-8-5. Partial network model developed in PowerFactory

Appendix B Python Code Discussion

The following code discussions elaborate on the 3 python files that were developed to provide the required functionality. The code creates a PowerFactory object of class *PowerFactorySim* using the PowerFactory API, providing developed functions associated with the *PowerFactorySim* class, method calls are made from the data handling file and executed the main file.

The code for importing the PowerFactory API is listed below:

Code I: Importing PowerFactory API module.

```
import sys

#Direct to powerfactory module folder
sys.path.append(r"C:\Program Files\DIgSILENT\PowerFactory
SP2\Python\3.7")

import powerfactory as pf
```

The PowerFactory simulation object class with the initialisation method defined within the class is defined as follows:

Code II: Defined class object with initialisation method.

```
class PowerFactorySim(object):
    def __init__(self, folder_name='folder_name',
                 project_name='project_name',
                 study_case_name='study_case_name', Unom=132):

        # Start PowerFactory in Engine Mode
        self.app = pf.GetApplication()

        # Activate project -> returns 0 success/1 not found
        self.project = self.app.ActivateProject(
            os.path.join(folder_name, project_name))

        # Activate project default [0] study case
        study_case_folder = self.app.GetProjectFolder('study')
        study_case = array(study_case_folder.GetContents(
            study_case_name+'.IntCase'))
        self.study_case = study_case[0]
        self.study_case.Activate()

        # Set system nominal voltage [kV]
        self.unom = Unom
```


The arguments that are passed to the *PowerFactorySim* class are the *folder_name*, the folder name in which the PowerFactory project is located, *project_name*, the project name within the specified folder, *study_case_name*, the project's study case name and *Unom*, the nominal voltage that will be considered for the system in kV. The *self* argument refers to the object that is created by the class *PowerFactorySim* and is used to define object specific attributes and methods.

The definition for the frequency sweep method is defined in the PowerFactory simulation object class as follows:

Code III: Frequency sweep preparation method defined in PowerFactorySim class.

```
def prepare_fsweep(self, monitored_variables,
                  fsweep_mode='balanced',
                  start_freq = 1, step_size = 0.1,
                  stop_freq = 2500, show_h = 1):

    # Get result file
    self.res = self.app.GetFromStudyCase('Freq.Sweep.ElmRes')

    # Select result variables to monitor
    for elm_name, var_names in monitored_variables.items():
        # Get all network elements that match 'elm_name'
        elements = self.app.GetCalcRelevantObjects(elm_name)

        # Select variables to monitor for each element
        for element in elements:
            self.res.AddVars(element, *var_names)

    # Translate load flow mode keyword to its int equivalent
    modes = {'balanced': 0, 'unbalanced': 1}
    self.fsweep = self.app.GetFromStudyCase('ComFsweep')

    # Set load flow mode
    self.fsweep.iopt_net = modes[fsweep_mode]

    # Set nominal frequency
    self.fsweep.frn timer = 50

    # Set frequency sweep range
    self.fsweep.fstart = start_freq
    self.fsweep.fstep = step_size
    self.fsweep.fstop = stop_freq

    # Set single return harmonic order [h]
    self.fsweep.ifshow = show_h
```

The *monitored_variables* argument is a dictionary object that contains the result variables' information that will be monitored, *fsweep_mode* indicates whether the system is analysed in a 'balanced' or 'unbalanced' mode, *start_freq*, *step_size* and *stop_freq* are variables that are used to establish the frequency range and *show_h* is the resultant harmonic value that is returned for system impedance methods.

The method executing the frequency sweep, as specified in *prepare_fswweep()*, is defined as follows:

Code IV: Frequency sweep execution method defined in PowerFactorySim Class.

```
# Execute: frequency sweep command
def run_fswweep(self):
    return bool(self.fswweep.Execute())
```

The *self.fswweep* command contains the frequency sweep information and the *.Execute()* method performs the calculation as specified by the command object (*Com**).

The method for acquiring the frequency sweep results for a specific bus is defined as follows:

Code V: Frequency sweep results call method defined in PowerFactorySim class.

```
def get_fswweep_results(self, elm_name, var_name):

    # Get network element of interest (default first element)
    element = self.app.GetCalcRelevantObjects(elm_name)[0]

    # Find column in results file that holds result of interest
    col_index = self.res.FindColumn(element, var_name)

    # Get number of rows (frequency points) in the result file
    n_rows = self.res.GetNumberOfRows()

    # Read results and frequencies and store them in lists
    freq = []
    var_values = []

    for i in range(n_rows):
        freq.append(
            self.res.GetValue(i))
        var_values.append(
            self.res.GetValue(i, col_index)[1])

    # Return result variables
    return freq, var_values
```

The *elm_name* variable refers to the name of the element (bus) for which the frequency results are returned. The *var_name* variable is the resultant data which is either the frequency sweep impedance (*m:Z*) or phase angle (*m:phiz*).

The method to construct the system positive sequence admittance matrix is defined as follows:

Code VI: Admittance matrix construction method defined in PowerFactorySim Class

```

# Construct and return system admittance matrix
def get_Ybus(self, start_freq = 0.1, step_size = 0.1,
             stop_freq = 2500, rDis = 0):

    buses = self.app.GetCalcRelevantObjects('BB*.ElmTerm',
                                           includeOutOfService = 0)

    FR = array(arange(start_freq, stop_freq + step_size, step_size))

    # Initialise variables
    size = len(buses)
    Ybus = zeros((size,size,FR.size), dtype=complex)
    cnt = 0

    # Self-Admittance
    for bus in buses:
        # Temp self admittance variable
        Ybb = 0
        connElms = bus.GetConnectedElements(1,1,1)

        # Iterate through each element connected to bus
        for i in range(len(connElms)):

            element = connElms[i]
            elm_type = element.GetClassName()

            # Verify class type to calculate admittance
            if elm_type == 'ElmVac':           #AC voltage source
                Yf = 1/(element.Rl +
                       (element.Ll)*1e-3*FR*2*pi*1j)

            elif elm_type == 'ElmShnt':       #Shunt/Filter Element
                if element.shtype == 1:       #Type R-L

                    Yf = 1/(element.rrea +
                           (element.rlrea)*1e-3*FR*2*pi*1j)

                if element.shtype == 2:       #Type C

                    Yf = ((element.gparac)*1e-6 +
                           (element.ccap)*1e-6*FR*2*pi*1j)

            # Transform element to 132kV
            Yf = Yf*(element.ushnm/self.unom)**2

            # Delta configuration value x3 for pos. seq.
            if element.ctech == 0:
                Yf *= 3

```

```

elif elm_type == 'ElmLod':          #Load model
    if element.plini > 0:
        R = (bus.uknom)**2/element.plini
    if element.qlini != 0:
        X = (bus.uknom)**2/(element.qlini)

    Yf = 1/(R + X*FR/50)*(bus.uknom/self.unom)**2

elif elm_type == 'ElmSind':        #Series reactor
    Yf = 1/(element.rrea +
            (element.lrea)*1e-3*FR**2*pi*1j)

elif elm_type == 'ElmLne':        #Overhead line model

    # Get line pos. seq. admittance
    Y1 = element.GetY1m(element)

    # If line admittance can be calculated from GetY1m()
    if Y1[0] == 0:

        Y1 = (Y1[1]*1e-6 + 1j*Y1[2]*1e-6*FR/50)/2

    else:

        # Geometric coordinates (x,y) of conductors
        cCoord = array(element.typ_id.xy_c)[0,1:7]

        # Calculate distance between conductors
        Dab = sqrt((cCoord[0]-cCoord[1])**2 +
                  (cCoord[3]-cCoord[4])**2)
        Dac = sqrt((cCoord[0]-cCoord[2])**2 +
                  (cCoord[3]-cCoord[5])**2)
        Dbc = sqrt((cCoord[1]-cCoord[2])**2 +
                  (cCoord[4]-cCoord[5])**2)

        # Calculate geometric mean distance
        GMD = cbrt(Dab*Dac*Dbc)

        # Get radius of conductors
        r = element.pCondCir.diacono*1e-3/2

        # Shunt capacitance formula
        Cpu = 2*pi*8.854e-12/(math.log(GMD/r))*1e3

        Y1 = 1j*FR**2*pi*Cpu*element.dline/2

    # Get line pos. seq. impedance and apply skin effect
    Z1 = (element.R1*(1 + 0.646*(FR/50)**2/
                    (192 + 0.518*(FR/50)**2)) +
          1j*element.X1*FR/50)

    Yf = transpose(Y1 + 1/Z1)

```

```

elif elm_type == 'ElmTr2':          #2-winding transformer

    # Get transformer operating values
    Ntap      = element.NTap()
    Rst, Xst  = element.GetZpu(Ntap, 0)
    Sr        = element.typ_id.strn

    # Calculate base impedance values
    Zb        = bus.uknom**2/Sr
    Rst, Xst  = Rst*Zb, Xst*Zb

    Yf = 1/(Rst + 1j*Xst*(FR/50)) #Arrillaga transformer model

elif elm_type == 'ElmTr3':        # 3-winding transformer

    # rated apparant powers at different voltage levels
    Sr        = [element.typ_id.strn3_h,
                 element.typ_id.strn3_m,
                 element.typ_id.strn3_l]

    # Busbar identifiers
    BB        = [element.bushv.ctrm.loc_name,
                 element.busmv.ctrm.loc_name,
                 element.buslv.ctrm.loc_name]

    # Zbase with bus voltage reference
    Zb        = bus.uknom**2/min(Sr)

    # z (0,1,2) HV-MV/MV-LV/LV-HV branch
    z = zeros((3,1), dtype=complex)

    for i in range(0,3):
        Ntap = element.NTap(i)
        zpu = element.GetZpu(Ntap,i,0)
        z[i] = (zpu[0]+1j*zpu[1])*Zb

    mat = inv(array([[1,1,0],[1,0,1],[0,1,1]]))

    # Zn (0,1,2) LV/MV/HV-branch
    Zn = matmul(mat,z)

    Zt = Zn[2]*Zn[1]+Zn[0]*Zn[1]+Zn[2]*Zn[0]
    Zhv_mv = Zt/Zn[0]
    Zmv_lv = Zt/Zn[1]
    Zhv_lv = Zt/Zn[2]

    Yhv_mv = 1/(Zhv_mv.real + 1j*Zhv_mv.imag*FR/50)
    Yhv_lv = 1/(Zhv_lv.real + 1j*Zhv_lv.imag*FR/50)
    Ymv_lv = 1/(Zmv_lv.real + 1j*Zmv_lv.imag*FR/50)

    # HV side
    if bus.loc_name == BB[0]:

        Yf = Yhv_mv + Yhv_lv

```

```

# MV side
elif bus.loc_name == BB[1]:

    Yf = Yhv_mv + Ymv_lv

# LV side
elif bus.loc_name == BB[2]:

    Yf = Yhv_lv + Ymv_lv

# Transform element to 132kV
Yf = Yf*(bus.uknom/self.unom)**2
Ybb += Yf

# Set mutual admittance counter
cnt1 = 0

# Mutual-Admittance
# Iterate through the buses
for node in buses:
    Yf = 0

    # Get connected elements connected to "node"
    linkElms = node.GetConnectedElements(1,1,1)

    # Skip iterations according to interconnected elements
    if node == bus or bool(set(linkElms)
        .intersection(connElms)) == False:
        cnt1 += 1
        continue
    else:
        # Get linking elements connecting bus with node
        jointElms = list(set(linkElms)
            .intersection(connElms))

        # Iterate through linking elements and calculate impedance
        for i in range(len(jointElms)):

            if jointElms[i].GetClassName() == 'ElmLne':
                Z1 = (jointElms[i].R1*(1 + 0.646*(FR/50)**2/
                    (192 + 0.518*(FR/50)**2)) +
                    1j*jointElms[i].X1*FR/50)

            elif jointElms[i].GetClassName() == 'ElmSind':
                Z1 = (jointElms[i].rrea +
                    (jointElms[i].lrea)*1e-3*FR**2*pi*1j)

            elif jointElms[i].GetClassName() == 'ElmTr2':

                Ntap      = jointElms[i].NTap()
                Rst, Xst = jointElms[i].GetZpu(Ntap, 0)

                Sr        = jointElms[i].typ_id.strn
                U_hv      = jointElms[i].typ_id.utrn_h

                Zb        = U_hv**2/Sr

                Rst, Xst = Rst*Zb, Xst*Zb

```

```

Z1 = (Rst + 1j*Xst*(FR/50))

if U_hv != self.unom:
    Z1 = Z1*(self.unom/U_hv)**2

elif jointElms[i].GetClassName() == 'ElmTr3':
    # Set base for HV-side
    Sr = [jointElms[i].typ_id.strn3_h,
          jointElms[i].typ_id.strn3_m,
          jointElms[i].typ_id.strn3_l]

    U = [jointElms[i].typ_id.utrn3_h,
          jointElms[i].typ_id.utrn3_m,
          jointElms[i].typ_id.utrn3_l]

    BB = [jointElms[i].bushv.ctrm.loc_name,
          jointElms[i].busmv.ctrm.loc_name,
          jointElms[i].buslv.ctrm.loc_name]

    # Zbase with system voltage ref [132 kV]
    Zb = self.unom**2/min(Sr)

    # z (0,1,2) HV-MV/MV-LV/LV-HV branch
    z = zeros((3,1),dtype=complex)

    for j in range(0,3):
        Ntap = jointElms[i].NTap(j)
        zpu = jointElms[i].GetZpu(Ntap,j,0)

        z[j] = (zpu[0]+1j*zpu[1])*Zb

    mat = inv(array([[1,1,0],[1,0,1],[0,1,1]]))

    # Zn (0,1,2) LV/MV/HV-branch
    Zn = matmul(mat,z)

    # Calculate delta configuration values
    Zt = Zn[2]*Zn[1]+Zn[0]*Zn[1]+Zn[2]*Zn[0]
    Zhv_mv = Zt/Zn[0]
    Zmv_lv = Zt/Zn[1]
    Zhv_lv = Zt/Zn[2]

    # HV-MV or HV-LV branch
    if node.loc_name == BB[0] or bus.loc_name == BB[0]:

        # HV-MV branch
        if node.loc_name == BB[1] or
           (bus.loc_name == BB[1]):
            Z1 = Zhv_mv.real + 1j*Zhv_mv.imag*FR/50

        # HV-LV branch
        else:
            Z1 = Zhv_lv.real + 1j*Zhv_lv.imag*FR/50

    # MV-LV branch
    else:
        Z1 = Zmv_lv.real + 1j*Zmv_lv.imag*FR/50

```

```

        Yf += 1/Z1

    Ybus[cnt][cnt1] = -Yf
    cnt1 += 1
cnt += 1

```

The defined method for constructing the admittance matrix consists of two parts. The first part iterates through all the specified buses calculating the self-admittance of each bus and applying it to the admittance matrix. The second part determines which elements are connected between the current bus and all the other buses, once again iterating through the specified buses.

In both parts the admittance is calculated according to the defined class name of the object. This is determined through the *GetClassName()* method. The class name defines the element type and dictates which method needs to be applied to calculate the admittance.

The method for acquiring the bus structure information is defined as follows:

Code VII: System bus listing information dictionary construction.

```

# Method constructing bus format dictionary
def list_bus_elements(self, rDis = 1):
    self.bus_map = {}
    bus_elm_list = []

    # Acquire specified bus objects
    buses = self.app.GetCalcRelevantObjects('BB*.ElmTerm',
                                            includeOutOfService = 0)

    for bus in buses:

        # Get elements connects to bus
        connElms = bus.GetConnectedElements(1, rDis, 1)

        # Add connected elements to bus element list
        for i in range(len(connElms)):
            bus_elm_list.append(connElms[i].loc_name)

        # Add bus information to dictionary
        self.bus_map[bus.loc_name] = bus_elm_list
        bus_elm_list = []

    return self.bus_map

```

The structure of the system is stored within the defined dictionary *bus_map* which contains the various buses' and connected elements' names. This is used in conjunction with the result plots to identify the buses and assign their participation factors accordingly.

Another Python file *Data_Handle.py* was created to provide data handling capabilities including the corresponding simulation execution and various data oriented calculations. Various figure plotting

methods were also included in the *Data_Handle.py* file. The following imports were required for the methods in the data handling file:

```
import matplotlib.image as mpimg
import matplotlib.pyplot as plt
import numpy as np

from scipy.io import savemat
from numpy.linalg import inv
from math import floor, ceil
```

The main functional methods declared in the data handler are discussed below.

The first method that is defined in the data handler file is the simulation evaluation method. This method is defined as follows:

Code VIII: Simulation evaluation and execution function.

```
def eval_sim_type(pfsim, SIM_TYPE, MONITORED_VARIABLES):

    # Execute loadflow procedure
    if SIM_TYPE == 0:

        pfsim.prepare_loadflow()
        pfsim.run_loadflow()

    # Execute fsweep procedure
    elif SIM_TYPE == 1:

        pfsim.prepare_fsweep(
            monitored_variables = MONITORED_VARIABLES,
            show_h              = 1
        )
        pfsim.run_fsweep()

    # EMT/RMS simulation
    elif SIM_TYPE == 2:

        pfsim.prepare_dynamic_sim(
            monitored_variables = MONITORED_VARIABLES,
            sim_type           = 'ins',
            start_time         = 0.0,
            step_size          = 0.001,
            end_time           = 0.02)
        pfsim.run_dynamic_sim()
```

The parameters that are passed to the *eval_sim_type()* method are the PowerFactory simulation object (*PowerFactorySim*) containing the simulation information, the *SIM_TYPE* variable identifying the simulation type and the *MONITORED_VARIABLES* variable containing the parameters that are stored in the simulation results object.

Three simulation types are defined in this method namely, loadflow, frequency sweep and EMT/RMS. The loadflow simulation type is setup to obtain bus voltage values from a loadflow execution. The

frequency sweep simulation type writes bus frequency data to the results object. The EMT/RMS simulation type produces time series data for waveform analysis.

Next, the `get_Zbus()` method is defined as follows:

Code IX: Method for converting admittance to impedance.

```
def get_Zbus(pfsim, ybus):
    zbus = np.zeros((len(ybus), len(ybus), ybus.shape[2]), dtype=complex)
    for i in range(0, ybus.shape[2]):
        zbus[:, :, i] = inv(ybus[:, :, i])

    return zbus
```

The PowerFactory simulation object and the constructed admittance bus matrix are passed to this method. The inverse of the 3D admittance matrix is calculated and returned.

Next, the `get_freq_sweep()` method was defined as follows:

Code X: Method for returning specified bus frequency sweep results.

```
def get_freq_sweep(pfsim, bus_name):
    # Get frequency sweep results
    Z = pfsim.get_fsweep_results(
        bus_name+'.ElmTerm', 'm:Z')
    [phiZ, f] = pfsim.get_fsweep_results(
        bus_name+'.ElmTerm', 'm:phiz')
    f = np.array(f)

    # Return appropriate frequency sweep parameters
    return [Z[0], phiZ, f[1]*50]
```

The PowerFactory simulation object is passed along with a system `bus_name` variable indicating the bus name for which the frequency sweep results should be returned. The bus impedance and phase angles as well as the frequency sweep range are return as a list.

The final functional method that was developed in the `Data_Handler` file is the `write_mat()` method defined as follows:

Code XI: Method for writing passed matrix in MATLAB format.

```
def write_mat(ybus):
    # Construct dictionary entry
    mdic = {"YBus": ybus.tolist()}

    # Save dictionary mdic in MATLAB format
    savemat("YBus_matrix.mat", mdic)
```

The system's positive sequence admittance matrix is passed as a parameter and saved in a MATLAB file extension format.

The methods that were declared in the *PowerFactorySim* class within the *pfsim* module as well as the data handler module, *Data_Handle*, are imported into the main Python script. The main script required Code XII to initialise the required Python modules and functions as well as the PowerFactory specific project information.

Code XII: Main Python script variable initialisation.

```

#-----
#                               Import required modules and module functions
#-----

import Data_Handle as DH
import pfsim as pfs

#-----
#                               Initialise PowerFactory Project/Simulation Object
#-----

SIM_TYPE           = 'fsweep'
FOLDER_NAME        = 'Touwsrivier'
PROJECT_NAME       = 'TR line reduction'
STUDY_CASE_NAME    = 'Study Case'
MONITORED_VARIABLES = {
    'BB*.ElmTerm': ['m:u1:A', 'm:u1:B', 'm:u1:C', 'm:Z', 'm:phiz', 'm:Y']
}
SIM_TYPES = {'loadflow': 0, 'fsweep': 1, 'dyn_sim': 2}

# Initialise Sim Object
pfsim = pfs.PowerFactorySim(
    folder_name      = FOLDER_NAME,
    project_name     = PROJECT_NAME,
    study_case_name  = STUDY_CASE_NAME)

# POC bus index
nbus = 13

```

The project information includes the simulation type that is executed, the folder directory in which the PowerFactory project is located, the name of the project file, the investigated study case name (default 'Study Case') and the variables that are monitored during the simulation. The PowerFactory simulation object is generated at the start and functions as a global object. Finally, the bus index of the POC bus is declared as a variable.

The main Python file consists of a *main()* function with a conditional execution statement using the special `__name__` variable. The main file is defined as follows:

Code XIII: Main function with conditional launcher.

```

#-----
#                               Main
#-----

def main():

    # Evaluate and execute simulation type
    DH.eval_sim_type(pfsim, SIM_TYPES[SIM_TYPE], MONITORED_VARIABLES)

    # Acquire list of bus names
    bus_list = pfsim.list_bus_elements(rDis = 1) #Ignore disconnected elms

    # Conditional results for each simulation type
    if SIM_TYPE == "loadflow":

        # Get bus voltages from load flow simulation
        voltages = pfsim.get_bus_voltages()

    elif SIM_TYPE == "fsweep":

        # Get frequency sweep results from PowerFactory
        fsweep_res = DH.get_freq_sweep(pfsim, list(bus_list.keys())[nbus])

        # Get admittance matrix from PowerFactory system
        [f, ybus] = pfsim.get_Ybus(step_size = 0.1, rDis = 1)
        zbus = DH.get_Zbus(pfsim, ybus)

        D, phi, psi, pf = pfsim.modal_analysis(Ybus=ybus)

    elif SIM_TYPE == "dyn_sim":

        time_series_list = DH.get_voltages(pfsim, bus_list, nbus)

if __name__ == "__main__":
    main()

```

The defined *main()* function evaluates the simulation type, acquires a list of the bus names and executes appropriate functions according to the set simulation type. This main function is executed using a conditional statement that evaluates the “*__name__*” variable which is set to “*__main__*” when the main file is used to execute the script.

Appendix C MATLAB Code Discussion

The MATLAB code that was used to apply RMA on the system admittance matrix and plot the modal impedances are discussed below.

The eigenvalue decomposition of the power system admittance matrix is a 3-dimensional operation as the 2-dimensional admittance matrix is also a function of frequency. To obtain the eigenvalues of the system in the correct order a function “*eigenshuffle*” obtained from the MathWorks file exchange and published by John D'Errico [51] was incorporated.

The variables were declared and initiated as follows:

Code XIV: MATLAB variable initialisation for modal impedance calculation function.

```
% Initiate YBus - 3D system admittance matrix with freq. range [0.1:0.1:2500]
load('YBus_matrix.mat')

% Initiate variables
FR = 0.1:0.1:2500;

psi = zeros(16,16,length(YBus));
PF = zeros(16,16,length(YBus));
ZBus = zeros(16,16,length(YBus));
Z_rev = zeros(16,16,length(YBus));

% Right eigenvector and eigenvalues
[phi, D] = eigenshuffle(YBus);
```

The “*eigenshuffle*” function returns the 3D right eigenvector (ϕ) and 2D diagonal eigenvalue matrix (D) in the correct order. From the results obtained from the “*eigenshuffle*” function the modal impedance can be plotted using the inverse of the constructed 2D eigenvalue matrix as follows:

Code XV: Plotting modal impedances through elementwise inverse 2-dimensional eigenvalue matrix.

```
% Plot modal impedances

figure
plot(FR, abs(D.^-1))
set(gca, 'yscale', 'log')
grid on
```

The participation factor matrix is calculated in a for loop as follows:

Code XVI: For loop calculating the PFs of the admittance matrix.

```
% Calculate participation factor matrix

for i = 1:length(YBus)

    psi(:, :, i) = inv(phi(:, :, i));
    PF(:, :, i) = phi(:, :, i).*(psi(:, :, i).');

end
```

This participation matrix's values can be analysed to determine what the participation of any bus is towards any mode through calling $PF(b,m,f)$ where b is the bus number, m is the mode number and f is the frequency.

Appendix D Additional Resonant Mode Results

The complete plot of all the modes in the investigated power system illustrated in Fig. A-8-5 are illustrated Fig. D-.

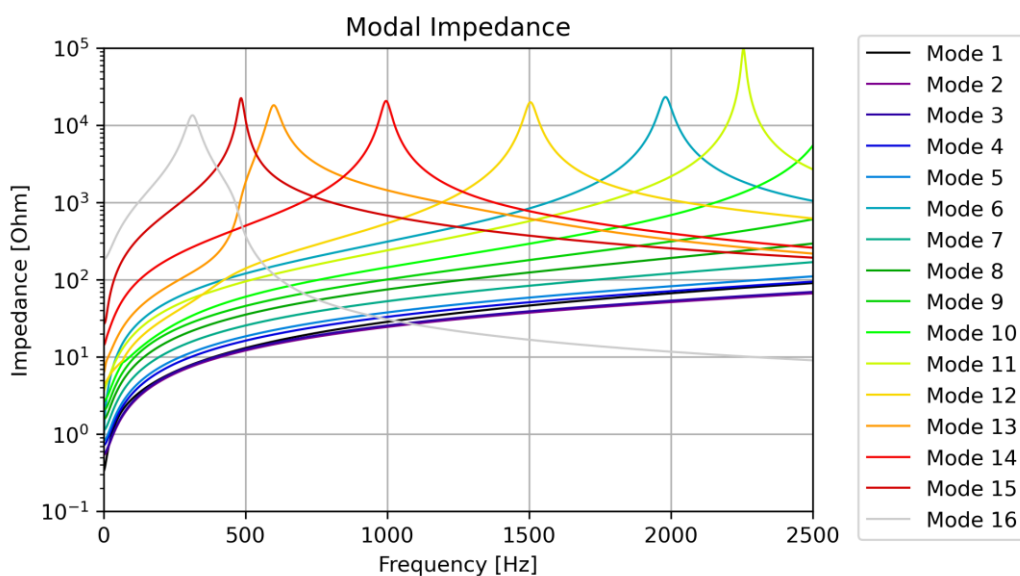
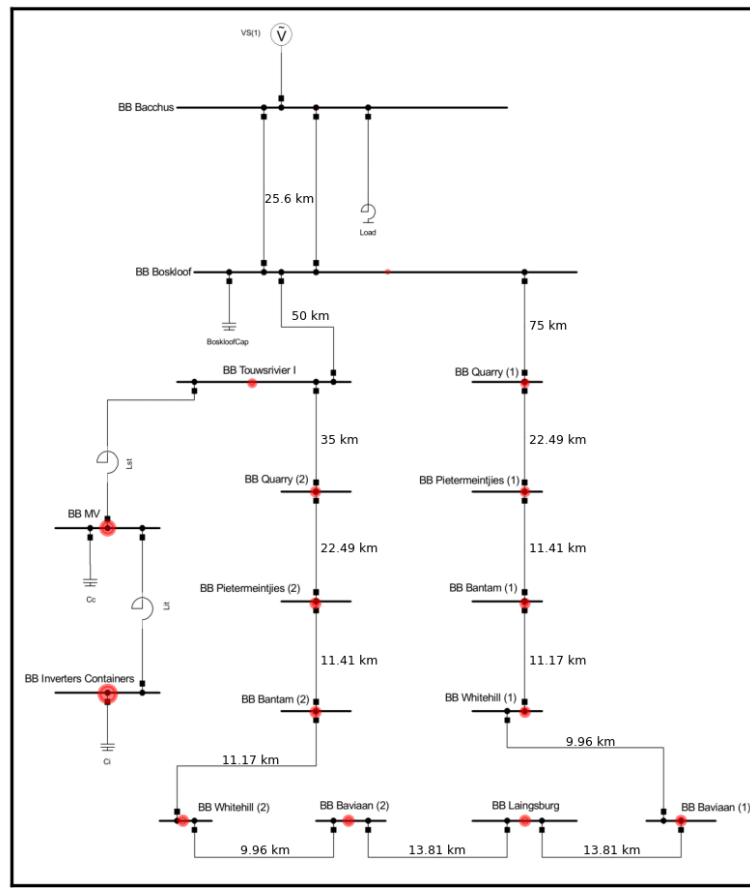


Fig. D-1. Modal impedances of all the extended power system's modes

It is illustrated that there exists a mode for each node in the investigated power system. Several of these modes present in Fig. D- do not have a resonant condition within the 2500 Hz frequency spectrum but 7 modes are identified that does have resonant peaks.

The visualisation of the participation of the various buses to the dominant mode resonant conditions is displayed in Fig. D-2 to Fig. D-9. The PFs are plotted as circles on the associated busbar to illustrate the contribution that it has to the resonant condition at the investigated frequency.

Participation for Mode 16 @ 313.7 Hz



Mode 16 Participation Factors @ 313.7 Hz

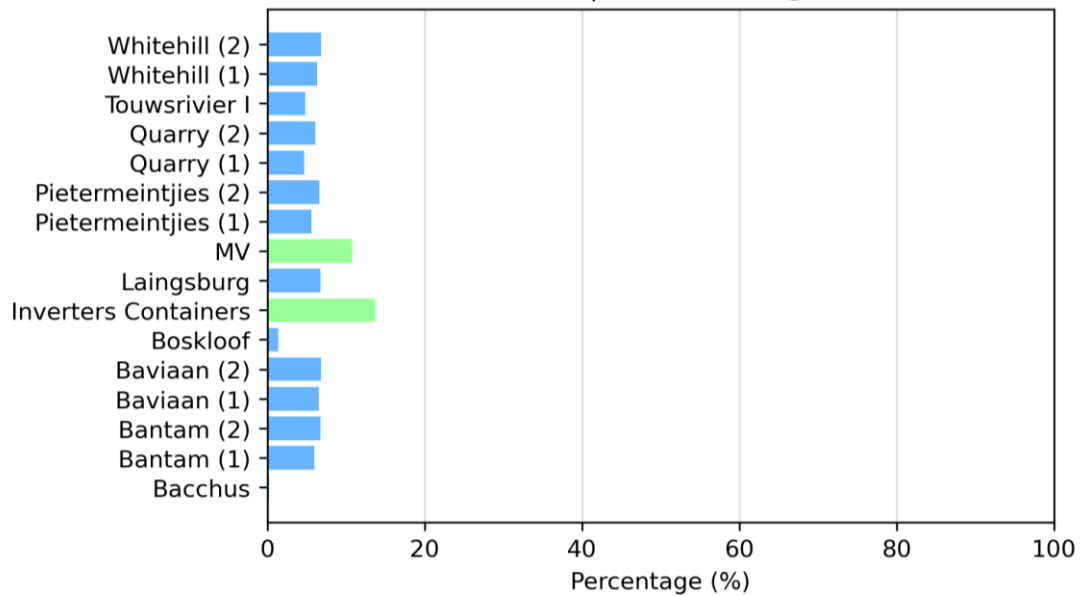
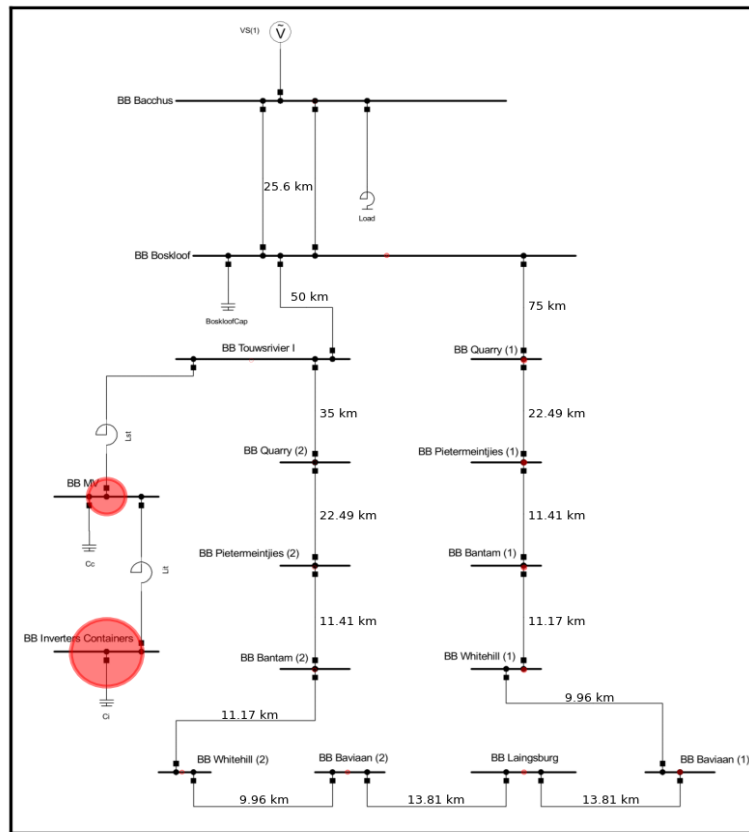


Fig. D-2. Power system bus participation visualisation (top) and bar graph (bottom) for mode 16 at 313.7 Hz

Participation for Mode 15 @ 485.0 Hz



Mode 15 Participation Factors @ 485.0 Hz

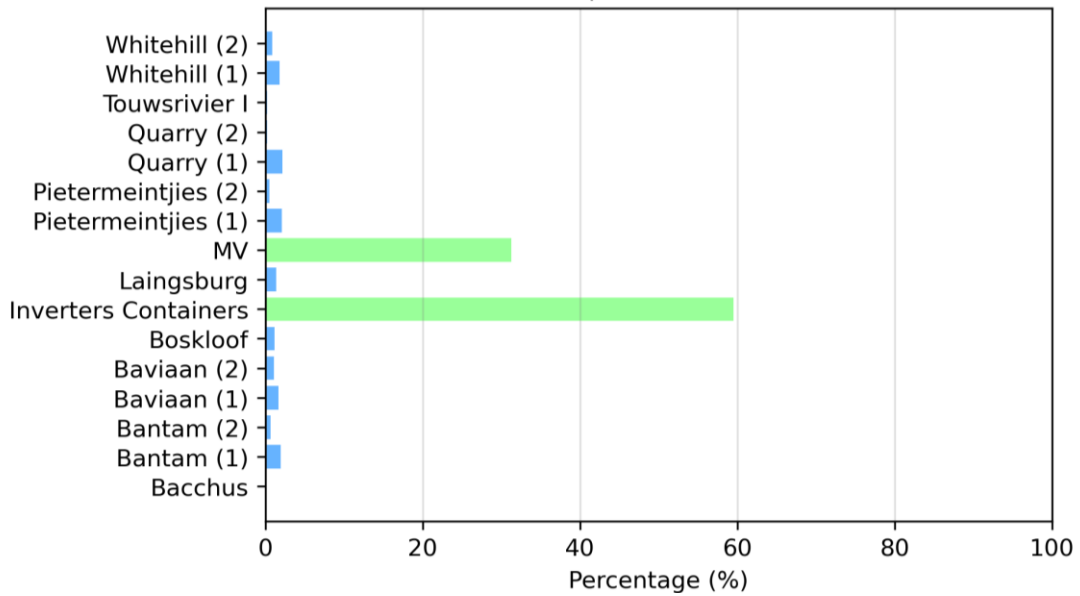
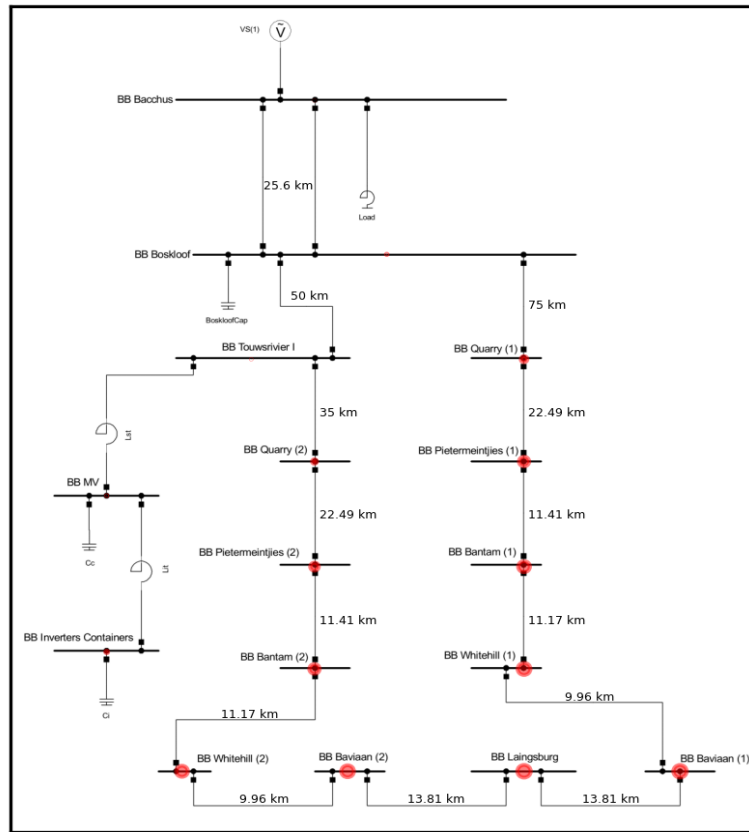


Fig. D-3. Power system bus participation visualisation (top) and bar graph (bottom) for mode 15 at 485.0 Hz

Participation for Mode 13 @ 600.3 Hz



Mode 13 Participation Factors @ 600.3 Hz

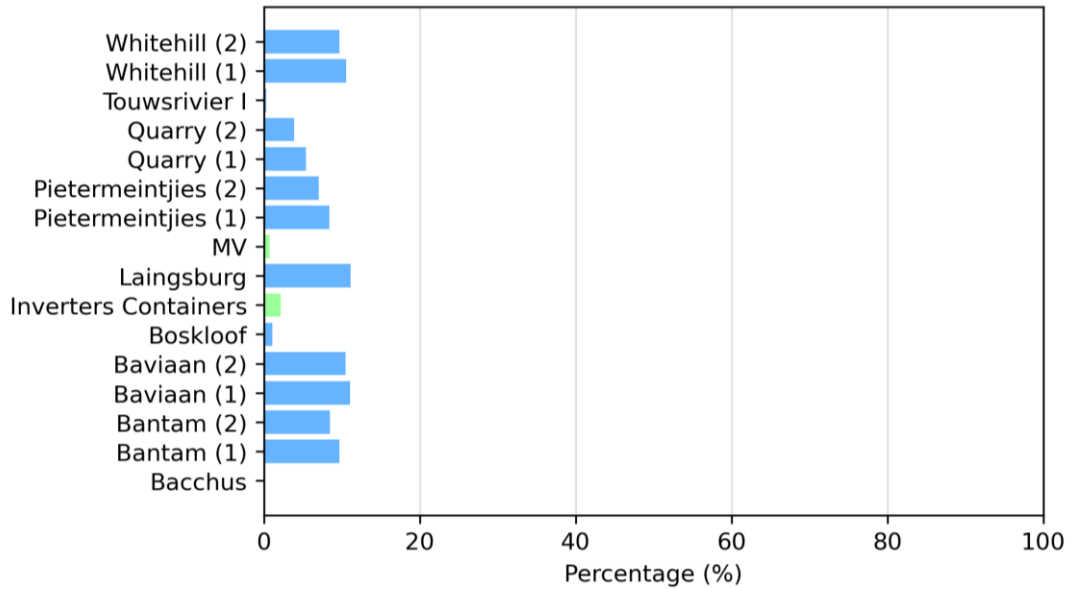
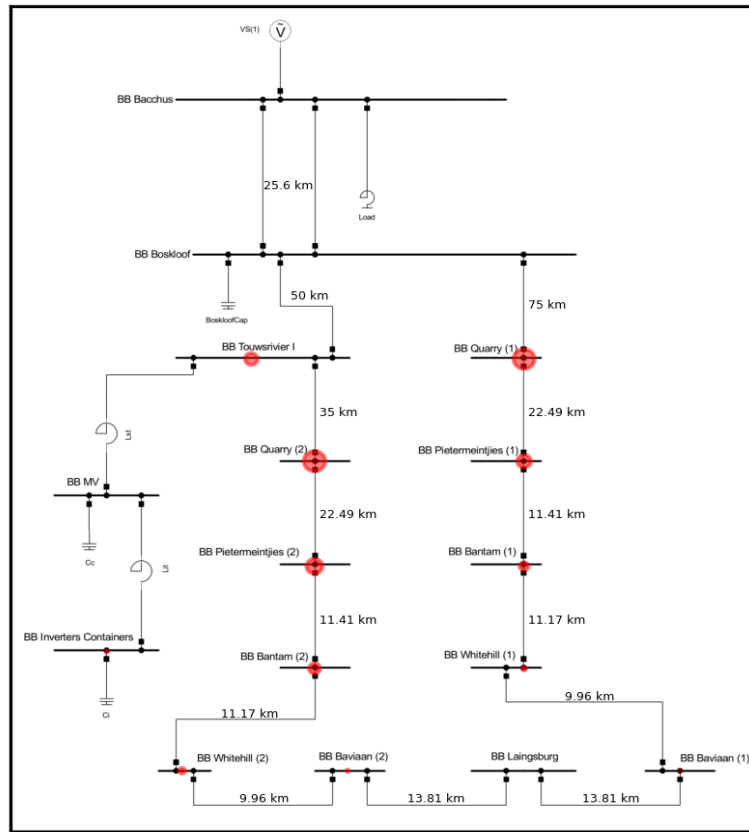


Fig. D-4. Power system bus participation visualisation (top) and bar graph (bottom) for mode 13 at 600.3 Hz

Participation for Mode 14 @ 996.1 Hz



Mode 14 Participation Factors @ 996.1 Hz

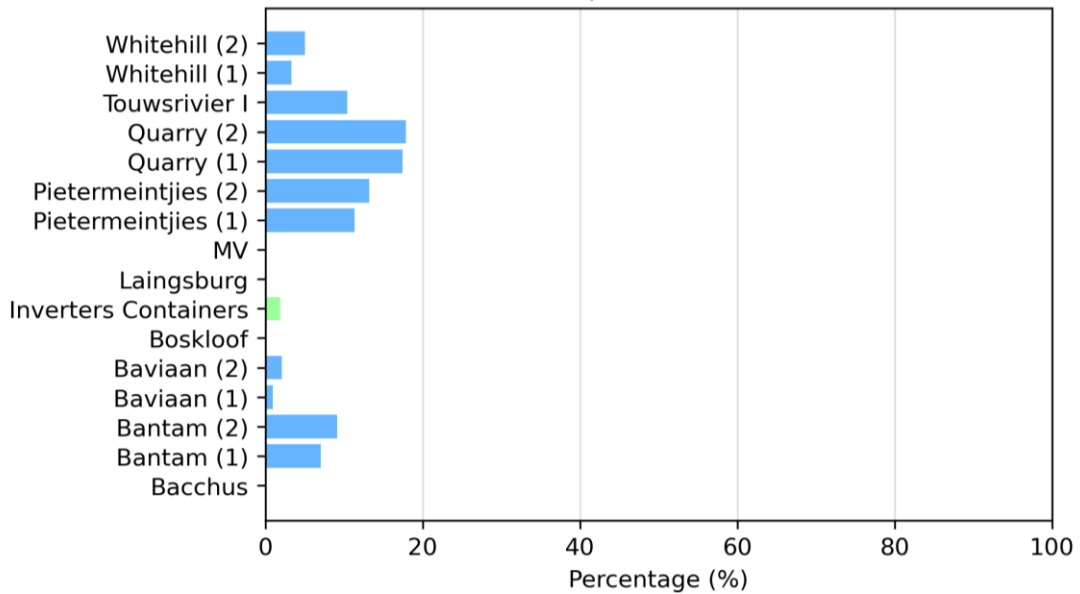
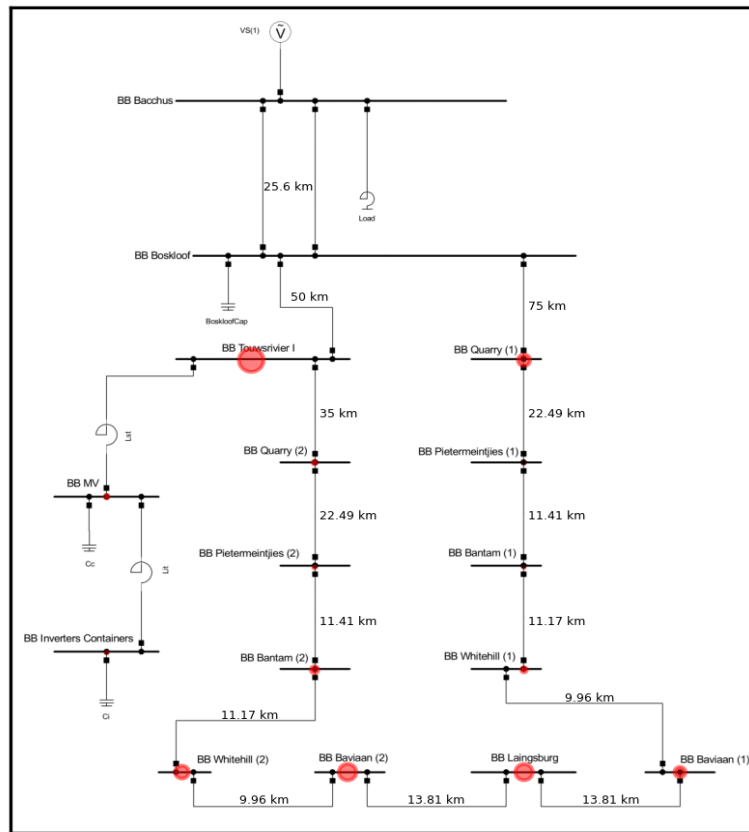


Fig. D-5. Power system bus participation visualisation (top) and bar graph (bottom) for mode 14 at 996.1 Hz

Participation for Mode 12 @ 1505.4 Hz



Mode 12 Participation Factors @ 1505.4 Hz

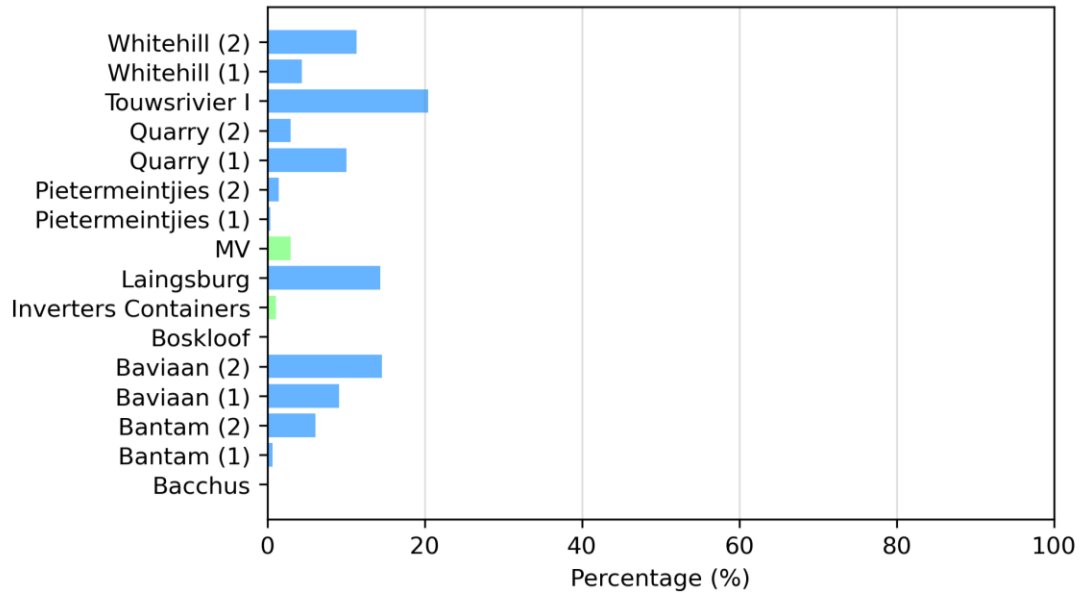
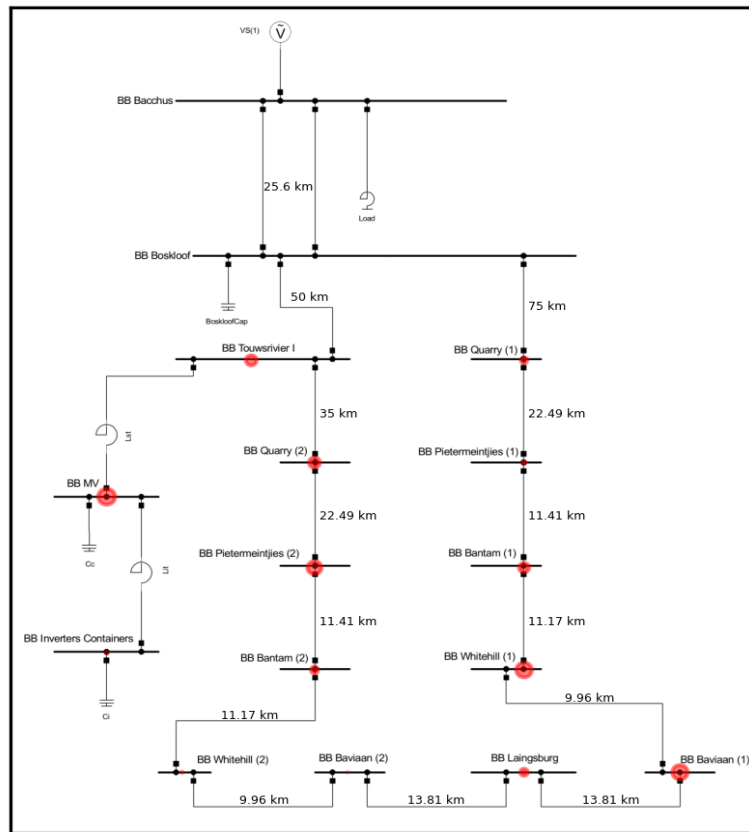


Fig. D-6. Power system bus participation visualisation (top) and bar graph (bottom) for mode 12 at 1505.4 Hz

Participation for Mode 6 @ 1981.4 Hz



Mode 6 Participation Factors @ 1981.4 Hz

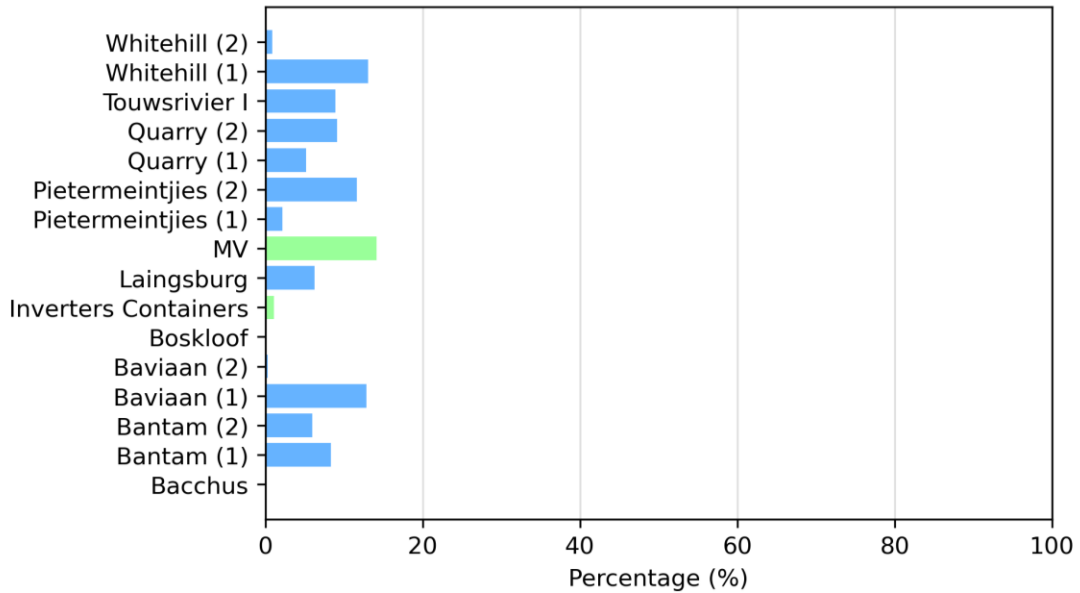
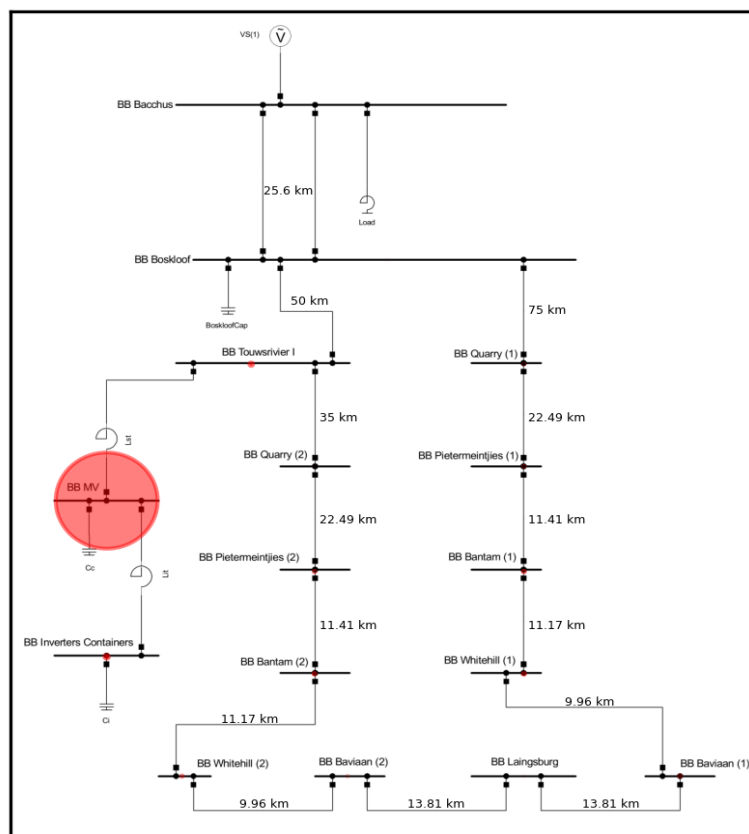


Fig. D-7. Power system bus participation visualisation (top) and bar graph (bottom) for mode 6 at 1981.4 Hz

Participation for Mode 11 @ 2256.3 Hz



Mode 11 Participation Factors @ 2256.3 Hz

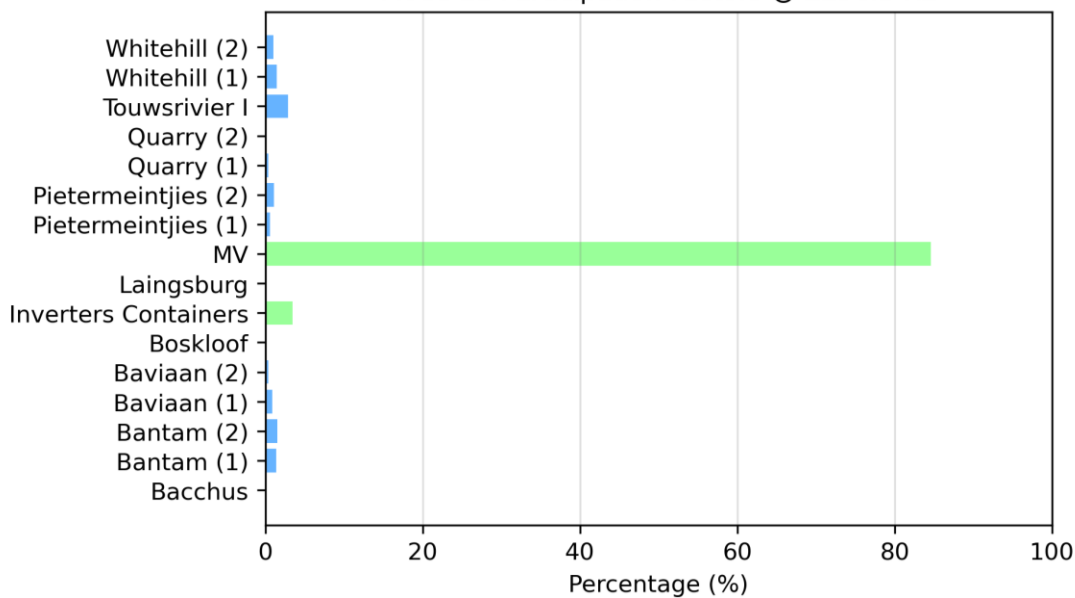


Fig. D-8. Power system bus participation visualisation (top) and bar graph (bottom) for mode 11 at 2256.3 Hz